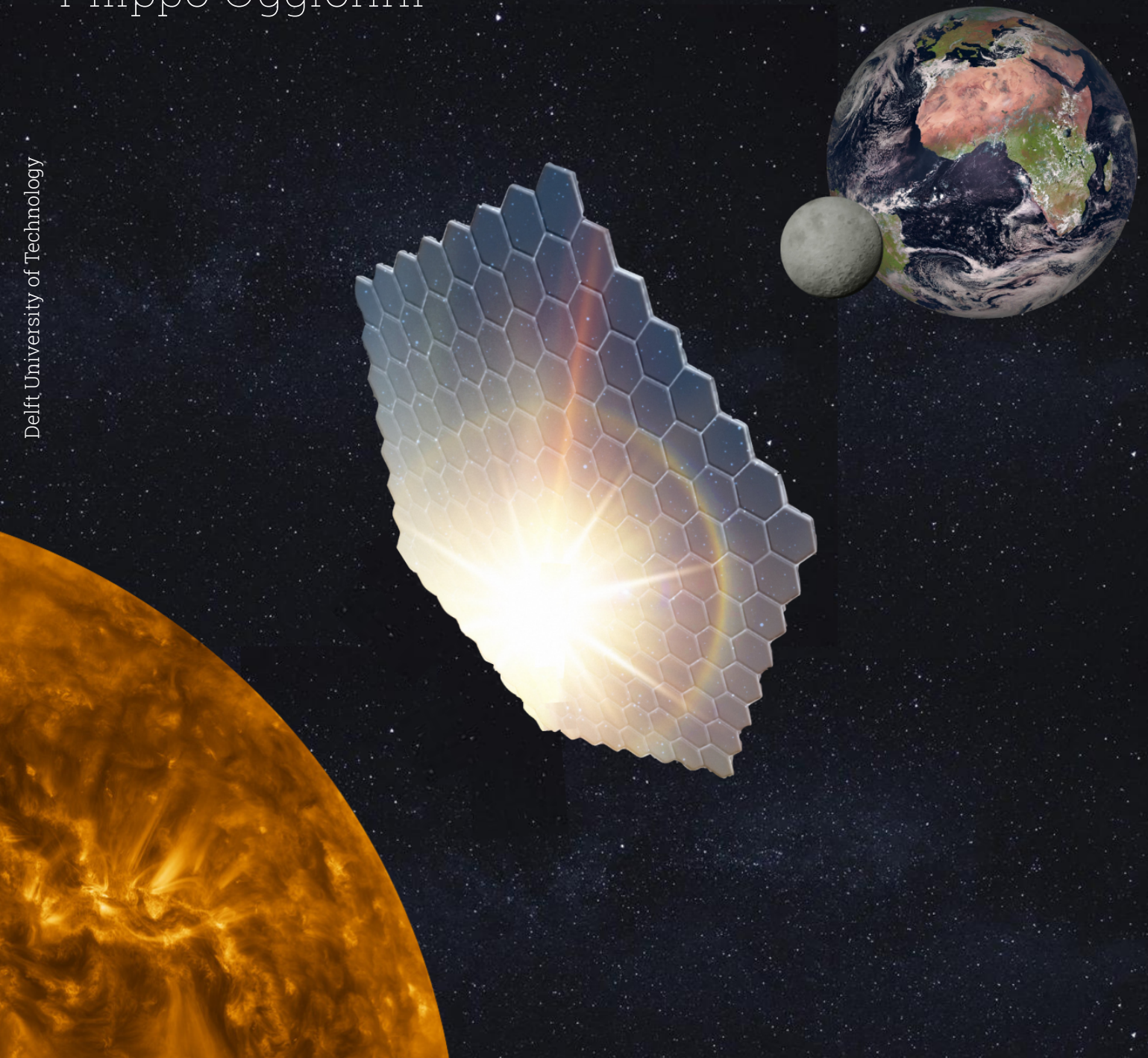# Trajectory optimization of a planetary sunshade

MSc Thesis

Filippo Oggionni

Trajectory optimization of a planetary sunshade

MSc Thesis

by

Filippo Oggionni

to obtain the degree of Master of Science
at the Delft University of Technology,
to be defended publicly on Friday, October 7th, 2022 at 13:00.

Student number: 5152542
Project duration: June 30th, 2021 – October 7th, 2022
Thesis committee: Dr. Ir. E. J. O. Schrama,   TU Delft, Chair
                    Dr. M. J. Heiligers,   TU Delft, Supervisor
                    Dr. A. Menicucci,   TU Delft
                    Dr. J. Pau Sanchéz   ISAE-Supaero, Co-Supervisor

Cover: Artist's impression of a planetary sunshade (adapted from NASA/ESA/Solar Orbiter, Planetary Sunshade Foundation, Kai Pilger)

An electronic version of this thesis is available at `http://repository.tudelft.nl/`.

TUDelft

Preface

The journal article that constitutes the core of this report starts and concludes with the same word: climate. My generation grew up while hearing about worrying issues with the Earth's climate. First, the ozone layer becoming thinner and thinner, followed by warnings about rising sea levels. Later, scientist spoke about the acceleration of global warming, like modern Cassandras. Finally, the predictions of the International Panel on Climate Change periodically shocked the world, but only for the few days these alarming reports made it through the news. It took devastating floods in Germany, raging wildfires in California, record-high temperatures in Canada, month-long droughts in France, sinking cities in South-East Asia, disappearing glaciers on the Alps, and asphalt melting in London for the world to acknowledge the seriousness of the problem. Sometimes more than other generations, young people seem to be fully aware of what is at stake. As a matter of fact, the climate is the core of this thesis.

However, the dire situation we are facing today does not make the climate a less fascinating physical system. Edward Norton Lorenz, a famous mathematician and meteorologist, outlined its complexity and instability in a famous journal paper, titled: "Does the Flap of a Butterfly's Wings in Brazil Set Off a Tornado in Texas?". With this title, Lorenz brilliantly summarized the unpredictability of the Earth's atmosphere, which he linked to the theory of deterministic chaos. Interestingly enough, the concept of a chaotic yet deterministic system was previously formulated by French mathematician Henri Poincaré, who unveiled many features of the Three-Body Problem and other dynamical systems for the first time. If the climate is the horizon of this thesis, orbital mechanics and solar sailing are the tools with which this thesis is built.

I sincerely hope that the concept behind this work will never have to be implemented. If that does not happen, it will mean that mankind managed to bring greenhouse gas emissions under control. Either way, working with climate models and studying the basic functioning of the climate system has been an exciting journey. It does take quite some creativity, which might turn into "hybris", to even think of making deliberate modifications to the climate on a planetary scale; still, I believe more research should be carried out on the topic of geoengineering. After all, in the past 200 years, we have constantly introduced larger and larger perturbations to the natural climate system, simply without realizing it. Offering a potential "emergency plan" to the most serious of mankind's challenges, together with the fact that this plan can be conceived mostly through astrodynamics, made this thesis topic very intriguing and motivating.

Filippo Oggionni
Delft, October 7th, 2022

Executive Summary

Climate change is undoubtedly one of the most pressing issues of the 21st Century. Geoengineering systems can delay irreversible climate changes and provide the international community with more time while working towards the net-zero emission goal. In this report, a space-based solar radiation management solution is investigated, consisting of a large sunshade located in the vicinity of the Sun-Earth L_1 point. Despite the high costs and low timeliness associated to its deployment, such a system can be very effective in decreasing the solar radiation forcing, allowing to maintain an artificial climate with large concentrations of greenhouse gasses before the net-zero goal is reached. In addition, a space-based geoengineering system does not directly affect the geosphere, thus avoiding possible side effects typical of other solar radiation management techniques, such as aerosol injection in the stratosphere. Furthermore, the trajectory of a planetary sunshade can be tailored to match the distribution of solar irradiance required by a climate system with a large concentration of greenhouse gases.

This thesis investigates different sets of trajectories in close proximity to the L_1 point to produce desirable annual shading patterns. Previous research has shown that a static sunshade located at the L_1 point tends to undercool polar regions and overcool tropical regions. Subsequent work addressed this issue by considering periodic orbits around the L_1 point to minimize temperature anomalies when the CO_2 concentration is equal to 680 ppm (twice the amount with respect to pre-industrial levels), compared to a reference scenario (340 ppm of atmospheric CO_2 with no sunshade). The current paper further improves on the latter work by considering heteroclinic connections between artificial equilibrium points (AEPs) above and below the ecliptic plane. These AEPs are created by exploiting the solar radiation pressure exerted on the sunshade, enabling a displacement in the location of the L_1 point above or below the ecliptic plane. The movement from above to below the ecliptic plane is synchronized with the seasonal variations on Earth such that the shade is located above the ecliptic plane during summer and below the ecliptic plane during winter (in the northern hemisphere). This movement between the AEPs is repeated twice a year to continuously track the seasonal variations of the climate. An optimal control problem is defined and solved with an orthogonal collocation method to minimize the time spent during the transfer and maximize the time spent at the AEPs.

The dynamical model used in this work is the Circular Restricted Three-Body Problem (CR3BP), while the sunshade is modelled as an ideal solar sail model to account for the solar radiation pressure acceleration. By modifying the sail attitude, it is possible to control the trajectory of the sunshade, enabling a propellant-less control of its motion. When computing the shade produced by the sunshade, a solar limb darkening model is adopted to increase the accuracy of the computation of the artificial solar irradiance distribution with respect to uniformly distributed brightness model for the solar disk. A simplified climate model is used to compute the simulated surface temperature after 50 years.

In this work, it is shown that a dynamic sunshade with a radius of 1434 km and placed in the vicinity of the Sun-Earth L_1 point is able to reduce the global mean surface temperature from 16.39°C (2xCO_2 scenario) to 14.13°C. It also reduces the root mean squares (RMS) of the latitudinal distribution of temperature anomalies from 0.30°C to 0.28°C, while lowering the polar mean surface temperature (for latitudinal bands above 65°) by more than 2°C with respect to a scenario without sunshade and by 0.06°C with respect to the static sunshade. The optimal results are achieved when the sunshade is located at a distance equal to 30% of the Earth's radius above and below the ecliptic plane, with the transfers between AEPs starting respectively at day 56 and day 250, both measured from January 1st.

This work contributes to the body of research investigating the feasibility of implementing a space-based geoengineering solution. It bridges the gap between the concept of a static sunshade located at the Sun-Earth L_1 point and several climate studies considering various artificial distributions for solar irradiance. It does so by proposing a novel transfer trajectory design scheme, where the sunshade's motion is tailored to the seasonal variations in the Earth's climate. The framework developed in this work is based on the assumption that the trajectory design process and the evaluation of the climate response are tightly coupled, something that has been rarely done before. Therefore, the methodology used in this work will be beneficial for further research. Ultimately, this work provides new insight into the technical feasibility of space-based geoengineering, as well as into the subsequent climate effects.

Contents

List of Figures

List of Tables

Nomenclature

List of abbreviations

AEP	=	Artificial Equilibrium Point
AU	=	Astronomical Unit
CDR	=	Carbon Dioxide Removal
CR3BP	=	Circular Restricted Three-Body Problem
EU	=	European Union
GHG	=	Greenhouse Gas
GMST	=	Global Mean Surface Temperature
GREB	=	Globally Resolved Energy Balance
IPCC	=	International Panel on Climate Change
PMST	=	Polar Mean Surface Temperature
PPM	=	Parts Per Million
RMS	=	Root Mean Squares
SRF	=	Synodic Reference Frame
SRM	=	Solar Radiation Management
SRP	=	Solar Radiation Pressure
UN	=	United Nations
WMO	=	World Meteorological Organization

List of symbols

Roman symbols

C	=	Jacobi's constant
J_{RMS}, J_{GMST}, J_{PMST}	=	Objective functions for the heuristic optimization problem
m_1	=	Mass of the primary (Sun)
m_2	=	Mass of the secondary (Earth)
$\hat{\mathbf{n}}$	=	Vector normal to the sunshade
$S(\hat{\mathbf{x}}, \hat{\mathbf{y}}, \hat{\mathbf{z}})$	=	Synodic Reference Frame
S_0	=	Solar constant
T	=	Surface temperature
$\bar{T}$	=	Monthly mean surface temperature
$\bar{T}^{\text{GMST}}$	=	Global mean surface temperature
$\bar{T}^{\text{PMST}}$	=	Polar mean surface temperature
t_N	=	Start time of the transfer trajectory from above to below the ecliptic plane
t_S	=	Start time of the transfer trajectory from below to above the ecliptic plane
U	=	Potential function of the CR3BP
z_N	=	Vertical displacement of the AEP above the ecliptic plane
z_S	=	Vertical displacement of the AEP below the ecliptic plane

Greek symbols

β	=	Lightness number
μ	=	Mass parameter of a CR3BP
ω	=	Angular velocity vector of the Earth around the barycenter of the Sun-Earth system

Subscripts

$\square_{\text{geo}}$	=	Geoengineered scenario
$\square_{\text{ref}}$	=	Reference scenario (340 ppm of atmospheric CO_2)
$\square_{\text{2XCO2}}$	=	Non-geoengineered scenario (680 ppm of atmospheric CO_2)

Superscripts

$\square^{static}$	=	Scenario with static sunshade
$\square^{dynamic}$	=	Scenario with dynamic sunshade
$\hat{\square}$	=	Unit vector
$\bar{\square}$	=	Averaged quantity
$\square^*$	=	Relative quantity

1

Introduction

In this chapter, background information about climate change, geoengineering, and the planetary sun-shade is provided. A short literature review is presented and the gap in the current research body is identified. The research objective and questions to fill that gap are then laid out. The chapter is concluded with an overview of the structure of the report.

1.1. Climate change

Climate change has been defined by many authors as "the problem of the 21st Century". It is undoubtedly the first time in the history of our Planet that the relevance of anthropogenic climate change surpasses that of natural climate change. In the 1980s, scientists have started investigating the effect of human activities on the climate [1]. In 1988, the International Panel on Climate Change (IPCC) was established as an independent body by the United Nations (UN) and the World Meteorological Organization (WMO) to research the scientific basis of climate change, assess its consequences, and provide policy recommendations to governmental institutions. Since then, the international recognition of ongoing human-driven changes to the climate has slowly but progressively increased. Numerous international agreements have been signed, such as the Kyoto protocol in 1997 [2] or the more recent Paris agreement in 2015. More and more attention is being dedicated to the environment; entire policy programs are focused on the prevention of further climate changes, such as the Next Generation EU promoted by the European Union to shape the post-pandemic recovery of the bloc, heavily centered around plans to reach carbon neutrality by 2050.

Nevertheless, it is becoming clear that ongoing efforts to avoid future carbon emissions might not be sufficient to solve the problem [3]. Even if global emission were to instantaneously stop, the surface temperature would continue to rise for many years and it would take long before returning to pre-industrial levels. Indeed, preventive strategies alone (i.e., the progressive reduction of greenhouse gas emissions towards full carbon neutrality) might not be enough. In addition, it must be reminded that the non-linear behavior of the climate, coupled with increasing levels of human-driven forcing, might cause climate *tipping points* to be reached: these are thresholds that, once reached, trigger irreversible changes in the climate system [4]. Examples of tipping points are the melting of portions of the ice caps, the destruction of carbon sinks (such as large forests like the Amazon), and the weakening of the Atlantic Thermohaline Circulation. As a response to the slow reaction of the international community to receiving and implementing effective policy recommendations recommended by scientists, climate geoengineering solutions have been proposed.

1.2. The case for geoengineering

Geoengineering is the intentional modification to the Earth's climate to slow down or halt global warming [5].

Geoengineering techniques are classified in two main groups [5]:

- *Carbon Dioxide Removal* (CDR) — this category includes all solutions attempting to decrease the total atmospheric carbon content by actively removing CO_2 with different techniques, with the

goal of progressively undoing anthropogenic modifications to the climate;

- *Solar Radiation Management* (SRM) — this category comprises geoengineering concepts allowing for a reduction of the incoming solar radiation (also referred to as *insolation*), without intervening directly on greenhouse gases.

The effects of SRM techniques are not yet well understood because they do not attempt to reduce the total amount of GHGs, but they act on a difference source of climate forcing: the incoming solar radiation. For this reason, the resulting climate of a world geoengineered through SRM solutions will be largely "artificial", with unprecedented levels of GHGs and reduced insolation. The climatic response to this combination of factors is far from being well understood, especially at a regional scale. Indeed, while the global response can be simulated fairly well, the reduction of the solar constant can cause variations at the local level (regional weather) that are generally complicated to reproduce and understand. In particular, the hydrological cycle and precipitation patterns deserve more attention and are not as well understood as the surface temperature. Furthermore, SRM solutions do not address the problem of ocean acidification [5]. As a result, SRM techniques are usually considered less safe than CDR counterparts due to the currently high uncertainties on their effects. However, they have the advantage of delivering results in the time scale of a few years after deployment, which makes them a suitable solution in case "emergency" situations are reached. If certain conditions entailing too high risks of reaching climate tipping points are verified, a temporary short-term fix may become necessary. This is where SRM techniques would come into play, thanks to the relatively fast climatic response they cause. Nevertheless, the problem of maintaining such solutions for a long time, combined with the potentially delicate equilibrium between the two sources of climate forcing and the possibility of incurring into *termination shocks* (i.e., the abrupt failure of a SRM system), suggests that SRM techniques should be implemented only for short period of times and only if strictly necessary, while they should not be considered as long-term solutions [5].

All methods and technologies supporting geoengineering solutions are relatively recent. Therefore, more research is needed not only to improve their performance, but also to predict the actual outcome on the Earth's climate following the application of such methods. Common issues about geoengineering solutions do not only concern their technical aspects, but also the social, political, and legal implications that these interventions would have. Although the bare technologies to create geoengineering solutions already exist, all non-technical questions mentioned above will greatly benefit from further research both on the implementation of geoengineering techniques and on their effects on the climate. The research body is still insufficient to provide policymakers with robust and mature recommendations on the case of geoengineering [5]. This work is a step in the direction of filling such gap.

1.3. Space-based geoengineering

Space-based techniques are commonly considered to be very expensive endeavors and their deployment would span several tens of years; on the other hand, they can be very effective, they can be controlled (at least to a certain degree) and they do not pose any risk of contamination of the Earth's environment. In addition, space-based methods present the same drawbacks common to all SRM methods, such as the risks connected to termination effects and the fact that these techniques do not address the issue of ocean acidification. On the other hand, the implementation of a space-based solution has the side effect of boosting the development of the space sector, as both governmental institutions and private companies would be involved in a large international effort.

The design of space-based geoengineering techniques involve many disciplines, spanning from systems engineering to climate sciences. Regardless of the selected concept, the manufacturing and logistical aspects of such a large-scale project are enormous. Managing the governance at a global scale of such an endeavor could prove even more difficult. However, the existing body of literature already offers interesting discussions and preliminary solutions for many of the issues mentioned above. Although some proposals of space-based geoengineering missions are envisaged in Low Earth Orbit, the most promising solutions are envisaged to be deployed at the Lagrange point between the Sun and Earth, where all accelerations have a net sum of zero in a synodic reference frame. This makes it an equilibrium point that co-rotates with the same angular velocity of the Earth around the Sun.

The first publication proposing such concept is reference [6], where a shield made of Lunar material is envisaged. The work conducted in reference [7] followed shortly after, where different optical solutions (using reflecting and absorbing materials for the manufacture of the screen) are proposed

and research requirements are outlined. Following proposals include the work in references [8, 9, 10]. These all focus on placing a thin film or a metallic reflector at L_1, mainly as a single object, but possibilities of having large constellations or even *clouds* of much smaller devices are explored. In these proposals, the shield is effectively considered as a solar sail, so that the impact of the solar radiation pressure acceleration is accounted for in the orbital calculations. These ideas were further discussed in reference [11], where the focus is steered to considerations about launch systems and the economical aspects of such endeavors. The cost-effectiveness of space-based geoengineering has been also discussed in other studies [12]. Similar discussions are also reported in reference [13], which is an extensive source treating geoengineering solutions (including the solar disk at L_1) and other macro-engineering proposals from a broader perspective. There have been also studies focusing on more specific aspects of a solar shield placed at L_1, for example about passive control of the solar sail [14] or its structural feasibility [15]. The work in references [16, 17] explored the possibility of placing a dust cloud at L_1, instead of an actively controlled sunshade.

Although all geoengineering systems proposed in references [6, 17] are envisaged to be statically located at the L_1 point, some works also hint at the fact that the orientation of the sail can be exploited to control the shield and its position along the Sun-Earth line. In particular, solar sailing constitutes a propellantless form of orbit maneuvering, making it a very appealing concept to control the orbit of such a massive object. The only study conducted so far on a solar shield orbiting around the L_1 point is reference [18]. Such work focuses on the orbit design and preliminary optimization of a sunshade oscillating around L_1 to minimize the residual climate changes in a geoengineered climate with high levels of atmospheric CO_2. This work aims to expand its conclusions and explore different orbital solutions that would provide different shading patterns on Earth with the goal to offset residual temperature anomalies. It is clarified here that, due to the scale and complications of a geoengineering project, it was chosen to explore only the trajectory aspect of a geoengineering mission to L_1. As mentioned before, there are numerous other aspects that would deserve similar dissertations. Hopefully, the currently growing interest in the topic will deliver more studies covering other aspects and benefiting from other disciplines different from astrodynamics.

1.4. Research objective and questions

The research objective of this thesis is the following:

> To improve our understanding of how the motion of a planetary sunshade, in particular its out-of-plane displacement during a full year, affects the Earth's climate system with large concentrations of atmospheric CO_2.

Such research objective can be broken down into three research questions:

1. *Is it possible to couple the out-of-plane motion of a planetary sunshade with the Earth's seasonal cycle to offset global warming, solely relying on the solar radiation pressure acceleration?*

   This research question aims to investigate the ideal out-of-plane displacement profile of a planetary sunshade. While the in-plane displacement has an impact on the sizing process of the shade, which is a systems engineering problem, a specific out-of-plane displacement profile can be achieved without changing the design of the shade. Therefore, it is important to understand the relation between the vertical displacement of the sunshade and the Earth's climate at different times of the year. This topic has not been researched before, as in most publications a static sunshade is assumed, except in reference [18]. Finally, this research question underlines how only the solar radiation pressure acceleration can used as an control technique.

2. *Is the combination of parking locations and time-optimal transfer trajectories an effective mission design strategy for a planetary sunshade?*

   This research question focuses on the specific trajectory design choices made in this work. The design approach selected for this work is fundamentally different from the one proposed in reference [18], which offers a case for cross-comparison. In addition, the characterization of the trajectory optimization approach adopted in this work for a single sunshade will be useful for future research work considering a swarm of smaller sunshades.

3. *How does a genetic algorithm compare to a grid search with respect to finding the optimal trajectory solution of a planetary sunshade that minimizes temperature anomalies?*

   This research question aims to explore different methods to explore the design space. In general, the grid search is a useful method to understand at a high level what impact each independent variable has on the objective functions, whereas the genetic algorithm allows to confirm and fine-tune the findings revealed by grid searches.

1.5. Structure of the report

The core of this report is constituted by a paper titled *Trajectory optimization of a planetary sunshade around the Sun-Earth L1 point for solar geoengineering*, reported in Chapter 2. The paper is written following the AIAA conference paper template and will be presented at the ASCEND conference 2022, taking place in Las Vegas (Nevada) between 22nd and 24th October 2022[1].

The paper is structured as follows. In the *Introduction*, an extensive literature review is provided and the outline of the paper itself is presented. In the *Problem definition and methodology* section, the nature of the problem is presented and the methodology chosen to solve the problem is explained. In the following four sections, the models adopted in this work are explained in detail. In particular, in the section *Circular restricted three-body broblem* the dynamical model used to simulate the trajectory of the sunshade is presented; in the *Insolation* section, the solar radiation and shade models used to compute the artificial solar insolation distribution are described in detail, while the impact of the planetary sunshade on the Earth's climate and how such impact is evaluated are explained in the section titled *Quantification of climate changes*. Furthermore, the algorithms implemented to numerically optimize the trajectory of the sunshade are presented in the *Numerical optimization* section. Finally, in the *Results and discussion* section the outcome of the optimization problem is presented and the main findings are discussed. These are also briefly summarized in the *Conclusions* section, where the overall contribution of this work to the research body on geoengineering is also assessed.

The conclusions of the thesis report follow in Chapter 3, where the research questions presented in this chapter will be answered and an overall reflection on this work is attempted. Finally, in Appendix A verification and validation methods are presented. Employing these methods are necessary to ensure the correctness of the computer code that implements the models used in this work.

---

[1]`https://ascend.aiaa.org/Category/4c840e6c-4f0f-4a35-b28a-356b6f8e8f65` (accessed on 22nd September 2022).

2

Journal article

Trajectory optimization of a planetary sunshade around the Sun-Earth L_1 point for solar geoengineering

Filippo Oggionni *

A planetary sunshade is a large, reflecting disk built to shield the Earth from a small fraction of solar irradiance and partly compensate global warming caused by greenhouse gas emissions. As a specific form of solar geoengineering, the sunshade is an emergency solution that would be implemented to prevent catastrophic climate change, while working towards the net-zero emission goal. In this paper, a dynamic sunshade is proposed. The motion of the sunshade is designed as a combination of static permanence at two equilibrium points above and below the ecliptic plane to shade the poles and a time-optimal transfer trajectory to connect these equilibrium points without overshading the tropical regions. Such a system is capable of not only reducing the global mean surface temperature anomaly, but also minimizing regional climate changes by tailoring the sunshade's motion according to climate requirements, which is the primary goal of this work. A simplified climate model is used to evaluate the results of a given shading pattern, directly related to the sunshade's trajectory. A dynamic sunshade with a radius of 1434 km and orbiting in the vicinity of the Sun-Earth displaced L_1 point is able to reduce the global mean surface temperature from $16.39°C$ (scenario with 680 ppm of atmospheric CO_2, double the amount with respect to the pre-industrial era) to $14.13°C$ until equilibrium is reached. It also reduces the polar mean surface temperature (for latitudinal bands above $65°$) by more than $2°C$ with respect to a scenario without sunshade and by $0.06°C$ with respect to a static sunshade at the displaced L_1 point. The optimal results are achieved when the sunshade is located at a distance equal to 30% of the Earth's radius above and below the ecliptic plane. In addition, the transfers between the equilibrium points start respectively at day 56 and day 250, both measured from the 1st of January.

I. List of abbreviations

AEP	=	Artificial Equilibrium Point
AU	=	Astronomical Unit
CR3BP	=	Circular Restricted Three-Body Problem
EBM	=	Energy Balance Model
EMIC	=	Earth Model of Intermediate Complexity
EOM	=	Equation of Motion
GDP	=	Gross Domestic Product
GHG	=	Greenhouse Gas
GMST	=	Global Mean Surface Temperature
GREB	=	Globally Resolved Energy Balance
IPCC	=	International Panel on Climate Change
IPOPT	=	Interior Point Optimizer
LEO	=	Low Earth Orbit
LRF	=	Local Reference Frame
NLP	=	Non-Linear Programming
PMST	=	Polar Mean Surface Temperature
PPM	=	Parts Per Million
RCP	=	Representative Concentration Pathway
RMS	=	Root Mean Squares

---
*MSc student, Department of Astrodynamics and Space Missions, Kluyverweg 1, 2629 HS Delft, The Netherlands – f.oggionni@student.tudelft.nl

| SRF | = | Synodic Reference Frame |
| SRP | = | Solar Radiation Pressure |

II. List of symbols

Roman symbols

A	=	Area of the sunshade
$\mathbf{a}_{SRP}$	=	Solar radiation pressure acceleration vector
c	=	Speed of light
c_i	=	Coefficient of order i
d_r	=	Radial distance
F_X	=	Climate forcing due to X
h	=	Hour angle
$|h_0|$	=	Hour angle at sunset/sunrise
I	=	Radiance
I_0	=	Radiance under fully illuminated conditions
I_{ae}	=	Radiance under annular eclipse conditions
I_c	=	Radiance emitted by the Sun at its center
I_{pe}	=	Radiance under partial eclipse conditions
I_r	=	Radiance emitted by the Sun at a radial distance d_r
J_1	=	Objective function for the optimal control problem
$J_{\text{RMS}}, J_{\text{GMST}}$	=	Objective functions for the heuristic optimization problem
$L\left(\hat{\mathbf{r}}_{13}, \hat{\boldsymbol{\zeta}}, \hat{\boldsymbol{\xi}}\right)$	=	Local Reference Frame
m	=	Mass of the sunshade
m_1	=	Mass of the primary (Sun)
m_2	=	Mass of the secondary (Earth)
$\hat{\mathbf{n}}$	=	Vector normal to the sunshade
P	=	Solar radiation pressure
Q	=	Insolation
$\mathbf{r}$	=	Position vector of the sunshade in the SRF
$\mathbf{r}_1$	=	Position vector of the primary (Sun) in the SRF
$\mathbf{r}_2$	=	Position vector of the secondary (Earth) in the SRF
$\mathbf{r}_{13}$	=	Position vector of the sunshade with respect to the Sun
$\mathbf{r}_{23}$	=	Position vector of the sunshade with respect to the Earth
$\mathbf{r}_{A,B}$	=	Position vector of B with respect to A
$\bar{r}_{\oplus}$	=	Average Sun-Earth distance (1 Astronomical Unit)
$r_{\oplus}$	=	Varying Sun-Earth distance
R	=	Radius of a body
$S(\hat{\mathbf{x}}, \hat{\mathbf{y}}, \hat{\mathbf{z}})$	=	Synodic Reference Frame
S	=	Irradiance
S_0	=	Solar constant
T	=	Surface temperature
$\bar{T}$	=	Monthly mean surface temperature
$\bar{T}^{\text{global}}$	=	Global mean surface temperature
$\bar{T}^{\text{polar}}$	=	Polar mean surface temperature
t	=	Generic epoch
t_N	=	Start time of the transfer trajectory from above to below the ecliptic plane
t_S	=	Start time of the transfer trajectory from below to above the ecliptic plane
U	=	Potential function of the CR3BP
$\mathbf{X}_1$	=	State vector of the optimal control problem
$\mathbf{X}_2$	=	Decision vector of the heuristic optimization problem
z_N	=	Vertical displacement of the AEP above the ecliptic plane

z_S	=	Vertical displacement of the AEP below the ecliptic plane
Greek symbols		
α	=	Cone angle
β	=	Lightness number
γ	=	Solar angle corresponding to a radial distance d_r
δ	=	Clock angle
η	=	Angular separation between the Sun and the sunshade
θ	=	Cone angle
λ	=	Latitude angle
μ	=	Mass parameter of a CR3BP
ν	=	Declination angle
σ	=	Critical sail loading
τ	=	Surface albedo
φ	=	Longitude angle
χ_{clouds}	=	Cloud albedo
χ_{surf}	=	Surface albedo
ψ	=	Solar zenith angle
ω	=	Angular velocity vector of the Earth around the barycenter of the Sun-Earth system
Ω	=	Solid angle subtended by a body
Subscripts		
$\square_D$	=	Sunshade
$\square_{\text{geo}}$	=	Geoengineered scenario
$\square_{\text{ref}}$	=	Reference scenario
$\square_\oplus$	=	Earth
$\square_\odot$	=	Sun
Superscripts		
$\hat{\square}$	=	Unit vector
$\bar{\square}$	=	Averaged quantity
$\dot{\square}$	=	First derivative with respect to time
$\ddot{\square}$	=	First derivative with respect to time
$\square^*$	=	Relative quantity

III. Introduction

Climate change is one of the most pressing issues of the 21st century. As a matter of fact, the Fifth Assessment Report from the International Panel on Climate Change (IPCC) draws four different Representative Concentration Pathways (RCPs), outlining different climatic scenarios based on future, predicted emissions of greenhouse gases (GHG). These four scenarios would result in a globally averaged surface temperature anomaly between $1.0\,^\circ$C and $4.0\,^\circ$C by 2100 [1]. In Fig. 1, the temperature anomaly resulting from a step-like increase of CO_2 content (680ppm) is shown. Such a scenario, which will be explained in more detail in Sec. IV, results in a global surface temperature anomaly of approximately $2.5\,^\circ$C, computed with respect to pre-industrial levels, and is in agreement with the two middle RCPs (RCP 4.5 and RCP 6.0) presented in Reference [1]. As a comparison, the most recent observations published by the National Ocean and Atmospheric Administration show that the atmospheric concentration of CO_2 has already reached 421 ppm*. In turn, a CO_2 concentration of 680 ppm could be reached already in 2055, according to the worst RCP predicted by the IPCC [1]. Policymakers and researchers are focusing on how to prevent catastrophic consequences on the Earth's ecosystems by reducing emissions of GHGs. In parallel, several methods to artificially modify the Earth's climate system have been proposed [2]. These methods are collectively known as *geoengineering* and they include both preventive (e.g., capturing CO_2 from the atmosphere [3]) and mitigation (e.g., solar geoengineering [4]) techniques. Geoengineering should be considered as a complementary set of methods to limit extreme climate consequences, while the international community works towards the goal of net-zero emission, and to prevent the climate system from reaching tipping points that would result in irreversible cascade effects [5]. So, by all means, geoengineering should not

---

*https://www.noaa.gov/news-release/carbon-dioxide-now-more-than-50-higher-than-pre-industrial-levels, accessed on 10th September 2022

be considered as a substitute of GHG emission reduction policies. However, the little amount of research conducted on geoengineering is still insufficient to conduct a proper assessment of its effects.

In this paper, only solar geoengineering is considered. Solar power is the main source of forcing in the Earth's climate system. The basic principle of solar geoengineering consists of blocking a fraction of the solar radiative flux reaching the Earth with the ultimate goal to offset the Earth's global energy balance. This solution would in principle allow to create and maintain an artificial climate system with increased atmospheric CO_2 content, balanced by lower levels of incoming solar radiation [6]. It should be mentioned that solar geoengineering not only has benefits. In the first place, it does not address the issue of ocean acidification. Secondly, it poses the risk of the so-called *termination effect*: this effect, particularly valid for space-based systems, refers to the possibility of returning to the natural solar irradiance levels very quickly, following an unexpected and sudden failure of the solar geoengineering system. This circumstance would result in a rapid rise in surface temperature. A broad survey collecting the opinion on space-based geoengineering of 125 experts in the field was conducted in Reference [7].

Previous studies analyzed the climate changes occurring with increased CO_2 levels and a subsequent reduction in the solar constant, focusing on the effects on the global surface temperature [8, 9], on its regional differences [10–12], on the hydrological cycle [13, 14], and on the transient climate dynamics [15]. Methods and techniques to minimize climate anomalies were also proposed [16–18]. Other studies treated the topic of a planetary sunshade in more detail, first exploring the concept in a general manner [19, 20], then focusing on the mission requirements [21] and on alternative mission architectures [22–25]. More in-depth studies researched several aspects of a space-based geoengineering mission: the sunshade's optimal location [6, 26], logistical challenges [27], orbit control techniques [28], spectrally selective materials for its fabrication [29], a possible roadmap towards its implementation [30], and its costs [31]. In particular, the latter study claims that, if the sunshade system has a mass smaller than 100 Mt and simultaneously ensures an insolation reduction of at least $0.8\,Wm^{-2}$ from 2050 to 2150, the economic costs of climate change caused by a 2xCO_2 scenario can be reduced by 240 billion USD from roughly 500 billion USD.

The vast majority of the studies concerned with space-based geoengineering focused on the concept of a static sunshade, continuously located at the displaced L_1 point. On the other hand, a considerable amount of climate studies consider a spatially and temporally distributed reductions in solar irradiance. Indeed, it was demonstrated extensively by climate scientists that a static sunshade (corresponding to a spatially and temporally uniform reduction in solar irradiance) produces overcooling in tropical regions and undercooling in polar regions [32]. If a dynamic sunshade is adopted, its trajectory can be tailored to selectively shade different latitudinal bands on the Earth depending on the day of the year. In particular, a slightly greater reduction in insolation should be achieved over the polar regions and a slightly smaller reduction over the tropics. Furthermore, there are very few studies that treat both the trajectory design and its impact on the climate simultaneously. The two aspects are tightly coupled, since the motion of the sunshade has a direct effect on the reduction of solar irradiance and thus on the climate. This coupling is particularly important when regional climate changes are accounted for.

This work aims to fill these research gaps by assessing whether a large, dynamic (i.e., capable of orbiting above and below the ecliptic plane) sunshade is capable of minimizing residual climate changes arising in the Earth's climate system with increased atmospheric CO_2 (680 ppm, twice the amount with respect to pre-industrial levels). It does so
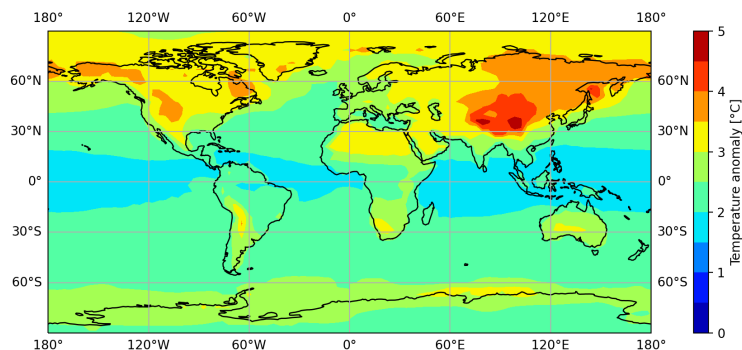

Fig. 1   Surface temperature anomaly after 50 years resulting from an instantaneous increase of atmospheric CO_2 to 680ppm. The simulation was performed with the GREB climate model; for more details, see Sec. VII.

4

by evaluating the performance of the sunshade's trajectory in the vicinity of the displaced L_1 point with a simplified climate model, which allows to account for the artificial solar irradiance distribution generated by a dynamic sunshade.

So far, only one study investigated the trajectory design of a dynamic sunshade to minimize residual regional climate changes [33]. In that study, a reverse-engineering approach was used to find optimal periodic orbits around the displaced L_1 point to tune the trajectory of the sunshade to the seasonal variations in the Earth's climate. This is achieved by linearly combining a set of static solutions with a non-zero displacement with respect to the ecliptic plane and subsequently connecting those solutions to create a periodic orbit.

In this work, a different approach, explained in Sec. IV, is proposed. Instead of using periodic orbits, a combination of equilibrium positions and time-optimal transfer between such equilibrium positions is used. The trajectory of the sunshade is controlled through the solar radiation pressure acceleration, the dynamical framework of which is presented in Sec. V. The shade cast on the Earth is computed with high accuracy (Sec. VI) and the artificial solar irradiance distribution is fed to a simplified climate model, presented in Sec. VII. The numerical methods used to optimize the motion of the sunshade are presented in Sec. VIII, while the results are discussed in Sec. IX. Conclusions are drawn in Sec. X.

IV. Problem Definition and Methodology

The approach used in this work to optimize the sunshade's trajectory is illustrated in Fig. 2. The trajectory over one year is composed of two separate parts: 1) the sunshade is alternately *parked* at two equilibrium points (one above the ecliptic plane during the summer and one below during the winter) and 2) the sunshade is transferred between the two equilibrium points (one transfer during spring and one during fall). As mentioned, the sunshade is placed below the ecliptic plane during the northern hemisphere winter and above the ecliptic plane during the northern hemisphere summer. This is done to ensure a greater reduction of insolation over the poles during local summer, while at the same time avoiding an excessively large insolation reduction over the equatorial regions. For most of the time during the year, the sunshade is located at either equilibrium points, which are in fact Artificial Equilibrium Points (AEPs): these equilibria are enabled by a given attitude of the sunshade [34, 35]. A formal definition of AEPs will be given in Sec. V.

The AEPs are connected by a time-optimal transfer trajectory. The transfer time is minimized to avoid overshading (and thus overcooling) of the equatorial regions. At a specific date during the northern hemisphere spring, the sunshade is transferred from an AEP below the ecliptic plane to an AEP above the ecliptic plane. After that, at another given date during the northern hemisphere fall, the same transfer is repeated. The details of the optimal control problem to find a minimum-time transfer trajectory are explained in Sec. VIII.A. The location of the AEPs, together with the departing dates of the transfer trajectory, are the independent variables that will be optimized in this work.

The insolation distribution resulting from the presence of the sunshade has both a temporal and a spatial dependency; however, in this paper, the spatial dependency is limited to latitudinal variations. This assumption is justified by the fact that longitudinal variations are relevant only if a sub-daily temporal resolution is required, yet this is not the case for this work. The artificial insolation distribution is then fed to a climate model (GREB), described in Sec. VII. The GREB model simulates surface temperatures on a regular grid of nodes, separated by $3.75°$ in latitude and longitude, based on a simplified global energy balance [36]. The insolation distribution derived from the presence of the sunshade is repeated for each year throughout the GREB simulation, which lasts for 50 years. Finally, the temperature anomalies are evaluated at the final year of the simulation and compared to a reference scenario corresponding to pre-industrial levels of atmospheric CO_2 and with a nominal solar radiation distribution [36]. The reference scenario is also computed by GREB with a 50-year-long climate simulation.

A few assumptions are made; assumed values of some quantities are reported in Table 1. The main sizing parameters for a static sunshade are its radius R_D and its distance from the Earth $r_{D,\oplus}$, which directly affect the mass of the sunshade. The minimization of the sunshade's mass, for a static sunshade located in the ecliptic plane along the Sun-Earth line, has been explored thoroughly in literature [6, 19, 20, 33]. Therefore, the values found in Reference [33] for the Earth-sunshade distance along the Sun-Earth line (as reported in Table 1) are adopted in this work. For a static sunshade with parameters as in Table 1, such assumptions ensure a global reduction in insolation of 1.7%, which has been proved as the minimum value to balance the climate effects of a doubling of the atmospheric CO_2 with respect to pre-industrial levels [6]. With respect to published work, in this paper the out-of-plane displacement of the sunshade is non-zero. However, the global insolation reduction obtained in this work will not differ significantly from 1.7%, since the out-of-plane component of the sunshade's location with respect to the Earth is roughly three orders of magnitude smaller than the Earth-sunshade distance. The upper limit placed on the out-of-plane displacement is derived by the fact that for a large out-of-plane displacement most of the shade would not be cast on the Earth. As a result, the in-plane
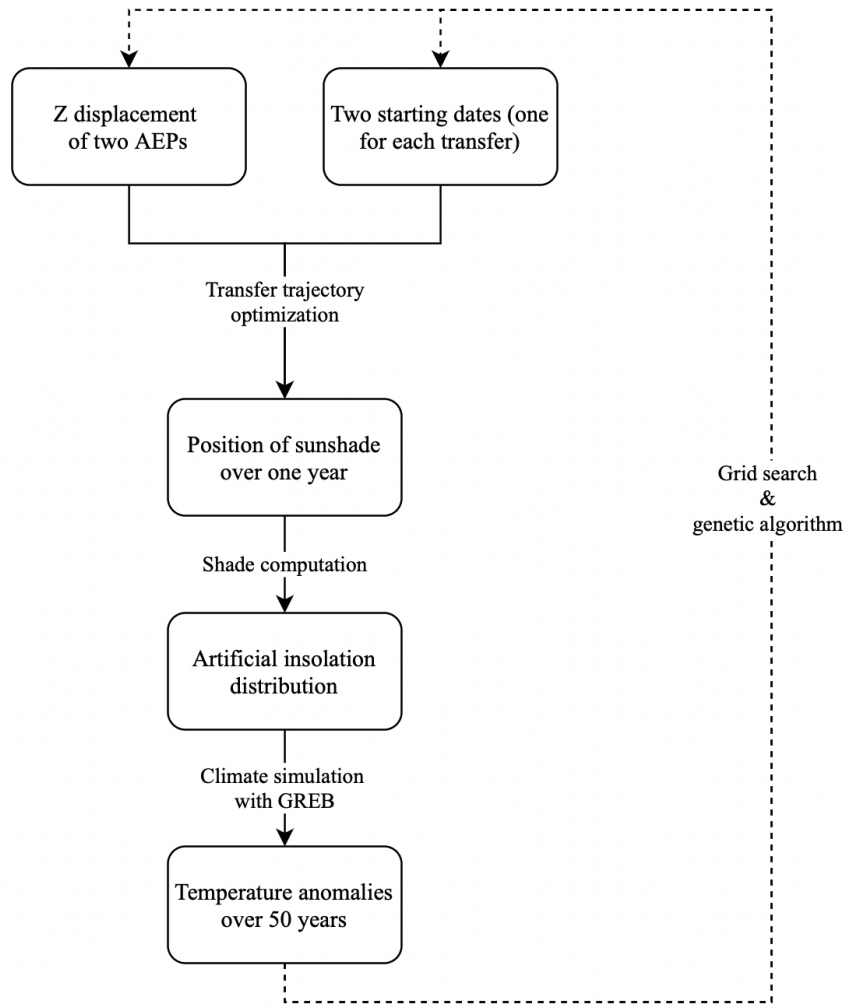
5

Fig. 2   Schematics of the methodology used in this work and described in Sec. IV.

AEP found in Reference [6] will be considered as a starting point. More details of the geometry of the system and on the AEPs are provided in Sec. V.

To select the optimal out-of-plane displacement of the AEPs and the dates on which the orbital transfers should be initiated, two methods are used in this paper: a grid search to explore the search space and a genetic algorithm. The settings used for the heuristic optimization are described in Sec. VIII.B, while the results are discussed in Sec. IX.

Table 1 Characteristic quantities for the sunshade and the climate model assumed in this work.

Quantity	Notation	Value	Unit	Source
Radius of the sunshade		1434	km	[33]
Distance of the sunshade from the Earth		$2.44 \cdot 10^6$	km	[33]
Pre-industrial levels of atmospheric CO_2		340	ppm	[36]

V. Dynamical Model

In this section, the dynamical model is presented in detail. The framework of the Circular Restricted Three-Body Problem is explained, together with the perturbing solar radiation pressure acceleration. The notation, reference frames, and the equations of motion are formulated in Sec. V.A. The section then focuses on the solar radiation pressure acceleration and how it can be exploited to control the orbital motion of the sunshade (Sec. V.B). Finally, the associated equilibrium solutions are discussed in Sec. V.C.

A. Circular Restricted Three-Body Problem

In this paper, the motion of the sunshade is designed in the framework of the Sun-Earth Circular-Restricted Three-Body Problem (CR3BP). It is therefore assumed that the sunshade is subject to the point-mass gravitational attraction of the primaries – the Sun (m_1) and the Earth (m_2) – neglecting the gravitational attraction of other celestial bodies in the solar system. In addition, since the mass of the sunshade, m, is negligible with respect to the mass of the primaries, the gravitational attraction exerted by the sunshade on the primaries is not considered [37]. Finally, the motion of the primaries around the barycenter of the system is assumed to be circular.

To describe the motion of the sunshade, a synodic (or corotating) reference frame (SRF), $S(\hat{\mathbf{x}}, \hat{\mathbf{y}}, \hat{\mathbf{z}})$, is introduced. The SRF, visualized in Fig. 3, is centered at the barycenter of the Sun-Earth system, O. One axis of the SRF, $\hat{\mathbf{x}}$, coincides with the vector connecting the primaries and is always oriented towards the smaller primary, m_2, while the $\hat{\mathbf{z}}$-axis coincides with the constant angular velocity vector, ω, describing the circular motion of m_1 and m_2 around the barycenter. The $\hat{\mathbf{y}}$-axis completes the right-handed reference frame. The position vectors of the Sun and the Earth in the SRF are denoted with $\mathbf{r}_1$ and $\mathbf{r}_2$, respectively, and the position of the sunshade with $\mathbf{r} = [x \quad y \quad z]^T$.

Under the assumptions presented in Sec. V.A, it is possible to describe the motion of the sunshade in the CR3BP in non-dimensional form by introducing new units of mass ($m_1 + m_2$), length ($|\mathbf{r}_1| + |\mathbf{r}_2|$), and time ($2\pi|\omega|^{-1}$). The characteristic parameter μ is also introduced:

$$\mu = \frac{m_2}{m_1 + m_2} \tag{1}$$

For the Sun-Earth system, this yields $\mu = 3.041464 \cdot 10^{-6}$ [38, 39]. As a result, the motion of the sunshade in the synodic reference frame expressed in dimensionless quantities is described as [37]:

$$\ddot{\mathbf{r}} = -\left(\frac{1-\mu}{r_{13}^3}\mathbf{r}_{13} + \frac{\mu}{r_{23}^3}\mathbf{r}_{23} \right) - 2\,\omega \times \dot{\mathbf{r}} - \omega \times (\omega \times \mathbf{r}) + \mathbf{a}_{SRP} \tag{2}$$

where $r_\square = |\mathbf{r}_\square|$. The first and second derivatives are denoted with single and double dots, respectively. The vector $\mathbf{a}_{SRP}$ represents the solar radiation pressure acceleration, which will be expanded and explained in more detail in Sec. V.B. Vectors $\mathbf{r}_{13}$ and $\mathbf{r}_{23}$, represented in Fig. 3, denote the position of the sunshade in the SRF with respect to the Sun and Earth, respectively, and are defined as:

$$\mathbf{r}_{13} = [x + \mu \quad y \quad z]^T \tag{3a}$$

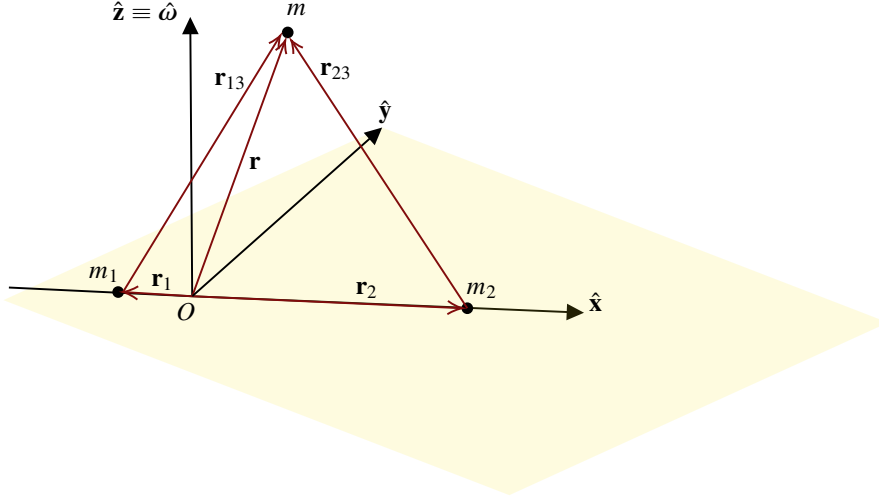$$\mathbf{r}_{23} = [x - (1 - \mu) \quad y \quad z]^T \tag{3b}$$

7

Fig. 3 The bigger primary (m_1), the smaller primary (m_2), and the planetary sunshade (m) represented in the synodic reference frame, S($\hat{x}$, $\hat{y}$, $\hat{z}$).

To further simplify the equations of motion (EOM), it is convenient to introduce the potential U [37]:

$$U = -\frac{1}{2}\left(x^2 + y^2\right) - \left(\frac{1-\mu}{r_{13}} + \frac{\mu}{r_{23}}\right) \tag{4}$$

so that the equation of motion (EOM) becomes:

$$\ddot{\mathbf{r}} = -2\omega \times \dot{\mathbf{r}} - \nabla U + \mathbf{a}_{SRP} \tag{5}$$

B. Solar Radiation Pressure Acceleration

As mentioned in Sec. V.A, for a large sunshade the solar radiation pressure acceleration should be accounted for. Indeed, especially in the vicinity of an equilibrium point, the magnitude of the solar radiation pressure acceleration is comparable to the gravitational accelerations exerted by the primaries [39]. Moreover, by changing the orientation of the sunshade, the acceleration vector can be controlled, similar to a solar sail [35]. The main advantage of exploiting solar radiation pressure to control the motion of the sunshade is that no propellant is required.

In this work, an ideal sail model is used to model the sunshade. An ideal sunshade reflects all photons in a specular manner; in other words, diffuse reflection, absorption, and emission are neglected. This type of sunshade is similar to an ideal mirror, whose performance could in theory be achieved by a sunshade constituted by a perfectly smooth membrane without wrinkles. Losses due to absorption, re-emission, and non-specular reflection are generally small compared to the magnitude of the reflective part: for realistic sunshades, approximately 94% of the incident radiation is reflected in the specular direction, with absorption coefficients as low as 0.04 [35]. Therefore, considering an ideal sunshade is justified in the context of this preliminary trajectory design study. The performance of an ideal sunshade with area A and mass m is uniquely characterized by the lightness number β, defined as follows:

$$\beta = \frac{mA}{\sigma} \tag{6}$$

where $\sigma = 1.53\,gm^{-2}$ is the critical solar sail loading parameter for the solar system [35]. The SRP acceleration $\mathbf{a}_{SRP}$ acting on the sunshade can be expressed as [35]:

$$\mathbf{a}_{SRP} = \beta\frac{1-\mu}{r_{13}^2}(\hat{\mathbf{r}}_{13} \cdot \hat{\mathbf{n}})^2\hat{\mathbf{n}} \tag{7}$$

As mentioned before, the solar radiation pressure acceleration depends on the sunshade's position and orientation with respect to the Sun, quantified in the SRF through vectors $\mathbf{r}$ and $\hat{\mathbf{n}}$ (the vector normal to the surface of the sunshade), respectively.
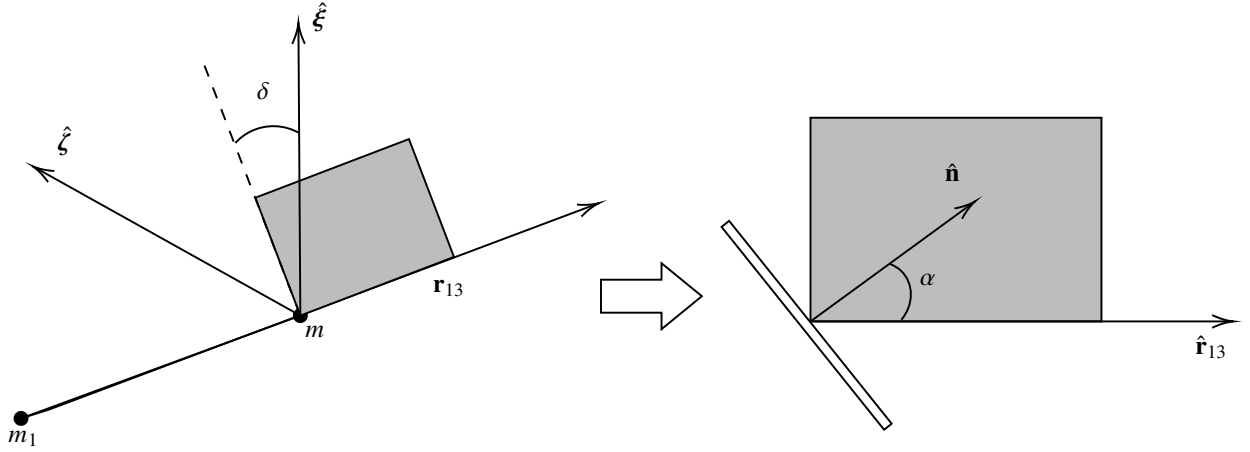
8

Fig. 4   Representation of the Local Reference Frame (LRF), L($\hat{\mathbf{r}}_{13}$, $\hat{\zeta}$, $\hat{\xi}$), adapted from Reference [40].

To define the attitude angle of the sunshade, a new reference frame is introduced, the Local Reference Frame (LRF), L($\hat{\mathbf{r}}_{13}$, $\hat{\zeta}$, $\hat{\xi}$) [35], represented in Fig. 4. The LRF is centered at the center of mass of the sunshade, with one axis that coincides with the vector connecting the Sun and the sunshade, $\hat{\mathbf{r}}_{13}$. The second axis is defined as:

$$\hat{\zeta} = \hat{\mathbf{z}} \times \hat{\mathbf{r}}_{13} \tag{8}$$

The third axis of the LRF, $\hat{\xi}$, completes the right-handed reference frame. The attitude of the sunshade can be defined by two angles: the cone angle α and the clock angle δ. The cone angle is defined as the angle between the direction normal to the sail, $\hat{\mathbf{n}}$, and the Sun-sunshade vector, $\hat{\mathbf{r}}_{13}$:

$$\alpha = \cos^{-1}\left(\hat{\mathbf{r}}_{13} \cdot \hat{\mathbf{n}}\right) \tag{9}$$

The clock angle is the angle between the projection of the acceleration vector onto the $\zeta\xi$ plane and the direction represented by $\hat{\xi}$:

$$\delta = \cos^{-1}\left\{\left[\hat{\mathbf{r}}_{13} \times (\hat{\mathbf{n}} \times \hat{\mathbf{r}}_{13})\right] \cdot \hat{\xi}\right\} \tag{10}$$

C. Equilibrium Solutions

If the perturbing acceleration $\mathbf{a}_{SRP}$ is neglected, five classical equilibrium solutions can be found by substituting $\mathbf{r} = \dot{\mathbf{r}} = \mathbf{a}_{SRP} = \mathbf{0}$ into Eq. 5, yielding $\nabla U = \mathbf{0}$. These solutions correspond to the five Lagrangian points: three collinear points (with $x = 0$) and two equilateral points (with $x \neq 0$). For obvious reasons, the first Lagrangian point, L_1, is an ideal location for a planetary sunshade, as it is located between the Sun and the Earth throughout the revolving motion of the Earth around the Sun, without the need of performing large orbital maneuvers.

The addition of the solar radiation pressure acceleration expands the set of five equilibrium points to an *infinite* set of equilibrium solutions (again derived from Eq. 5):

$$\nabla U = \mathbf{a}_{SRP} \tag{11}$$

From Eq. 11, it is clear that the equilibrium solutions depend on the characteristics of the sunshade through the term $\mathbf{a}_{SRP}$ [34]. These equilibrium solutions are often called *(solar sail) displaced* equilibrium points or Artificial Equilibrium Points (AEPs) and they will be useful for the remainder of this work. A representation of a set of selected equilibrium solutions for the Sun-Earth CR3BP is reported in Fig. 5. Contour lines and arrows represent the lightness number and sunshade orientation, respectively, that are required to achieve equilibrium. It can be noticed from Fig. 5 that achieving equilibrium in certain locations is not possible. This is due to the fact that the SRP acceleration can only be oriented away from the Sun. Furthermore, it is also clear from Fig. 5 that a static sunshade in the ecliptic plane must be located between the Sun and the classical L_1 point; in addition, to increase the distance from L_1 corresponds a larger lightness number is required.
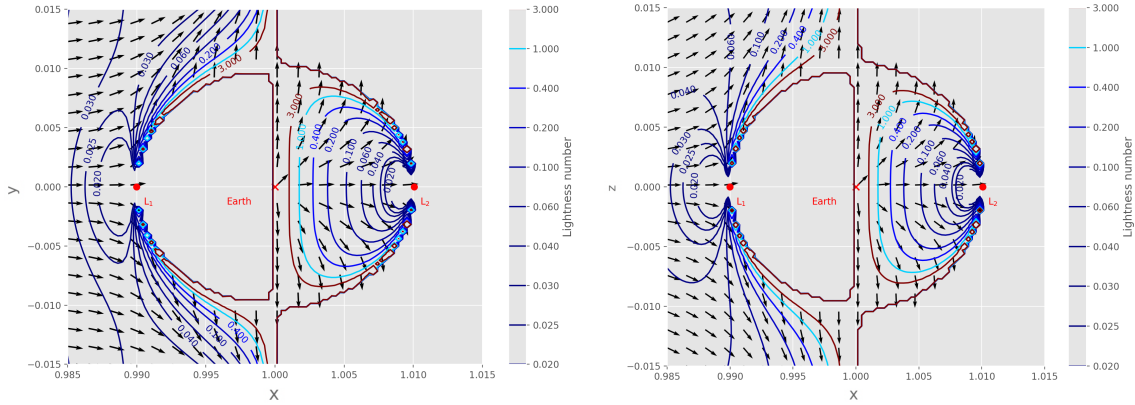
9

Fig. 5 **Distribution of Artificial Equilibrium Points in the vicinity of the Earth, plotted in the xy-plane (left panel) and in the xz-plane (right panel). The required lightness number β is represented by countour levels, while the required sunshade orientation is indicated by black arrows.**

VI. Insolation

The focus of the paper is now shifted towards the computation of the solar irradiance and of its reduction due to the sunshade. Fundamental quantities are introduced below. The spatio-temporal distribution of the natural insolation received by the Earth is presented in Sec. VI.A, while different eclipse conditions are described in Sec. VI.B. The section is concluded with the explanation of the solar limb darkening model adopted for this work (Sec. VI.C).

The irradiance, S, is defined as the power emitted or received by a unit surface [41]. The solar irradiance received by the Earth, averaged over one year, is usually referred to as the solar constant, S_0. According to the most recent satellite measurements [42], its value oscillates between 1360 and 1365 Wm^{-2}, depending on the eleven-year solar cycle. The irradiance can be converted to the radiance, I, which is defined as the radiating power emitted or received by a unit surface per unit solid angle [41]:

$$S = \Omega I \tag{12}$$

where Ω is the solid angle subtended by a generic surface. These definition will be useful for the remainder of this section.

A. Natural Insolation

Solar irradiance is a good metric to evaluate the global energy balance of the Earth. However, since it is defined as the solar flux reaching a unit surface perpendicular to the direction of solar radiation, it is not a suitable metric to evaluate its impact on the Earth's climate. A more representative quantity in this context is the insolation, Q, that adjusts the value of the solar constant for different locations on the Earth and for different times during the year. The temporal dependency is expressed through the varying Sun-Earth distance, $r_{\oplus}$, while the spatial dependency is quantified by the solar zenith angle, ψ, as follows [43]:

$$Q = S_0 \left(\frac{\bar{r}_{\oplus}}{r_{\oplus}} \right)^2 \cos \psi \tag{13}$$

with $\bar{r}_{\oplus}$ the average Sun-Earth distance (1 AU). The solar zenith angle, ψ, is defined as the angle between the normal to the Earth's surface at a given point P and the direction in which solar radiation reaches at the same point [43]. The solar zenith angle depends on the latitude, on the season, and on the time of day as follows [43]:

$$\cos \psi = \sin \lambda \sin \nu + \cos \lambda \cos \nu \cos h \tag{14}$$

All quantities from Eq. 14 are depicted in Fig. 6. The latitudinal dependence is expressed through the latitude angle λ, while the seasonal dependence is expressed via the declination angle ν, which is the latitude of the point on the Earth's surface where the Sun is at zenith at noon. The time of the day is expressed via the hour angle, which is the longitude of point P during the day, expressed with respect to its position at noon [43]. Equation 14 holds everywhere on Earth,

except at the poles: in the summer hemisphere, latitudes higher than $\lambda = 90° - v$ are in constant daylight, while in the winter hemisphere such locations are not reached by sunlight at all.

It is possible to find the daily average of Eq. 13, $\overline{Q}$, by computing the integral over all hour angles between $-h_0$ (hour angle at sunrise) and $+h_0$ (hour angle at sunset) [43]:

$$\overline{Q} = \frac{S_0}{\pi} \left(\frac{\bar{r}_\oplus}{r_\oplus}\right)^2 (h_0 \sin \lambda \sin v + \cos \lambda \cos v \cos h_0) \tag{15}$$

The insolation distribution resulting from Eq. 15 is reported in Fig. 7. The contour lines denote the insolation level, while the dashed line shows the latitude of the subsolar point at local noon. It can be noticed that the poles do not receive any insolation (constant darkness) during local winter; on the other hand, during local summer, they receive the greatest amount of insolation, due to the tilt of the Earth's spinning axis. Finally, the latitude of the subsolar point at local noon (dashed line) oscillates between the latitude of the tropic of Cancer (reached on the summer solstice) and the tropic of Capricorn (reached on the winter solstice).
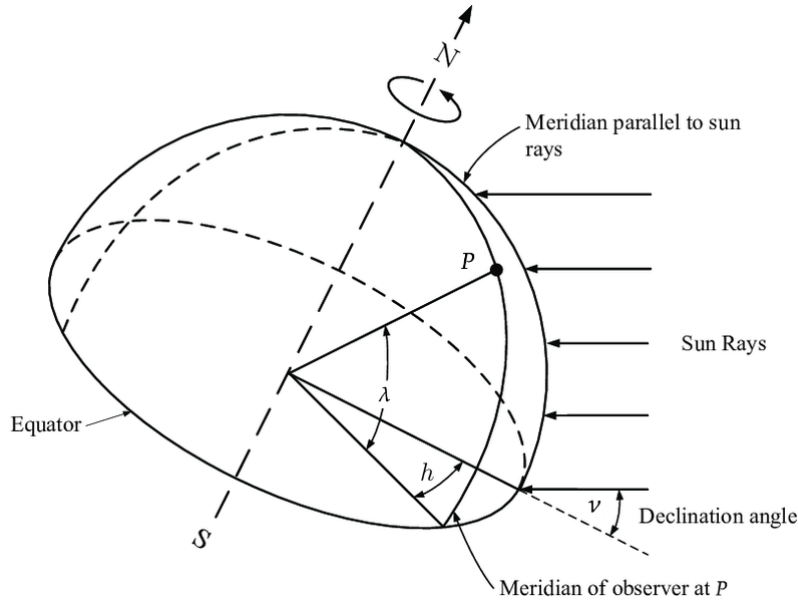

Fig. 6 Representation of the latitude angle, λ, the declination angle, v, and the hour angle, h (adopted from Reference [44]).

B. Radiance reduction under eclipse conditions

The attention is now shifted towards the computation of the radiance reduction due to the shade. In the presence of a radiating body (usually the Sun) and a shading body, four different eclipse regions arise: the fully illuminated region, the *umbra* region (total eclipse), the *penumbra* region, and the annular eclipse region. These regions are represented in Fig. 8 and are denoted as follows:

$$I = \begin{cases} I_0 & \text{fully illuminated} \\ I_{\text{pe}} & \text{partial eclipse} \\ I_{\text{ae}} & \text{annular eclipse} \\ 0 & \text{total eclipse} \end{cases} \tag{16}$$

with $0 < I_{\text{pe}} < I_0$ and $0 < I_{\text{ae}} < I_0$. Most methods available in literature to compute the eclipse condition of an orbiting body are derived for satellites in Low Earth Orbit (LEO), therefore the main objective of these methods is to determine whether a spacecraft is in total eclipse or, alternatively, fully exposed to sunlight, but nothing in between (see References [45, 46]). These methods are therefore not suitable for the purpose of this work, where the radiance reduction due to partial or annular eclipses has to be determined. As a result, the method described in Reference [47] is adopted. The
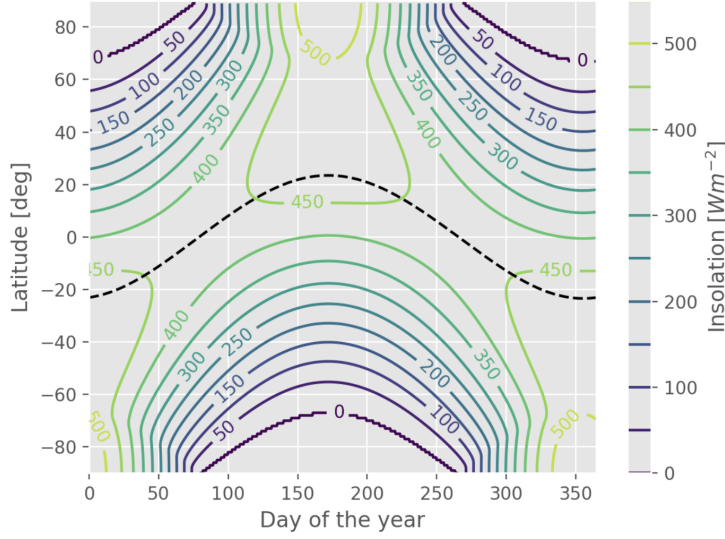
Fig. 7 **Insolation received by the Earth in nominal conditions over one year ($S_0 = 1360\,\mathrm{Wm^{-2}}$). Countour levels indicate the insolation, while the dashed line denotes the latitude of the subsolar point at local noon.**

radiating body (the Sun) is assumed to be perfectly spherical and the radius of its projected disk is denoted by $R_\odot$; the planetary sunshade is assumed to be perfectly circular and its radius is denoted by R_D. The Sun and the sunshade are centered at points S and D, respectively, as indicated in Fig. 8. The sufficient conditions for each eclipse region are reported in [47]. To quantify the insolation reduction due to the shade, vectors $\mathbf{r}_{\odot,P}$ and $\mathbf{r}_{D,P}$ are introduced, denoting the position of the Sun and the sunshade with respect to a generic point P on the Earth's surface, respectively. Solid angles $\Omega_\odot$ and Ω_D, quantifying the angular radius of the Sun and the sunshade respectively, are also introduced:

$$\Omega_\odot = \sin^{-1}\left(\frac{R_\odot}{r_{\odot,P}}\right) \tag{17}$$

$$\Omega_D = \sin^{-1}\left(\frac{R_D}{r_{D,P}}\right) \tag{18}$$

The parameter η, denoting the angular separation between the Sun and the sunshade, is defined as [47]:

$$\eta = \cos^{-1}\left(\frac{\mathbf{r}_{\odot,P} \cdot \mathbf{r}_{D,P}}{r_{\odot,P} \cdot r_{D,P}}\right) \tag{19}$$

The radiance under partial eclipse condition, I_{pe}, can then be computed as follows [47]:

$$I_{\mathrm{pe}} = I_0 \left\{ 1 - \frac{1}{\pi\left(1 - \cos\Omega_\odot\right)}\left[\pi - \cos\Omega_\odot \cos^{-1}\left(\frac{\cos\Omega_D - \cos\Omega_\odot \cos\eta}{\sin\Omega_\odot \sin\eta}\right) + \right.\right. \tag{20}$$

$$\left.\left. - \cos\Omega_D \cos^{-1}\left(\frac{\cos\Omega_\odot - \cos\Omega_D \cos\eta}{\sin\Omega_D \sin\eta}\right) - \cos^{-1}\left(\frac{\cos\eta - \cos\Omega_\odot \cos\Omega_D}{\sin\Omega_\odot \sin\Omega_D}\right)\right]\right\}$$

while the radiance in annular eclipse, I_{ae}, can be computed as follows [47]:

$$I_{\mathrm{ae}} = I_0 \left(1 - \frac{1 - \cos\Omega_D}{1 - \cos\Omega_\odot}\right) \tag{21}$$

Given the geometry of the Sun–sunshade–Earth system under the assumptions presented in Sec. IV, the Earth's surface is never in total eclipse, but it oscillates between annular eclipse and partial eclipse, depending on the relative position of the sunshade.
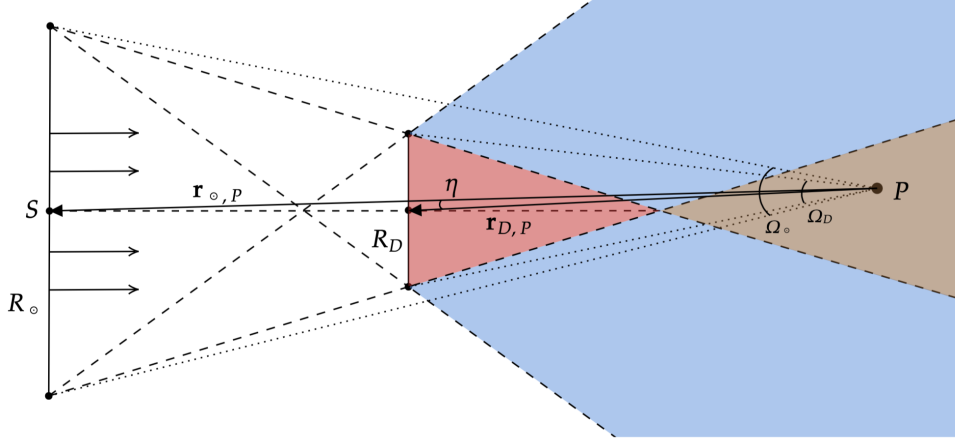
Fig. 8 **Different eclipse conditions produced by a planetary sunshade of radius R_D located at a distance** $|\mathbf{r}_{\odot,P} - \mathbf{r}_{D,P}|$ **from the Sun: fully illuminated (white), partial eclipse (blue), annular eclipse (brown), and total eclipse (red). Solid angles $\Omega_\odot$ and Ω_D, subtended by the Sun and the sunshade at point P, respectively, are also represented.**

C. Solar Limb Darkening

Equations 20 and 21 are based on the assumption that the illuminating body radiates homogeneously. However, this assumption is not justified when a planetary sunshade is present. Indeed, the apparent solar luminosity is larger at the center of the solar disk and smaller at its outer edges [48]. The radial dependency of the apparent solar luminosity, known in literature as *limb darkening*, has the direct implication that the same sunshade shading different regions of the solar disk results in different radiance distributions on the Earth's surface. Most limb darkening models available in literature are empirical and are based on polynomial interpolations of solar observations (e.g., [49]). In this work, the second-degree polynomial approximation proposed in Reference [50] (computed for a mean wavelength of 550 nm) is adopted. The geometry of the model is described in Fig. 9. The limb darkening can then be computed as follows [50]:

$$I_r = I_c \left(c_0 + c_1 \cos\gamma + c_2 \cos^2\gamma \right) \tag{22}$$

where I_c is the radiance emitted by the center of the Sun and I_r is the radiance emitted by the Sun at a radial distance d_r from its center. c_0, c_1, and c_2 are empirical coefficients and their values are assumed from Reference [50] ($c_0 = 0.3$, $c_1 = 0.93$, and $c_2 = -0.23$). With this set of coefficients, it is assumed that the brightness of the Sun at its limb is equal to 30% of the brightness at its center. The radial distance, d_r, is related to the angle γ as follows:

$$\frac{d_r}{R_\odot} = \sin\gamma \tag{23}$$

As a result, the radiance seen by an observer in fully illuminated conditions, I_0, results in:

$$I_0 = \int_0^{R_\odot} I_r(d_r) \, \mathrm{d}\, d_r \tag{24}$$

where the integral spans the entire radial extension of the Sun. In this paper, Eq. 24 is discretized over ten different values of the radial distance to reduce the computational effort. A representation of this approximation is reported in Fig. 10. The ten values are discretized in the range $0 < \frac{I_r}{I_c} < 1$ so that the radiance emitted by a solar ring between two adjacent nodes of radial distance is the same for all pairs of radial distances. This is an improvement in accuracy with respect to the method used in Reference [33], where the discretization was based on regularly spaced values of the radius of solar disks.
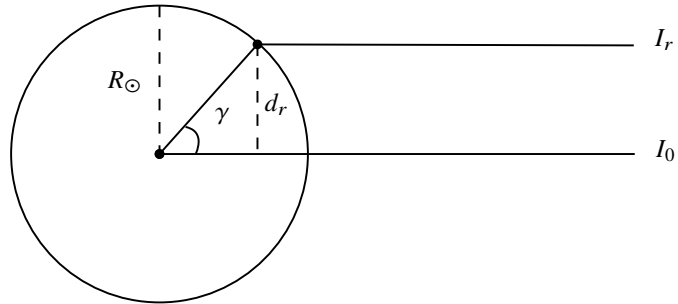
Fig. 9 **Geometry of solar limb darkening: the radiance emitted by the Sun decreases with increasing radial distance d_r.**
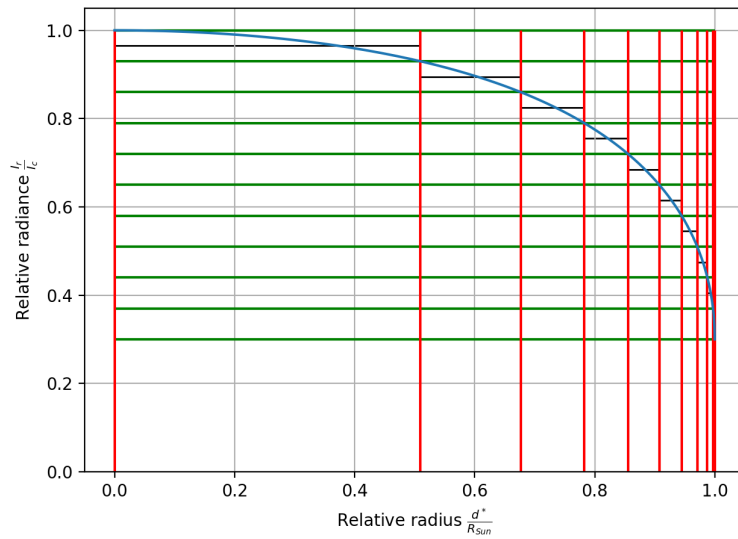

Fig. 10 **Discretization of solar limb darkening: empirical law representing Eq. 22 (blue), ten equidistant levels of relative radiance (green), and resulting discrete levels for the relative radius (red).**

VII. Quantification of Climate Changes

The effect of the reduced insolation due to the sunshade produces an effect on the Earth's climate. Since the climate is a complex system, it is difficult to optimize the resulting latitudinal and seasonal insolation distribution without any data related to the climate itself [51]. Therefore, in this work a climate model is used to quantify the impact of the sunshade. Climate models are usually grouped into three classes of increasing complexity: Energy Balance Models (EBMs, [52]), Earth Models of Intermediate Complexity (EMICs, [53]), and Global Circulation Models (GCMs, [54]). Although EMICs and GCMs accurately reproduce most climate features, they are very computationally expensive and not suitable to be run within an optimization loop. Therefore, a specific EBM, the Globally Resolved Energy Balance (GREB) model, is adopted [36]. The choice is motivated by two factors. Firstly, GREB is the only globally resolved EBM available in literature. Thus, it is possible to supply the model with a latitude-dependent insolation distribution, rather than a single value, like it would be when considering a uniform reduction in the solar constant [55]. Secondly, GREB was used in the work in Reference [33], which enables cross-validation and comparison of the results.

GREB is based on a simplified energy balance and accounts for several sources of heat flux, F: the heat flux from shortwave (solar), F_{solar}, and longwave (thermal) radiation, $F_{thermal}$, the heat exchanged within the atmospheric hydrological cycle, F_{latent}, the heat flux exchanged with the deep oceans, F_{ocean}, and the sensible heat flux, F_{sense}. Heat transfer via atmospheric circulation (advection and diffusion) is also accounted for. Such processes are modeled in a simplified way that prioritizes computational efficiency over accuracy. It features three different layers (a single-slab atmosphere, surface land, and a single-layer deep ocean) resolved on a grid of 3.75° x 3.75° in latitude (angle λ) and longitude (angle φ). The grid's spatial resolution corresponds to roughly 400 km, which is comparable to the resolution of several GCMs [54]. The temperature at each node of these three layers (atmosphere, land surface, and ocean) represent GREB's main prognostic variables [36]: $T_{atm}(\lambda, \varphi, t)$, $T(\lambda, \varphi, t)$, $T_{ocean}(\lambda, \varphi, t)$, where t denotes the time dependency. The land surface energy balance is described by the following equation (it is noted that energy balance equations for the atmosphere and the deep ocean have similar forms, therefore they are not reported here):

$$\tau_{surf}\frac{dT}{dt} = F_{solar} + F_{thermal} + F_{latent} + F_{ocean} + F_{sense} + F_{correct} \qquad (25)$$

where T is the surface temperature and τ_{surf} its heat capacity. The term $F_{correct}$ represents empirical corrections: indeed, for most EBMs and EMICs, models are adjusted with empirical values to correct for deviations due to model biases [36]. This correction is achieved by performing a shorter climate simulation that computes the heat fluxes needed to maintain the prognostic variables equal to their observed counterparts. It is of interest for this work to expand the forcing term quantifying the shortwave radiative energy flux, F_{solar}, as follows:

$$F_{solar} = (1 - \chi_{clouds})(1 - \chi_{surf})Q \qquad (26)$$

where Q is the insolation introduced in Eq. 15, while χ_{clouds} and χ_{surf} are the cloud and surface albedo, respectively. Introducing a planetary sunshade affects the insolation Q and its temporal and latitudinal distribution, which in turn plays a role in the surface temperature via the GREB model equations. The GREB model needs a set of historical average climatologies as input data, both to estimate the empirical corrections (surface temperature, atmospheric temperature, and deep ocean temperature) and to provide the model with boundary conditions (horizontal winds, CO_2 levels, topographic height, surface wetness, ocean mixed layer depth, and cloud cover). While GREB is unable to reproduce small-scale and short-term climate variability (i.e., weather fluctuations), it is a reasonably accurate and particularly fast tool to evaluate global trends in climate change due to modifications in the external forcings [33, 36, 55]. Simulating 50 years of climate evolution takes approximately 10 minutes on a standard Personal Computer (PC), as reported also in Reference [33]. However, caution should be exerted, since GREB — like all EBMs — does not include *all* types of climate feedback. It is therefore unable to reproduce small-scale climate changes that could be of great importance when it comes to evaluating the impact of a geoengineering scheme. The authors of the models claim that its uncertainties are comparable to the models used by the International Panel on Climate Change (IPCC) [36]. Still, more accurate models should be used when a more precise assessment of solar geoengineering schemes are needed. GREB was originally written in Fortran and its source code, together with the required input data, are freely available through [36]. For the purpose of this work, the source code was converted into Python code; the input data were taken from [36].

In the remainder of this work, four different climate simulations are performed with GREB. The first climate simulation (case A), denoted by the subscript $\square_{ref}$, is a reference scenario with pre-industrial levels of atmospheric CO_2 content (see Table 1) and the natural insolation distribution. The second climate simulation (case B), denoted by the subscript $\square_{2xCO2}$ is the same as case A, but with doubled amount of atmospheric CO_2 content (680ppm). The third and

Table 2 Climate scenarios considered.

Case	Name	Notation	CO_2 [ppm]	Sunshade
A	Reference	$\square_{\text{ref}}$	340	Absent
B	2xCO2	$\square_{\text{2xCO2}}$	680	Absent
C	Geoengineering - static	$\square_{\text{geo}}^{\text{static}}$	680	Static
D	Geoengineering - dynamic	$\square_{\text{geo}}^{\text{dynamic}}$	680	Dynamic

fourth climate simulations (case C and D), denoted by the subscript $\square_{\text{geo}}$, are the same as case B, but with an artificial insolation distribution, with the latter varying according to the sunshade trajectory and configuration. All the scenarios considered in this work are summarized in Table 2.

VIII. Numerical optimization

In this section, the numerical optimization techniques used in this work are described. The optimal control problem to find a time-optimal transfer trajectory connecting two given artificial equilibrium points is introduced in Sec. VIII.A. The optimal control problem constitutes the "inner" loop of the pipeline described in Fig. 2 (i.e., it is part the "transfer trajectory optimization" process in Fig. 2). Furthermore, the heuristic optimization problem and the associated genetic algorithm used are described in Sec. VIII.B. The heuristic optimization constitutes the "outer" loop of the pipeline described in Fig. 2.

A. Transfer Trajectory Optimization

As anticipated in Sec. IV, the transfer trajectory between artificial equilibrium points is found by solving an optimal control problem [56, 57]. In this work, a direct method based on collocation is used. Direct methods convert (or *transcribe*) an optimal control problem into a finite non-linear programming (NLP) problem. This is achieved by dividing the trajectory into segments through a mesh of nodes (spaced, for example, in time). Across each segment, the state and control variables are approximated by means of polynomial interpolation. In this work, both the state and control variables are discretized on the time domain using Lagrange-Radau polynomials [58]. At the boundaries of the segment, the polynomial must satisfy the dynamical constraints. In addition, at one or more points within the segment (called *collocation* points), the interpolated derivatives are compared to the derivatives computed through the EOM. The difference, called *defect*, is minimized by the solver [56]. Considering all segments of the trajectory, a set of algebraic equations expressed in terms of the state and control variables emerges.

In this work, the state variables $\mathbf{X}_1(t)$ are the position and velocity components of the sunshade in the SRF:

$$\mathbf{X}_1(t) = \begin{bmatrix} x & y & z & \dot{x} & \dot{y} & \dot{z} \end{bmatrix}^T \tag{27}$$

The control variables $\mathbf{U}(t)$ are the components of the vector normal to the sail, introduced in Sec. V.B, expressed in the SRF:

$$\mathbf{U}(t) = \hat{\mathbf{n}} = \begin{bmatrix} n_x & n_y & n_z \end{bmatrix}^T \tag{28}$$

The objective function J_1 to be minimized is the time of flight:

$$J_1 = t_f - t_i \tag{29}$$

where t_i and t_f are the times corresponding to the start and end of the transfer trajectory, respectively.

Several constraints are imposed. Dynamic constraints, represented by the equation of motions (Eq. 5), are imposed. Additionally, two path constraints are formulated. The first path constraint ensures that the norm of the control vector equals unity:
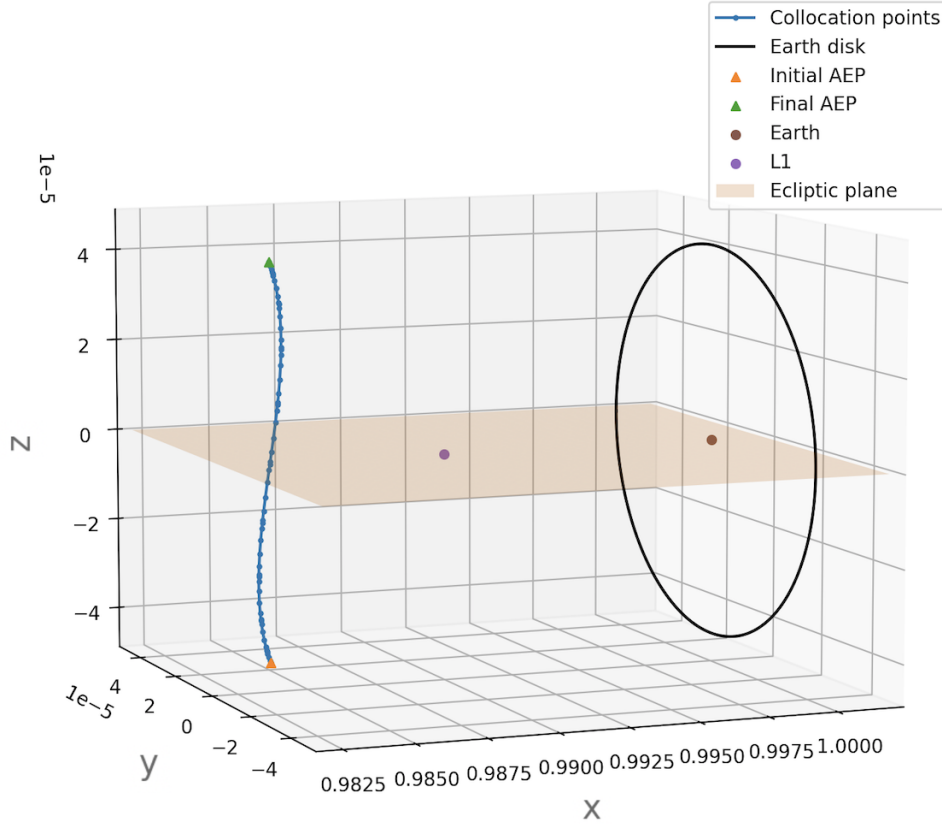
$$|\mathbf{n}| = 1 \tag{30}$$

Fig. 11 Time-optimal transfer trajectory originating from $z = -R_\oplus$ and ending at $z = +R_\oplus$. It is noted that the z-axis is stretched with respect to the x- and y-axes.

The second path constraint ensures that the SRP acceleration vector points away from the Sun [35]:

$$\mathbf{r}_{13} \cdot \hat{\mathbf{n}} \geqslant 0 \tag{31}$$

Boundary conditions are also imposed on the initial and final state and control variables:

$$\mathbf{X}_1(t_i) = \mathbf{X}_i \tag{32a}$$
$$\mathbf{X}_1(t_f) = \mathbf{X}_f \tag{32b}$$
$$\mathbf{U}(t_i) = \mathbf{U}_i \tag{32c}$$
$$\mathbf{U}(t_f) = \mathbf{U}_f \tag{32d}$$

The first two equations ensure that the transfer trajectory of the sunshade begins and ends at given AEPs, while the last two equations ensure that equilibrium is satisfied at the start and end locations. In this work, the problem was discretized by dividing the time of flight, $t_f - t_i$, in ten segments. Each segment was composed of six collocation points. For some trajectories, variations of these settings have been performed in order for the problem to converge. For all the other settings, default values are used. An open-source, Python-based optimization modeling package, called Pyomo, is used [59]. Pyomo relies on the Interior Point Optimizer (IPOPT), an open-source package for large-scale optimization [60]. Pyomo allows users to model the optimization problem and use direct methods to transcribe a dynamic optimization problem into a large-scale, sparse, static optimization problem through collocation methods. The NLP problem is then solved by IPOPT.

An example of a transfer trajectory between two AEPs is reported in Fig. 11, while the attitude angles required to achieve such a trajectory are plotted in Fig. 12. The transfer starts at $z = -R_\oplus$ and ends at $z = +R_\oplus$, taking approximately 56 days. It is possible to notice how the trajectory and the cone angle profile are rather symmetric with
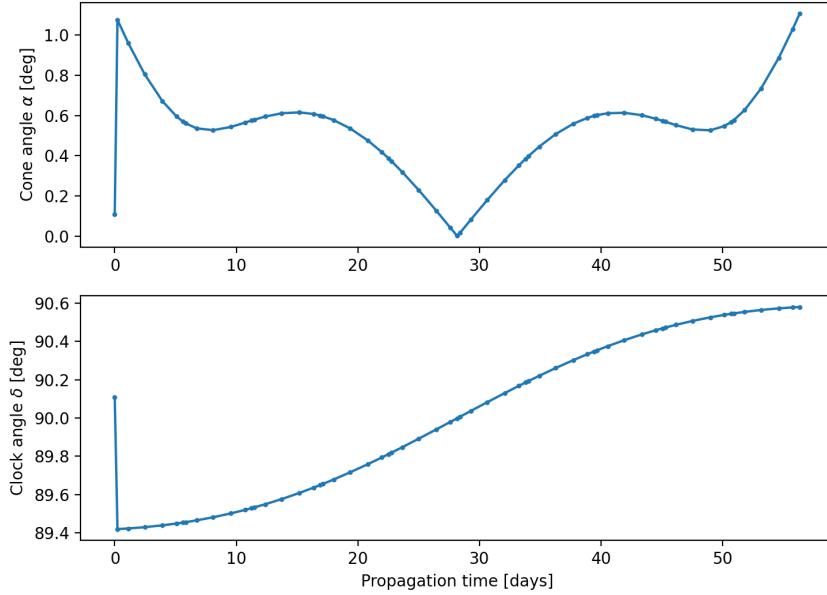
17

Fig. 12 Attitude angles required to achieve the transfer trajectory presented in Fig. 11. Top panel: cone angle, α; bottom panel: clock angle, δ.

respect to the midpoint of the transfer. These features are directly related to the fact that the ecliptic plane is a plane of symmetry for the CR3BP. Furthermore, given the relatively small distance travelled by the sunshade, the attitude angle shows small variations, in the order of $1°$. Given that the objective is to minimize the transfer time, the trajectory results in a nearly-straight, elongated transfer, with a very large variation in the z-coordinate and small variations for the x- and y-coordinates.

B. Minimization of Temperature Anomalies

As stated in Sec. IV, the goal of this work is to optimize the location of the sunshade over a full year to minimize latitudinal temperature anomalies. For this purpose, three different problems are defined, each with a different objective, and then solved via a genetic algorithm. This process corresponds to the "outer" loop reported in Fig. 2. However, before doing so, the design space is explored through grid searches that analyze the relation between the independent variables and two of the three objective functions. All the optimization problems explained below are unconstrained and single-objective.

The objectives used for the optimization are threefold. The first two objectives are also used as dependent variables in the grid searches. First, an objective function J_{RMS} that quantifies the latitudinal distribution of temperature anomalies is considered, as suggested by Reference [33]. The GREB model produces monthly means of surface temperature data for each node of the spatial grid. This is denoted as $\bar{T}(\lambda, \varphi, i)$, with index $i = 0, 1, \ldots, 11$ referring to the month of the year; as presented in Sec. VI, the latitudinal and longitudinal dependencies are respectively denoted by the latitude angle λ and the longitude angle φ. The overbar indicates that this quantity is a monthly average. The spatial grid is discretized through 96 points over the longitude and 48 points over the latitude, resulting in 4608 nodes and a spatial resolution of $3.75°$ (corresponding to roughly 400 km, as stated in Sec. VII). For such a grid, the longitudinally averaged temperature is:

$$\bar{T}(\lambda, i) = \frac{1}{96} \sum_{\varphi=0°}^{360°} \bar{T}(\lambda, \varphi, i) \tag{33}$$

From Eq. 33, the temperature anomaly is computed by taking the difference between the double-CO_2 geoengineering

18

scenario (subscript $\square_\text{geo}$) and the reference scenario (subscript $\square_\text{ref}$):

$$\Delta\bar{T}(\lambda, i) = \bar{T}_\text{geo}(\lambda, i) - \bar{T}_\text{ref}(\lambda, i) \tag{34}$$

Then, the root mean squares (RMS) is used to account for both negative and positive temperature anomalies over time:

$$\Delta\bar{T}(\lambda) = \sqrt{\frac{1}{12} \sum_{i=0}^{11} \Delta\bar{T}^2(\lambda, i)} \tag{35}$$

Finally, the resulting values are averaged over latitude weighted for the surface area corresponding to each latitudinal grid point. The surface area for each grid point, $\Delta A(\lambda, \varphi)$, can be computed as [61]:

$$\Delta A(\lambda, \varphi) = R_\oplus^2 \, \Delta\lambda \, \Delta\varphi \cos\lambda \tag{36}$$

Equation 36 represents both the case where the Earth radius is latitude-dependent (ellipsoidal Earth model) or constant (spherical Earth model). In this work, a spherical Earth model is used; therefore, for a regularly spaced grid as the one used in this work, the surface area $\Delta A(\lambda)$ is only latitude-dependent. The objective function sought for can then be defined as:

$$J_\text{RMS} = \sum_{\lambda=-90°}^{90°} \Delta A(\lambda) \Delta\bar{T}(\lambda) \tag{37}$$

It should be noted that the objective function J_RMS is only computed over the last year of the simulation (50$^\text{th}$ year). It is also possible to include a filter after Eq. 35, so that only statistically relevant temperature anomalies are accounted for. This method was proposed in Reference [33], using a threshold of statistical relevance of 0.1°C.

The second objective function, J_GMST, quantifies the global temperature anomaly, without accounting for regional or latitudinal differences. The surface temperature is averaged by longitude, by latitude, and by month of the year, to obtain the Global Mean Surface Temperature (GMST), denoted by $\bar{T}^\text{global}$:

$$\bar{T}^\text{global} = \frac{1}{96}\frac{1}{48}\frac{1}{12} \sum_{\varphi=0°}^{360°} \sum_{\lambda=-90°}^{90°} \sum_{i=0}^{11} \bar{T}(\lambda, \varphi, i) \tag{38}$$

Subsequently, the global mean surface temperature, $\bar{T}^\text{global}$, is used to compute the temperature anomaly:

$$J_\text{GMST} = \bar{T}_\text{geo}^\text{global} - \bar{T}_\text{ref}^\text{global} \tag{39}$$

In this case, it is also possible to introduce a filtering scheme to discard statistically insignificant values.

Finally, it is also useful to introduce a third objective function, J_polar, that quantifies the Polar Mean Surface Temperature (PMST) anomaly. This is essentially a variation of the objective function J_GMST, computed only over the polar regions. In this work, polar regions are defined as regions with latitude $|\lambda| > 67.5°$. Therefore, Eq. 38 can be transformed into:

$$\bar{T}^\text{polar} = \frac{1}{96}\frac{1}{12}\frac{1}{12} \sum_{\varphi=0°}^{360°} \sum_{i=0}^{11} \left(\sum_{\lambda=-90°}^{-67.5°} \bar{T}(\lambda, \varphi, i) + \sum_{\lambda=67.5°}^{90°} \bar{T}(\lambda, \varphi, i) \right) \tag{40}$$

yielding:

$$J_\text{polar} = \bar{T}_\text{geo}^\text{polar} - \bar{T}_\text{ref}^\text{polar} \tag{41}$$

The objective function formulated in Eq. 41 is useful to evaluate the sunshade's performance over the poles, which are sensitive regions for climate change showing the largest surface temperature increase.

The independent variables of all optimization problems are the following, grouped in the decision vector $\mathbf{X}_2$:

$$\mathbf{X}_2 = \begin{bmatrix} z_S & z_N & t_S & t_N \end{bmatrix}^T \tag{42}$$

Quantities z_S and z_N denote respectively the vertical displacement of the AEPs below (subscript $\square_S$) and above (subscript $\square_N$) the ecliptic plane. As presented in Sec. IV, the x- and y-coordinates of the AEPs are fixed and their values are reported in Table 1, therefore only the z-coordinate is optimized. As a result, the optimal AEP found will not be a true equilibrium point. Analogously, t_S and t_N denote the time when the transfer from south to north and from north to south

19

start, respectively. Both t_S and t_N are measured in days from January 1st. Such a choice entails that the south-to-north trajectory of the sunshade is the north-to-south trajectory, yet flown backwards.

A Differential Evolution (DE) algorithm was selected to solve each of the three optimization problems [62]. In all cases, a population of 20 individuals was initialized randomly, which evolved over 20 generations. Given the computational resources required to run the GREB model for 50 years, this setup results in roughly 66 hours of runtime to solve each optimization problem using a single seed to initialize the population. To solve the optimization problems, the open-source, Python-based heuristic optimization package `PyGMO` was used in this paper [63]. The results are presented and discussed in Sec. IX.

IX. Results and discussion

In this section, the results are presented and discussed. In Sec. IX.A, the performance of a static shade is analyzed. Then, the design space for a dynamic shade is explored through grid searches in Sec. IX.B. Finally, the optimal solutions found for each objective function are presented in Sec. IX.C.

A. Static shade

In Sec. III, it was stated that a static sunshade has the disadvantage of undercooling polar regions and overcooling tropical regions. This scenario is reproduced here by modeling a static sunshade with its location and size equal to the values reported in Table 1. The results of a 50-year simulation with the GREB model accounting for the effect of the static sunshade are reported in Fig. 13. It is possible to notice negative temperature anomalies, with peaks of $-0.4\,°C$ between the $+20°$ and $-20°$ latitudinal bands; on the other hand, temperature anomalies over the polar regions are evidently positive. These results confirm the findings reported in literature.

Furthermore, there is a clear latitudinal asymmetry: over Antarctica, temperature anomalies are lower than $1.0\,°C$ everywhere; on the other hand, in the northern hemisphere, the same level of anomaly is already reached in the latitudinal band between $+50°$ and $+80°$. At latitudes higher than $+80°$, the temperature anomaly is always greater than $1.0\,°C$, with peaks of $1.4\,°C$ over North-East Asia. The gradient in temperature anomalies is larger at mid-latitudes between $45°$ and $70°$ in both hemispheres. Such an asymmetry is likely due to the different split between land and oceans: in the southern hemisphere, the ratio between land and ocean is 1 to 4, which reduced to 1 to 1.5 in the northern hemisphere [64]. In other words, the fraction of land over the total area is 20% for the southern hemisphere and 40% for the northern hemisphere. As a result, given that water has a greater heat storage capacity than land, an equal increase in radiative forcing results in a lower average surface temperature in the southern hemisphere. This pattern is even more visible if the sunshade is not present (see Fig. 1). Therefore, it is expected that the outcome of the optimization problem will reflect this difference. In terms of sunshade trajectory, this roughly means that the sunshade should spend more time over the northern hemisphere.

From a global perspective, the reference scenario (CO_2 content of 340 ppm, corresponding to pre-industrial levels, without sunshade) results in a GMST of $\bar{T}_{\text{ref}}^{\text{global}} = 13.92\ °C$; on the other hand, the geoengineered scenario with a static sunshade produces a GMST of $\bar{T}_{\text{geo}}^{\text{global}} = 14.15\ °C$, simulated with GREB. This yields a global temperature anomaly of $J_{\text{GMST}} = 0.23\ °C$. As explained in Sec. IV, the size and location of the sunshade are assumed from literature so that an average reduction of 1.7% in insolation is achieved. It is clear that, under the assumptions made in this work, a slightly larger reduction in insolation would be required to completely offset the global temperature anomaly, which could be achieved by a larger sunshade. As long as the assumptions made to model the sunshade do not change, the fact that the GMST anomaly is not exactly zero is not an issue for this work, since the goal is to compare different trajectory solutions and understand their effects on the climate, rather than to accurately size the sunshade.

B. Grid search

Before solving the overarching optimization problem with the heuristic algorithm (see Fig. 2), the design space is explored by means of grid searches. The goal of using a grid search method is to better understand the search space and the impact of each variable of the decision vector $\mathbf{X}_2$, defined in Eq. 42. In particular, a regular grid of points is used for both types of independent variables (z-displacement and time of departure). The z-displacement is discretized through

ten equidistant points as follows:

$$z_S^* = \frac{z}{R_\oplus} = -\frac{i}{10} \qquad \text{for } i = 1, 2, \ldots, 10 \tag{43}$$

$$z_N^* = \frac{z}{R_\oplus} = +\frac{i}{10} \qquad \text{for } i = 1, 2, \ldots, 10 \tag{44}$$

where for simplicity the z-displacement is expressed as a fraction of the Earth's radius, $R_\oplus$. This notation will be used throughout the remainder of the paper. The start dates of the transfers (t_S and t_N) are also discretized with ten equidistant points as follows:

$$t_S = 30 + 10\,i \qquad \text{for } i = 1, 2, \ldots, 10 \tag{45}$$

$$t_N = 210 + 10\,i \qquad \text{for } i = 1, 2, \ldots, 10 \tag{46}$$

where t_S and t_N are measured in days from January 1st.

Two different types of grid searches are carried out. The first grid search fixes the start dates of the transfers ($t_S = 60$ days, $t_N = 240$ days) to create a catalog of trajectories with different combinations of z-displacement
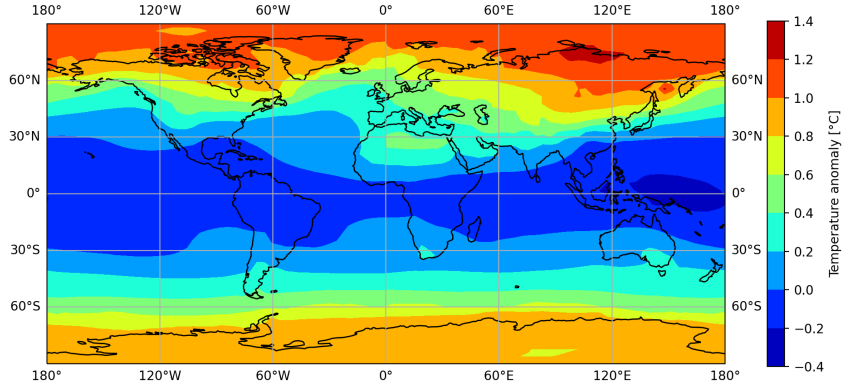
Fig. 13   Surface temperature anomaly resulting from the presence of a static sunshade.
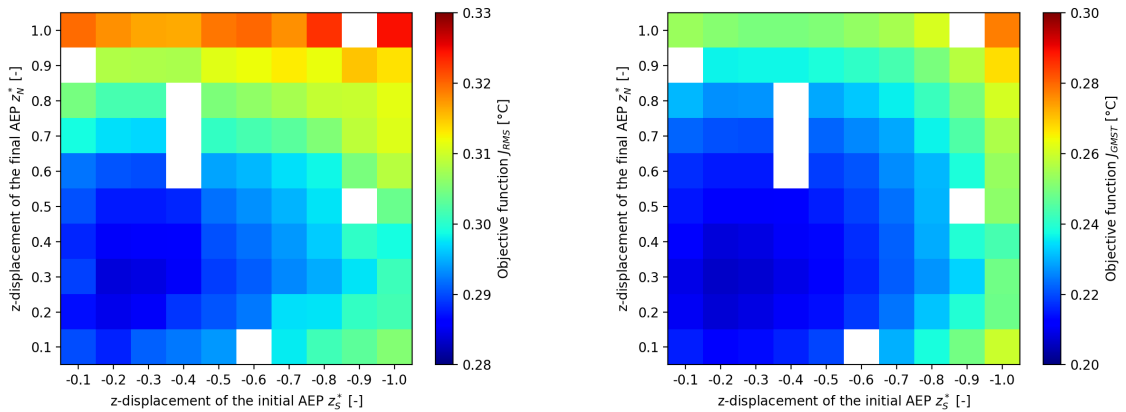
Fig. 14   Results of the grid search over the trajectory catalog for different combinations of z-displacement (z_S^* and z_N^*), with fixed departing dates of the transfers ($t_S = 60$ days, $t_N = 240$ days), performed for objective function J_{RMS} (left panel) and objective function J_{GMST} (right panel). White cells represent unfeasible transfer trajectories.
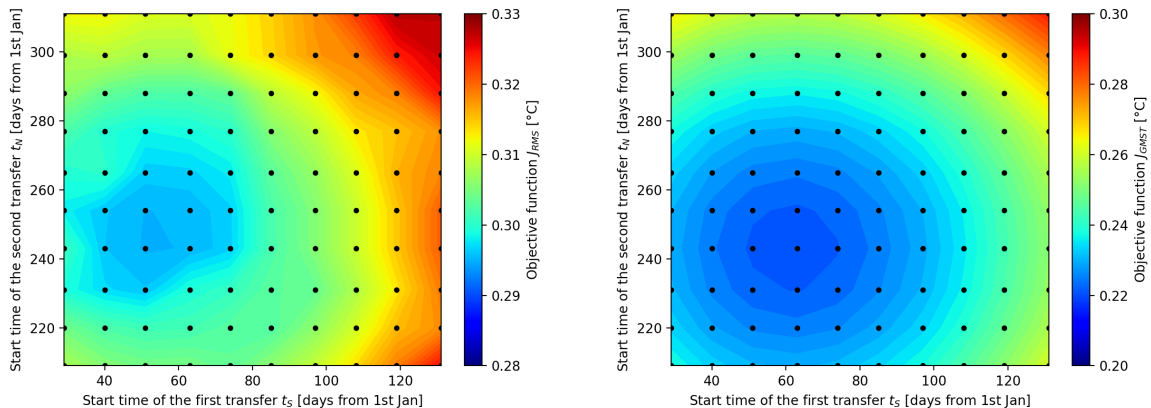
Fig. 15 Results of the grid search over the trajectory catalog for different combinations of start dates of the transfer (t_S and t_N), with fixed z-displacements ($z_S^* = -0.6R_\oplus$, $z_N^* = +0.6R_\oplus$), performed for objective function J_{RMS} (left panel) and objective function J_{GMST} (right panel). White cells represent unconverged transfer trajectories.

(z_S^* and z_N^*). A typical transfer trajectory resulting from the optimal control problem presented in Sec. VIII.A was already shown in Fig. 11. Instead, the second grid search fixes the initial and final z-displacement of the trajectory ($z_S^* = -0.6R_\oplus$, $z_N^* = 0.6R_\oplus$) while varying the dates when the sunshade departs from the AEPs. For each combination of z-displacement and departing dates, all the steps described in Fig. 2 are carried out: the time-optimal trajectory is found, the shading pattern is computed, and a climate simulation with the GREB model is performed, resulting in the evaluation of two metrics (the objective functions J_{RMS} and J_{GMST}). The objective function J_{polar} is not considered for the grid searches. The results are reported in Fig. 14 for the first grid search and in Fig. 15 for the second grid search.

Before analyzing the results, it should be mentioned that white cells in the figures correspond to unconverged transfers. Such trajectories are not unfeasible; on the contrary, it was verified that the optimizer is very sensitive to the number of collocation points. Therefore, the apparent unfeasibility could be solved using an iterative trial-and-error approach to a change in the number of collocation points.

Looking at Fig. 14, it can be noticed that the first type of grid search shows similar results for both objectives. The best-performing trajectories are found in the region described by $-0.3 \leqslant z_S^* \leqslant -0.2$ and $+0.2 \leqslant z_N^* \leqslant +0.3$, with the objective function gradually increasing for absolute displacement values larger than 0.3. It can also be noticed that the objective function J_{RMS} is slightly less sensitive to changes in the z-displacements with respect to objective J_{GMST}. Finally, Fig. 14 confirms again that a static shade with no vertical displacement is not the optimal solution to minimize temperature anomalies.

Observing the results from the second grid search, reported in Fig. 15, it is possible to see some differences between the two objective functions. For objective function J_{RMS}, the best performing region is found at $40 < t_S < 60$ days and $240 < t_N < 260$ days; for objective function J_{GMST}, which shows a more regular behavior with respect to J_{RMS}, the best performing region is located at roughly $50 < t_S < 70$ days and $230 < t_N < 250$ days. As a reference, the equinoxes occur around day 79 (March 20th) and day 266 (September 22nd). The transfer trajectory takes between 40 and 50 days to complete. If J_{RMS} is used as objective, the asymmetry mentioned in Sec. IX.A appears as expected. This pattern confirms that the sunshade should spend more time over the northern hemisphere and less over the southern hemisphere. It is interesting to notice that, when objective function J_{GMST} is used, the figure looks rather symmetric. This is because the GMST gives relatively more weight to equatorial regions than to polar regions; therefore, the motion of the sunshade closely follows the apparent oscillation of the Earth's spinning axis, giving less weight to temperature anomalies at higher latitudes. In addition, the best performing regions for J_{RMS} show that the values of t_S and t_N are more spread apart compared to the grid search for J_{GMST}, meaning that the sunshade spends more time over the northern hemisphere, as expected. Finally, objectives J_{RMS} and J_{GMST} seem to be more sensitive to the z-displacement than to the departing dates, as it can be seen from the range of the colorbar in the contour plots in Fig. 14 and Fig. 15.

The two grid searches described above allow to restrict the search space for the heuristic optimization process. The new boundaries of the search space that will be used to solve the optimization problems are reported in Table 3.

22

Table 3 Boundaries of the search space for the single-objective optimization problem (GMST).

Variable	Lower boundary	Upper boundary	Unit
z_S^*	-0.5	0.0	–
z_N^*	0.0	0.5	–
t_S	30	70	days from January 1st
t_N	230	270	days from January 1st

C. Optimization of the sunshade's motion

The results of the single-objective optimization problems are presented in the following subsections: Sec. IX.C.1 when optimizing for J_{RMS}, Sec. IX.C.2 when optimizing for J_{GMST}, and Sec. IX.C.3 when optimizing for J_{polar}. It is noted again that, for all optimization problems, the search space is limited to the values reported in Table 3. The results reported in this section are obtained by initializing the population with a seed value equal to 20151017.

1. Root Mean Squares (J_{RMS})

Objective function J_{RMS} highlights the latitudinal differences in the surface temperature anomalies. The evolution of the fitness of the best individual ("champion") of the population is reported in Fig. 17, while the independent variables corresponding to the optimal solution are reported in Table 4. The value of the objective at the last evolution is $J_{\mathrm{RMS}} = 0.2837\,^\circ\mathrm{C}$ and the resulting temperature anomaly distribution is very similar to the one shown in Fig. 16. It can be noticed that the optimizer struggles to significantly improve the value of the objective function.

More generally, comparing the results of this subsection with the ones presented in Sec. IX.C.2 suggests that the chosen metrics have a relatively low sensitivity with respect to the selected independent variables. This is mainly caused by the fact that the shade cast on the Earth does not change significantly, coupled with the inherent complexity of the Earth's climate system and the non-linearity of the problem. An extensive comparison of the optimization results and of other climate scenarios presented in the paper (reference scenario, without a shade, and with a static shade) is summarized in Table 4.

2. Global Mean Surface Temperature (J_{GMST})

The objective function used in this section is J_{GMST}, therefore the optimal trajectory in terms of GMST is searched for. This objective function is inherently a global metric. The evolution of the fitness of the best individual ("champion") of the population is reported in Fig. 17, while the independent variables corresponding to the optimal solution are reported in Table 4. The value of the objective at the last evolution is $J_{\mathrm{GMST}} = 0.2061\,^\circ\mathrm{C}$.

It can be noticed that the optimal solution obtained when optimizing for J_{RMS} and the optimal solution obtained when optimizing for J_{GMST} produce comparable values of the RMS. The possible causes of this have been already mentioned in the previous paragraphs. However, the independent variables reported in Table 4, in particular the values of the vertical displacement, z_S^* and z_N^*, indicate that the sunshade tends to shade the tropical regions less. Indeed, the vertical displacement is greater when optimizing for J_{RMS}, as the optimizer focuses on minimizing latitudinal temperature anomalies (i.e., casting more shade on the poles), rather than on a global metric (GMST). In addition, When computing the value for J_{GMST} for the trajectory obtained when optimizing for J_{RMS}, it can be noticed how the value of J_{GMST} is slightly higher with respect to the optimal value computed when optimizing for J_{GMST}. This can be explained with the fact that relatively less shade is cast on the equatorial regions that have the biggest influence on the objective function J_{GMST}.

Furthermore, the improvement of the objective function, J_{GMST}, across 20 generations is relatively small. This is due to a number of factors: firstly, the search space was already constrained based on the findings of the grid search explained in the previous subsection; secondly, the optimization settings (population size and number of generations) are severely limited by the runtime. In addition, given the entity of the results obtained, one could wonder whether it is worth changing the location of the sunshade, in terms of operational costs and complexity. However, this is beyond the scope of this work.
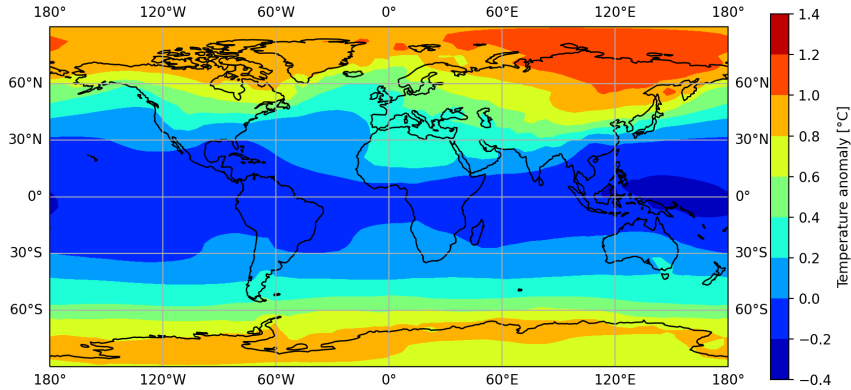
Fig. 16 Surface temperature anomaly resulting from the presence of a dynamic sunshade.

3. Polar Mean Surface Temperature (J_{polar})

The objective function J_{polar} forces the optimizer to focus on polar regions only. The evolution of the fitness of the best individual ("champion") of the population is reported in Fig. 17, while the independent variables corresponding to the optimal solution are reported in Table 4. The value of the objective at the last evolution is $J_{\text{polar}} = 0.9010\,^\circ\text{C}$ and the resulting temperature anomaly distribution is very similar to the one shown in Fig. 16. As a reference, the temperature anomaly of a static shade over the polar regions is $J_{\text{polar}}^{\text{static}} = 0.96\,^\circ\text{C}$. Therefore, this is another improvement with respect to the static shade. In addition, it can be observed that the reduction in polar temperature anomaly is two orders of magnitude greater than in global temperature anomaly. Again, as stated in Sec. IX.C.1, the values of the objectives do not differ significantly, but it can be noticed how the vertical displacement of the shade is higher than when optimizing for J_{RMS} and J_{GMST}. This was expected, as the objective function is solely focused on the surface temperature anomaly in the polar regions. It is interesting to notice how the vertical displacement, although greater than in the other cases, is limited to roughly $|z| < 0.32\,R_\oplus$, while larger values could have been predicted. This can be explained by two effects. Firstly, modeling solar radiation with limb darkening means that the center of the Sun should be shaded more than its limbs. Without solar limb darkening, the shade would be placed closer to the line connecting the Earth's pole to the center of the Sun. Secondly, it must be reminded that solar radiation is not the only source of climate forcing; internal energy exchanges through oceans and the atmosphere play a role as well, as explained in Sec. VII. Therefore, in order to minimize the surface temperature anomaly in a given region, casting a shade only on that area is not sufficient, as other regions would have a greater surface temperature, which would warm the target region by atmospheric energy transport (advection and diffusion). Although this explanation is greatly simplified, this result is another proof of the complexity of the climate system and of the non-linearity of the problem tackled in this paper.

4. Comparison

In Fig. 18 the vertical displacements of the optimal trajectories found in Sec. IX.C.2 through Sec. IX.C.3 are reported. All the features previously explained can be noticed: the vertical displacement is minimum when optimizing for J_{GMST}, increases for J_{RMS}, and is maximum for J_{polar}. Similarly, the cumulative transfer time decreases in the same order (J_{GMST}, J_{RMS}, and J_{polar}). This means, as expected, that the optimal trajectory found for J_{polar} spends more time at the equilibrium points to shade the polar regions, while the opposite is true for J_{GMST}. This is however not true for the second transfer, where the solution for J_{RMS} actually stays at the equilibrium point for longer. The reason for this was not exactly understood, but it may be simply caused by the optimization settings.

In addition, Fig. 18 shows another relevant feature that was already observed in Sec. IX.B. For the first transfer (from below to above the ecliptic plane), the sunshade crosses the ecliptic plane almost exactly at the equinox (dashed vertical line in the figure). However, for the second transfer, this is not the case: it can be noticed that the sunshade spends more time above the northern hemisphere, therefore the crossing of the ecliptic plane is delayed and happens only after the equinox (between 5 and 10 days later). This feature confirms the findings observed in Fig. 15, further clarifying the fact that the northern hemisphere should be shaded more than the southern hemisphere. The reason for
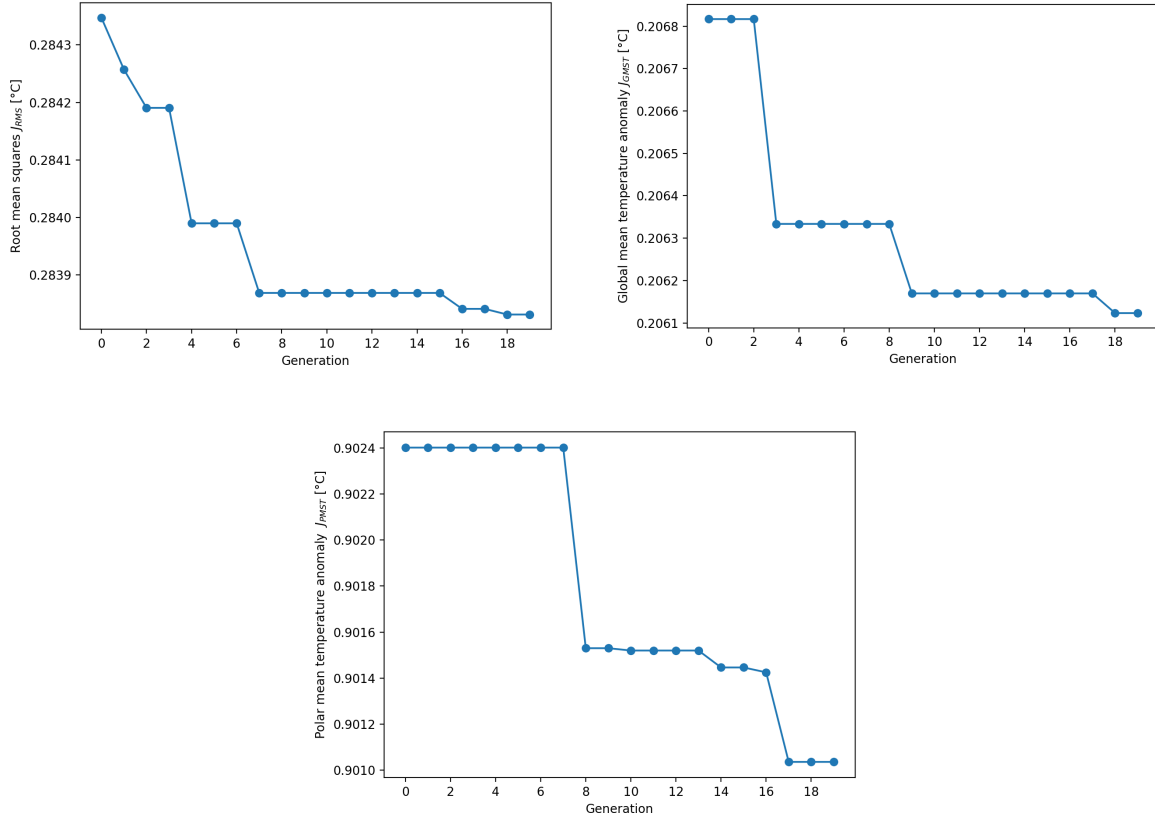
24

Fig. 17 Evolution of the best individual in the population when optimizing for J_{RMS} (top left panel), J_{GMST} (top right panel), and J_{PMST} (bottom panel).

this is related to the ocean/land ratio and was already explained in Sec. IX.B.

X. Conclusions

In this paper, the optimal trajectory of a planetary sunshade placed in the vicinity of the Sun-Earth displaced L_1 point was investigated to minimize regional imbalances observed for a static shade at the displaced L_1 point. The sunshade was modeled as an ideal solar sail in the dynamical framework of the Circular Restricted Three-Body Problem. A simplified climate model, GREB [36], was employed to evaluate the climatic evolution under different shading conditions. The Global Mean Surface Temperature (GMST) of the reference scenario (pre-industrial levels of atmospheric CO_2, equal to 340 ppm, without the sunshade) found is $\bar{T}_{\text{ref}}^{\text{global}} = 13.92$ °C. With an increased amount of atmospheric CO_2 (680 ppm), the resulting GMST is $\bar{T}_{2xCO2}^{\text{global}} = 16.39$ °C. It was found that a static shade with a fixed radius of 1434 km placed at a displaced equilibrium point on the ecliptic plane at a distance of $2.44 \cdot 10^6$ km from the Earth can reduce the GMST to $\bar{T}_{\text{geo}}^{\text{global}} = 14.15$ °C. While a dynamic shade improves the GMST by only 0.02 °C to $\bar{T}_{\text{geo}}^{\text{global}} = 14.13$ °C, it reduces the Polar Mean Surface Temperature (PMST) by 0.06 °C. In addition, a dynamic shade delivers an improvement in latitudinal imbalances compared to a static shade – quantified through the Root Mean Squares (RMS) of the latitudinal temperature anomaly distribution – from 0.3032 °C to 0.2837 °C, representing a 6.4% improvement. The most promising trajectory solutions move periodically between Artificial Equilibrium Points (AEPs) located at roughly 0.3 Earth radii above and 0.3 Earth radii below the ecliptic plane, with a slightly larger vertical displacement above the ecliptic plane. The optimal starting dates of the transfers are close to $t_S = 56$ days and $t_N = 250$ days for the transfers (from below to above the ecliptic plane and vice versa, respectively). While the trajectory found when optimizing for the GMST anomaly is almost symmetric in time and space, the optimal trajectory to minimize the PMST anomaly moves between

25
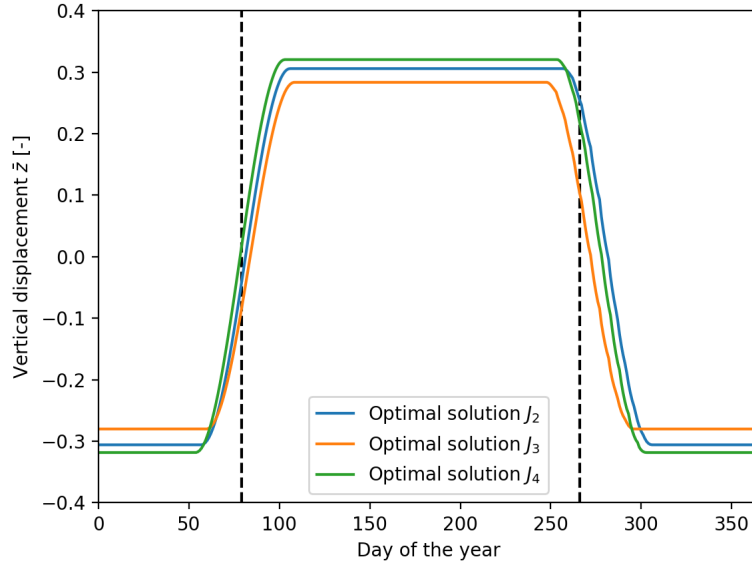
Fig. 18   Vertical displacement profile of the optimal solutions plotted against the day of the year.

AEPs displaced further above and below the ecliptic plane and remains there longer. This way, more shade can be cast over the polar regions; this, however, comes at the cost of a slightly higher GMST anomaly, since less shade is cast over tropical regions. In addition, it was observed that the northern hemisphere is shaded more and for longer than the southern hemisphere. This result can be explained through the imbalance in the land-to-ocean ratio, which is greater in the northern hemisphere, coupled with the higher heat storage capacity of oceans with respect to the land.

The results found in this paper highlight the benefits of a dynamic shade over a static one. So far, this is one of the only two studies tackling the problem of a dynamic sunshade for geoengineering purposes, together with Reference [33]. This study also employs and validates a trajectory design approach that has never been considered before in the context of space-based geoengineering. Therefore, this work constitutes a unique contribution to the research body concerned with space-based solar geoengineering solutions and its effects on the Earth's climate.

Table 4   Summary of the results. Highlighted cells show the objective function for each optimization problem.

Case	z_S^*	z_N^*	t_S	t_N	$\bar{T}^{\text{global}}$ [$^\circ C$]	$\bar{T}^{\text{polar}}$ [$^\circ C$]	J_{RMS} [$^\circ C$]	J_{GMST} [$^\circ C$]	J_{polar} [$^\circ C$]
Reference	–	–	–	–	13.92	−18.42	–	–	–
No shade	–	–	–	–	16.39	−15.44	2.5049	2.4711	2.9795
Static shade	0	0	0	0	14.15	−17.46	0.3032	0.2318	0.9633
Optimal J_2	−0.3059	+0.3058	56.80	254.99	14.13	−17.52	0.2837	0.2062	0.9013
Optimal J_3	−0.2801	+0.2835	59.71	245.59	14.13	−17.52	0.2837	0.2061	0.9017
Optimal J_4	−0.31841	+0.32050	53.74	251.38	14.13	−17.52	0.2840	0.2067	0.9010

References

[1] IPCC, Mayer, L., and Pachauri, R. K. (eds.), *Climate change 2014: synthesis report*, Intergovernmental Panel on Climate Change, Geneva, Switzerland, 2015.

[2] "Geoengineering the climate : science, governance and uncertainty," Tech. rep., Royal Society, 2009.

[3] Keith, D. W., "Why Capture CO_2 from the Atmosphere?" *Science*, Vol. 325, No. 5948, 2009, pp. 1654–1655. https://doi.org/10.1126/science.1175680, URL https://www.science.org/doi/10.1126/science.1175680.

[4] Rasch, P. J., Tilmes, S., Turco, R. P., Robock, A., Oman, L., Chen, C.-C. J., Stenchikov, G. L., and Garcia, R. R., "An overview of geoengineering of climate using stratospheric sulphate aerosols," *Philosophical Transactions of the Royal Society A: Mathematical, Physical and Engineering Sciences*, Vol. 366, No. 1882, 2008, pp. 4007–4037. https://doi.org/10.1098/rsta.2008.0131, URL https://royalsocietypublishing.org/doi/10.1098/rsta.2008.0131.

[5] Lenton, T. M., Held, H., Kriegler, E., Hall, J. W., Lucht, W., Rahmstorf, S., and Schellnhuber, H. J., "Tipping elements in the Earth's climate system," *Proceedings of the National Academy of Sciences*, Vol. 105, No. 6, 2008, pp. 1786–1793. https://doi.org/10.1073/pnas.0705414105, URL https://pnas.org/doi/full/10.1073/pnas.0705414105.

[6] McInnes, C. R., "Minimum mass solar shield for terrestrial climate control," *JBIS - Journal of the British Interplanetary Society*, Vol. 55, No. 9-10, 2002.

[7] Baum, C. M., Low, S., and Sovacool, B. K., "Between the sun and us: Expert perceptions on the innovation, policy, and deep uncertainties of space-based solar geoengineering," *Renewable and Sustainable Energy Reviews*, Vol. 158, 2022, p. 112179. https://doi.org/10.1016/j.rser.2022.112179, URL https://linkinghub.elsevier.com/retrieve/pii/S1364032122001046.

[8] Govindasamy, B., and Caldeira, K., "Geoengineering Earth's radiation balance to mitigate CO2-induced climate change," *Geophysical Research Letters*, Vol. 27, No. 14, 2000, pp. 2141–2144. https://doi.org/10.1029/1999GL006086, publisher: American Geophysical Union.

[9] Govindasamy, B., Caldeira, K., and Duffy, P. B., "Geoengineering Earth's radiation balance to mitigate climate change from a quadrupling of CO2," *Global and Planetary Change*, Vol. 37, No. 1-2, 2003, pp. 157–168. https://doi.org/10.1016/S0921-8181(02)00195-9, publisher: Elsevier B.V.

[10] Robock, A., Oman, L., and Stenchikov, G. L., "Regional climate responses to geoengineering with tropical and Arctic SO2 injections," *Journal of Geophysical Research*, Vol. 113, No. D16, 2008, p. D16101. https://doi.org/10.1029/2008JD010050, URL http://doi.wiley.com/10.1029/2008JD010050.

[11] Ricke, K. L., Morgan, M. G., and Allen, M. R., "Regional climate response to solar-radiation management," *Nature Geoscience*, Vol. 3, No. 8, 2010, pp. 537–541. https://doi.org/10.1038/ngeo915, URL http://www.nature.com/articles/ngeo915.

[12] Caldeira, K., and Wood, L., "Global and Arctic climate engineering: numerical model studies," *Philosophical Transactions of the Royal Society A: Mathematical, Physical and Engineering Sciences*, Vol. 366, No. 1882, 2008, pp. 4039–4056. https://doi.org/10.1098/rsta.2008.0132, URL https://royalsocietypublishing.org/doi/10.1098/rsta.2008.0132.

[13] Govindasamy, B., Thompson, S., Duffy, P. B., Caldeira, K., and Delire, C., "Impact of geoengineering schemes on the terrestrial biosphere," *Geophysical Research Letters*, Vol. 29, No. 22, 2002, pp. 18–1–18–4. https://doi.org/10.1029/2002gl015911, publisher: American Geophysical Union.

[14] Bala, G., Duffy, P. B., and Taylor, K. E., "Impact of geoengineering schemes on the global hydrological cycle," *Proceedings of the National Academy of Sciences*, Vol. 105, No. 22, 2008, pp. 7664–7669. https://doi.org/10.1073/pnas.0711648105, URL http://www.pnas.org/cgi/doi/10.1073/pnas.0711648105.

[15] Matthews, H. D., Caldeira, K., and Karl, D. M., "Transient climate-carbon simulations of planetary geoengineering," *Proceedings of the National Academy of Sciences*, Vol. 104, No. 24, 2007, pp. 9949–9954. URL www.pnas.orgcgidoi10.1073pnas.0700419104.

[16] Moreno-Cruz, J. B., Ricke, K. L., and Keith, D. W., "A simple model to account for regional inequalities in the effectiveness of solar radiation management," *Climatic Change*, Vol. 110, No. 3-4, 2012, pp. 649–668. https://doi.org/10.1007/s10584-011-0103-z.

[17] Ban-Weiss, G. A., and Caldeira, K., "Geoengineering as an optimization problem," *Environmental Research Letters*, Vol. 5, No. 3, 2010. https://doi.org/10.1088/1748-9326/5/3/034009, publisher: Institute of Physics Publishing.

[18] MacMartin, D. G., Keith, D. W., Kravitz, B., and Caldeira, K., "Management of trade-offs in geoengineering through optimal choice of non-uniform radiative forcing," *Nature Climate Change*, Vol. 3, No. 4, 2013, pp. 365–368. https://doi.org/10.1038/nclimate1722.

[19] Early, J. T., "Space-based solar shield to offset greenhouse effect," *Journal of the British Interplanetary Society*, Vol. 42, 1989, pp. 567–569.

[20] Hudson, H., "A space parasol as a countermeasure against the greenhouse effect," *Journal of the British Interplanetary Society*, Vol. 44, 1991, p. 139.

[21] Mautner, M. N., "Deep-space solar screens against climatic warming: technical and research requirements," *Proceedings of the Third Pacific Basin International Symposium on Advances in Space Sciences Technology and its Applications (PISSTA)*, 1989. URL https://www.researchgate.net/publication/321712294.

[22] Mautner, M., "A space-based solar screen against climatic warming," *Journal of the British Interplanetary Society*, Vol. 44, No. 3, 1991.

[23] Pearson, J., Oldson, J., and Levin, E., "Earth rings for planetary environment control," *Acta Astronautica*, Vol. 58, No. 1, 2006. https://doi.org/10.1016/j.actaastro.2005.03.071.

[24] Struck, C., "The Feasibility of Shading the Greenhouse with Dust Clouds at the Stable Lunar Lagrange Points," *Journal of the British Interplanetary Society*, Vol. 60, 2007.

[25] Bewick, R., Sanchez, J. P., and McInnes, C. R., "The feasibility of using an L 1 positioned dust cloud as a method of space-based geoengineering," *Advances in Space Research*, Vol. 49, No. 7, 2012, pp. 1212–1228. https://doi.org/10.1016/j.asr.2012.01.010, publisher: Elsevier Ltd.

[26] Roy, K. I., "Solar sails: An answer to Global Warming?" *AIP Conference Proceedings*, Vol. 552, AIP, Albuquerque, New Mexico, 2001, pp. 413–418. https://doi.org/10.1063/1.1357956, URL http://aip.scitation.org/doi/abs/10.1063/1.1357956, iSSN: 0094243X.

[27] Angel, R., "Feasibility of cooling the Earth with a cloud of small spacecraft near the inner Langrange point (L1)," *Proceedings of the National Academy of Sciences of the United States of America*, Vol. 103, No. 46, 2006. https://doi.org/10.1073/pnas.0608163103.

[28] Biggs, J. D., and McInnes, C. R., "Passive Orbit Control for Space-Based Geo-eEngineering," *Journal of Guidance, Control, and Dynamics*, Vol. 33, No. 3, 2010, pp. 1017–1020. https://doi.org/10.2514/1.46054, URL https://arc.aiaa.org/doi/10.2514/1.46054.

[29] Seeley, J. T., Lutsko, N. J., and Keith, D. W., "Designing a Radiative Antidote to CO2," *Geophysical Research Letters*, Vol. 48, No. 1, 2021. https://doi.org/10.1029/2020GL090876, URL https://onlinelibrary.wiley.com/doi/10.1029/2020GL090876.

[30] Fuglesang, C., and de Herreros Miciano, M. G., "Realistic sunshade system at L1 for global temperature control," *Acta Astronautica*, Vol. 186, 2021, pp. 269–279. https://doi.org/10.1016/j.actaastro.2021.04.035, URL https://linkinghub.elsevier.com/retrieve/pii/S0094576521001995.

[31] Kosugi, T., "Role of sunshades in space as a climate control option," *Acta Astronautica*, Vol. 67, No. 1-2, 2010, pp. 241–253. https://doi.org/10.1016/j.actaastro.2010.02.009.

[32] Lunt, D. J., Ridgwell, A., Valdes, P. J., and Seale, A., ""Sunshade World": A fully coupled GCM evaluation of the climatic impacts of geoengineering," *Geophysical Research Letters*, Vol. 35, No. 12, 2008. https://doi.org/10.1029/2008GL033674, publisher: American Geophysical Union.

[33] Sánchez, J.-P., and McInnes, C. R., "Optimal Sunshade Configurations for Space-Based Geoengineering near the Sun-Earth L1 Point," *PLOS ONE*, Vol. 10, No. 8, 2015, p. e0136648. https://doi.org/10.1371/journal.pone.0136648, URL https://dx.plos.org/10.1371/journal.pone.0136648.

[34] McInnes, C. R., McDonald, A. J. C., Simmons, J. F. L., and MacDonald, E. W., "Solar sail parking in restricted three-body systems," *Journal of Guidance, Control, and Dynamics*, Vol. 17, No. 2, 1994, pp. 399–406. https://doi.org/10.2514/3.21211, URL https://arc.aiaa.org/doi/10.2514/3.21211.

[35] McInnes, C. R., *Solar sailing: technology, dynamics and mission applications*, Springer-Praxis series in space science and technology, Springer [u.a.], London, 1999. OCLC: 246336919.

[36] Dommenget, D., and Flöter, J., "Conceptual understanding of climate change with a globally resolved energy balance model," *Climate Dynamics*, Vol. 37, No. 11-12, 2011, pp. 2143–2165. https://doi.org/10.1007/s00382-011-1026-0, URL http://link.springer.com/10.1007/s00382-011-1026-0.

[37] Heiligers, J. M., and McInnes, C. R., "Agile solar sailing in three-body problem: Motion between artificial equilibrium points," International Astronautical Federation, Beijing, China, 2013.

[38] Lissauer, J. J., and De Pater, I., *Fundamental Planetary Science*, Cambridge University Press, USA, 2013.

[39] Szebehely, V. G., *Theory of orbits: the restricted problem of three bodies*, Academic Press, 1967.

[40] Heiligers, J., Vergaaij, M., and Ceriotti, M., "End-to-end trajectory design for a solar-sail-only pole-sitter at Venus, Earth, and Mars," *Advances in Space Research*, Vol. 67, No. 9, 2021, pp. 2995–3011. https://doi.org/10.1016/j.asr.2020.06.011, URL https://linkinghub.elsevier.com/retrieve/pii/S0273117720304130.

[41] Nicodemus, F. E., "Radiance," *American Journal of Physics*, Vol. 31, No. 5, 1963, pp. 368–377. https://doi.org/10.1119/1.1969512, URL http://aapt.scitation.org/doi/10.1119/1.1969512.

[42] Kopp, G., and Lean, J. L., "A new, lower value of total solar irradiance: Evidence and climate significance: FRONTIER," *Geophysical Research Letters*, Vol. 38, No. 1, 2011, pp. n/a–n/a. https://doi.org/10.1029/2010GL045777, URL http://doi.wiley.com/10.1029/2010GL045777.

[43] Hartmann, D. L., *Global physical climatology*, No. v. 56 in International geophysics, Academic Press, San Diego, 1994.

[44] Vasquez Padilla, Ricardo, "Simplified Methodology for Designing Parabolic Trough Solar Power Plants," Ph.D. thesis, USF Tampa, Tampa, Florida, 2011. URL https://digitalcommons.usf.edu/etd/3390.

[45] Escobal, P. R., and Robertson, R. A., "Lunar eclipse of a satellite of the earth." *Journal of Spacecraft and Rockets*, Vol. 4, No. 4, 1967, pp. 538–540. https://doi.org/10.2514/3.28903, URL https://arc.aiaa.org/doi/10.2514/3.28903.

[46] Vallado, D. A., and McClain, W. D., *Fundamentals of astrodynamics and applications*, 4th ed., No. 21 in Space technology library, Microcosm Press, Hawthorne, Calif, 2013.

[47] Wertz, J. R., *Mission geometry: orbit and constellation design and management ; spacecraft orbit and attitude systems*, No. 13 in Space technology library, Microcosm Press, El Segundo, Calif, 2001.

[48] Pierce, A., and Slaughter, C., "Solar limb darkening," *Solar Physics*, Vol. 51, No. 1, 1977. https://doi.org/10.1007/BF00240442, URL http://link.springer.com/10.1007/BF00240442.

[49] Neckel, H., and Labs, D., "Solar limb darkening 1986–1990 (303 to 1099 nm)," *Solar Physics*, Vol. 153, No. 1-2, 1994, pp. 91–114. https://doi.org/10.1007/BF00712494, URL http://link.springer.com/10.1007/BF00712494.

[50] Cox, A. N., and Cox, A. N., *Allen's Astrophysical Quantities*, 2002. URL https://link.springer.com/book/10.1007/978-1-4612-7037-9, oCLC: 1058941068.

[51] Budyko, M. I., "The effect of solar radiation variations on the climate of the Earth," *Tellus*, Vol. 21, No. 5, 1969, pp. 611–619. https://doi.org/10.1111/j.2153-3490.1969.tb00466.x, URL http://tellusa.net/index.php/tellusa/article/view/10109.

[52] Sellers, W. D., "A global climatic model based on the energy balance of the Earth-Atmosphere system," *Journal of Applied Meteorology*, Vol. 8, 1969, pp. 392–400.

[53] Petoukhov, V., Claussen, M., Berger, A., Crucifix, M., Eby, M., Eliseev, A. V., Fichefet, T., Ganopolski, A., Goosse, H., Kamenkovich, I., Mokhov, I. I., Montoya, M., Mysak, L. A., Sokolov, A., Stone, P., Wang, Z., and Weaver, A. J., "EMIC Intercomparison Project (EMIP–CO2): comparative analysis of EMIC simulations of climate, and of equilibrium and transient responses to atmospheric CO2 doubling," *Climate Dynamics*, Vol. 25, No. 4, 2005, pp. 363–385. https://doi.org/10.1007/s00382-005-0042-3, URL http://link.springer.com/10.1007/s00382-005-0042-3.

[54] Meehl, G. A., Covey, C., Delworth, T., Latif, M., McAvaney, B., Mitchell, J. F. B., Stouffer, R. J., and Taylor, K. E., "THE WCRP CMIP3 Multimodel Dataset: A New Era in Climate Change Research," *Bulletin of the American Meteorological Society*, Vol. 88, No. 9, 2007, pp. 1383–1394. https://doi.org/10.1175/BAMS-88-9-1383, URL https://journals.ametsoc.org/doi/10.1175/BAMS-88-9-1383.

[55] Nicholls, Z. R. J., Meinshausen, M., Lewis, J., Gieseke, R., Dommenget, D., Dorheim, K., Fan, C.-S., Fuglestvedt, J. S., Gasser, T., Golüke, U., Goodwin, P., Hartin, C., Hope, A. P., Kriegler, E., Leach, N. J., Marchegiani, D., McBride, L. A., Quilcaille, Y., Rogelj, J., Salawitch, R. J., Samset, B. H., Sandstad, M., Shiklomanov, A. N., Skeie, R. B., Smith, C. J., Smith, S., Tanaka, K., Tsutsui, J., and Xie, Z., "Reduced Complexity Model Intercomparison Project Phase 1: introduction and evaluation of global-mean temperature response," *Geoscientific Model Development*, Vol. 13, No. 11, 2020, pp. 5175–5190. https://doi.org/10.5194/gmd-13-5175-2020, URL https://gmd.copernicus.org/articles/13/5175/2020/.

[56] Betts, J. T., "Survey of numerical methods for trajectory optimization," *Journal of guidance, control, and dynamics*, Vol. 21, No. 2, 1998, pp. 193–207.

[57] Betts, J. T., *Practical methods for optimal control using nonlinear programming*, Advances in design and control, Society for Industrial and Applied Mathematics, Philadelphia, PA, 2001.

[58] Biegler, L. T., *Nonlinear programming: concepts, algorithms, and applications to chemical processes*, MOS-SIAM series on optimization, Society for Industrial and Applied Mathematics : Mathematical Programming Society, Philadelphia, 2010.

[59] Bynum, M. L., Hackebeil, G. A., Hart, W. E., Laird, C. D., Nicholson, B. L., Siirola, J. D., Watson, J.-P., and Woodruff, D. L., *Pyomo — Optimization Modeling in Python*, Springer Optimization and Its Applications, Vol. 67, Springer International Publishing, Cham, 2021. https://doi.org/10.1007/978-3-030-68928-5, URL http://link.springer.com/10.1007/978-3-030-68928-5.

[60] Wächter, A., and Biegler, L. T., "On the implementation of an interior-point filter line-search algorithm for large-scale nonlinear programming," *Mathematical Programming*, Vol. 106, No. 1, 2006, pp. 25–57. https://doi.org/10.1007/s10107-004-0559-y, URL http://link.springer.com/10.1007/s10107-004-0559-y.

[61] Hausfather, Z., Cowtan, K., Menne, M. J., and Williams, C. N., "Evaluating the impact of U.S. Historical Climatology Network homogenization using the U.S. Climate Reference Network," *Geophysical Research Letters*, Vol. 43, No. 4, 2016, pp. 1695–1701. https://doi.org/10.1002/2015GL067640, URL https://onlinelibrary.wiley.com/doi/10.1002/2015GL067640.

[62] Storn, R., and Price, K., "Differential Evolution – A Simple and Efficient Heuristic for global Optimization over Continuous Spaces," *Journal of Global Optimization*, Vol. 11, No. 4, 1997, pp. 341–359. https://doi.org/10.1023/A:1008202821328, URL http://link.springer.com/10.1023/A:1008202821328.

[63] Biscani, F., and Izzo, D., "A parallel global multiobjective framework for optimization: pagmo," *Journal of Open Source Software*, Vol. 5, No. 53, 2020, p. 2338.

[64] Marshall, J., and Plumb, R. A., *Atmosphere, ocean, and climate dynamics: an introductory text*, No. v. 93 in International geophysics series, Elsevier Academic Press, Amsterdam ; [Burlington, MA], 2008. OCLC: ocn166317541.

3

Conclusions and Recommendations

In this chapter, answers to the research questions presented in Chapter 1 are provided and conclusions are drawn. Furthermore, recommendations for future research on the trajectory optimization of a planetary sunshade are outlined.

3.1. Conclusions

In this section, each research question presented in Chapter 1 will be answered separately.

1. *Is it possible to couple the out-of-plane motion of a planetary sunshade with the Earth's seasonal cycle to offset global warming, solely relying on the solar radiation pressure acceleration?*

   The work carried out for this thesis proved that coupling the out-of-plane motion of a planetary sunshade with the Earth's seasonal cycle is indeed possible. In particular, the motion of the sunshade was controlled through the solar radiation pressure acceleration. In literature, it is reported that a static sunshade placed at the solar sail-displaced L_1 point overcools tropical regions and undercools polar regions. Therefore, this suggests that polar regions should be shaded more than tropical regions. Hence, the trajectory strategy adopted in this paper includes exploiting both Artificial Equilibrium Points (AEPs) above and below the ecliptic plane, where the shade is parked, and a time-optimal transfer optimization between these AEPs.

   To investigate the problem, the following methodology was adopted: the sunshade is parked at an Artificial Equilibrium Point (AEP) below the ecliptic plane during the northern hemisphere's winter. It is then transferred to another AEP above the ecliptic plane via a time-optimal transfer trajectory to remain there during summer of the northern hemisphere. After approximately six months, the shade transfers back towards the AEP below the ecliptic plane and the process is repeated over the years. The vertical displacements above and below the ecliptic plane, together with the start date of the transfer trajectories, were selected as the optimization variables of the problem. The dynamical framework used to model the sunshade's trajectory was the Circular Restricted Three-Body Problem (CR3BP) with the addition of the solar radiation pressure (SRP) acceleration. The sunshade is modelled as an ideal sail and its motion is controlled by varying the sail's attitude. The artificial solar radiation distribution on Earth resulting from the presence of the sunshade is computed using a solar limb darkening model to account for higher brightness at the center of the solar disk and lower brightness at its limbs. The resulting insolation profile, directly related to the sunshade's trajectory, is evaluated through a simplified climate model. The surface temperature distribution at the 50th year of a climate simulation is compared to a reference scenario, corresponding to the climate system without sunshade and with a pre-industrial atmospheric CO_2 concentration (340 ppm). The climate scenarios considered in this work are reported in Table 3.1. A genetic algorithm is used to find the optimal trajectories with respect to three different objectives, denoted with $J_\square$: the Global Mean Surface Temperature (GMST) anomaly (where the anomaly is defined as the difference between a given scenario and the reference scenario to evaluate the global impact of the sunshade; the Root of the Mean of the Squares (RMS) of the latitudinal distribution of the temperature anomaly, quantifying latitudinal imbalances between tropical and

Case	Name	Notation	CO_2 [ppm]	Sunshade
A	Reference	$\square_{\text{ref}}$	340	Absent
B	2xCO2	$\square_{\text{2xCO2}}$	680	Absent
C	Geoengineering - static	$\square_{\text{geo}}^{\text{static}}$	680	Static
D	Geoengineering - dynamic	$\square_{\text{geo}}^{\text{dynamic}}$	680	Dynamic

Table 3.1 — Climate scenarios considered.

polar regions; the Polar Mean Surface Temperature (PMST) anomaly, where only regions above $65°$ latitude are accounted for.

The results are summarized in Table 3.2. It was found that a moving sunshade improves the Global Mean Surface Temperature (GMST) with respect to a static shade, although not significantly, but it can especially reduce latitudinal surface temperature imbalances. In particular, the simulations conducted in this work compared a climate scenario with an atmospheric CO_2 content of 680 ppm (case D) corrected by the sunshade to the reference scenario, characterized by a GMST of 13.92 °C (case A). A dynamic shade with a radius of 1434 km placed at a distance of $2.44 \cdot 10^6$ km from the Earth can reduce the GMST from 16.39 °C (case B) to 14.12 ° (case D), resulting in a reduction of more than 2°C and an increase of less than a quarter of degree with respect to the reference scenario. The improvement in latitudinal imbalances ensured by a moving sunshade corresponds to an RMS of 0.28 °C (case D with respect to case A), representing a 6.4% improvement from the 0.30 °C value for a static shade (case B with respect to case A). In addition, the Polar Mean Surface Temperature (PMST, corresponding to the GMST computed for high latitudes) can be improved by 0.06 °C with respect to a static shade (case D with respect to case A), corresponding to a 6.6% improvement.

2. *Is the combination of parking locations and time-optimal transfer trajectories an effective mission design strategy for a planetary sunshade?*

The findings presented in this report suggest that this strategy is effective. In particular, the performance mentioned above was achieved with a vertical displacement of the shade of 30% the value of the Earth's radius, with the optimal starting dates of the transfers being 56 days for the first transfer (from below to above the ecliptic plane) and 250 days for the second transfer (from above to below the ecliptic plane), both measured from 1$^{\text{st}}$ January. Furthermore, this trajectory strategy has revealed additional findings. In the first place, larger vertical displacements and longer periods spent at the AEPs are needed to achieve a smaller PMST with respect to the GMST. This is a logical finding, as it effectively means that more shade is cast over polar regions and less over tropical regions. Furthermore, a hemispheric difference was observed: the northern hemisphere, with a greater land-to-ocean ratio, must be shaded more than the southern hemisphere. Indeed, in the southern hemisphere the higher fraction of oceans allows for more insolation to be absorbed while registering the same surface temperature increase with respect to the northern hemisphere.

Case	z_S^*	z_N^*	t_S	t_N	$\overline{T}^{\text{global}}$	$\overline{T}^{\text{polar}}$	J_{RMS}	J_{GMST}	J_{PMST}
Reference	–	–	–	–	13.92	−18.42	–	–	–
No shade	–	–	–	–	16.39	−15.44	2.5049	2.4711	2.9795
Static shade	0	0	0	0	14.15	−17.46	0.3032	0.2318	0.9633
Optimal J_2	−0.3059	+0.3058	56.80	254.99	14.13	−17.52	0.2837	0.2062	0.9013
Optimal J_3	−0.2801	+0.2835	59.71	245.59	14.13	−17.52	0.2837	0.2061	0.9017
Optimal J_4	−0.31841	+0.32050	53.74	251.38	14.13	−17.52	0.2840	0.2067	0.9010

Table 3.2 — Summary of the results. Highlighted cells show the objective function for each optimization problem. All values are expressed in degrees Celsius, except for the first four columns, where the vertical displacements, z_S^* and z_N^*, are expressed as fractions of Earth radii, while the times of departure, t_S and t_N, are expressed in days from January 1$^{\text{st}}$.

3. *How does a genetic algorithm compare to a grid search with respect to finding the optimal trajectory solution of a planetary sunshade that minimizes temperature anomalies?*

   The grid search presented in the paper was useful to reveal the impact of the selected independent variables on the surface temperature and gain a rough understanding of the design space before starting the optimization process. A downside of the grid search method is the fact that only two independent variables were analyzed at a time; while it would have been possible to run a three- or four-dimensional grid search, representing the results and understanding the main patterns would have been challenging. Nevertheless, the grid search anticipated the main findings that were confirmed by the optimization process. On the other hand, the optimization problem was useful to refine the results of the grid search. While running an optimization problem for the topic treated in this work is not a bad choice *per se*, the optimization process carried out with the settings used in this report did not lead to significant improvements with respect to the results found through the grid search. Although it was noticed that relatively large changes of independent variables led to relatively small changes in the objective function, this is likely due to the limited size of the population and limited amount of evolutions used by the genetic algorithm, coupled with the non-linearity of the problem. It is expected that the methodology used in this work will deliver better results when the trajectories of *a swarm of* sunshades are optimized.

3.2. Recommendations for further research

In this section, a set of recommendations to carry out further research following this work are outlined.

3.2.1. Swarm of sunshades

From the results of this work, it is clear that tailoring the out-of-plane displacement of a single sunshade to offset residual climate changes can deliver some improvements with respect to a static shade. However, the results also prove that more degrees of freedom are needed to achieve a larger reduction of the residual climate changes in the Earth's climate. In particular, it is expected that having a swarm of smaller sunshades will be extremely beneficial to minimize regional anomalies. Indeed, a much finer control of the shade and its distribution can be achieved by having multiple shades. In reference [18], this approach was attempted with two sunshades; the results of this work suggest that increasing the number of shades by two or three orders of magnitude will deliver noticeable improvements. This approach is also much more feasible from the systems engineering point of view, as manufacturing and deploying smaller units will be easier, despite the increase in mass caused by the spacecraft bus, structure, and other non-shading mass. The approach followed by this paper can be utilized by future studies that consider a swarm of sunshades; in addition, the code base is constructed so that the extension to a swarm of sunshades can be achieved by small changes to the code interfaces. Finally, a system of multiple sunshades will allow to satisfy other climate requirements besides the surface temperature, such as those related to precipitations and the hydrological cycle. In reference [19], it was found that minimizing changes both in surface temperature and precipitation is not possible with a single sunshade; nevertheless, more complex systems made by hundreds or thousands of sunshades allow to overcome this limitation.

3.2.2. Higher-fidelity climate models

The climate model used in this work is the Globally Resolved Energy Balance (GREB) model [20]. While GREB is the only globally resolved energy balance model [21], its accuracy is limited. This is caused by the nature of the model itself, as some physical features are not reproduced, but are fixed and treated as boundary conditions. This comes at the advantage of less stringent requirements in terms of computational resources, which allow for much smaller runtime with respect to fully-coupled Global Circulation Models (GCMs). Therefore, the suitability of GREB as a fast tool to assess climate change is recognized. It was also proved by [20] that GREB's uncertainties lie within the uncertainty levels recommended by the International Panel on Climate Change for its model ensemble. Nevertheless, the low-fidelity and lack of representation of important physical processes are clear disadvantages of the GREB model. One recommendation for the scientific community focused on space-based geo-engineering is to verify the results obtained in this paper with more accurate climate models. While the trajectory optimization problem can continue to be solved through simple models such as GREB,

its results should be checked against GCMs to verify their reliability. In addition, since the analysis of regional rather than global climate changes will be more and more relevant in this field of research, it is recommended for future works to adopt more accurate climate models directly within the optimization loop. This can be done by selecting computationally efficient climate models (such as Earth Models of Intermediate Complexity) or by increasing the computational resources available for these studies.

3.2.3. More efficient insolation model

The insolation model implemented in this work is accurate but not computationally efficient. Its accuracy is derived by the fact that solar limb darkening is accounted for; in addition, the insolation reduction caused by the sunshade is evaluated on a grid of points accurately representing the Earth's surface, without further simplifying assumptions, as it was done in reference [18]. Nevertheless, the amount of mathematical operations needed to compute the reduced insolation has an impact on the runtime. Little attention has been given in this work to improve the computational efficiency of the algorithm, but in further research this aspect should be improved to reduce the overall runtime.

3.2.4. More extensive heuristic optimization

The heuristic optimization problem run in this work had major limitations in terms of runtime. The major impediment was the computational resources required by the GREB model (50 years of climate simulation computed in 10 minutes). While the computer implementation of the GREB model was improved as much as possible, a heuristic optimization problem with a population of 20 individuals evolved 20 times required a simulation time of 67 hours for GREB only. Since it was not possible to parallelize the computation due to a number of technical issues, the extensiveness of the heuristic optimization problem had to be severely limited. In further research, this aspect should be improved by parallelizing the computations or by running simulations on more powerful machines. The runtime issue could also be solved by computing a climate scenario for a set of regularly spaced vertical displacements of the sunshade to then combine them linearly. This approach, used for instance by [18], has the advantage of largely reducing the runtime requirements, yet it reduces the accuracy of the results.

References

[1] Spencer R. Weart. *The discovery of global warming*. Rev. and expanded ed. New histories of science, technology, and medicine. Cambridge, Mass: Harvard University Press, 2008. ISBN: 978-0-674-03189-0.

[2] Sebastian Oberthür and Hermann Ott. *The Kyoto Protocol: international climate policy for the 21st century*. New York: Springer, 1999. ISBN: 978-3-540-66470-3.

[3] Joeri Rogelj et al. "Paris Agreement climate proposals need a boost to keep warming well below 2 °C". en. In: *Nature* 534.7609 (June 2016), pp. 631–639. ISSN: 0028-0836, 1476-4687. DOI: 10.1038/nature18307. URL: http://www.nature.com/articles/nature18307 (visited on 05/19/2021).

[4] Timothy M. Lenton et al. "Climate tipping points — too risky to bet against". en. In: *Nature* 575.7784 (Nov. 2019), pp. 592–595. ISSN: 0028-0836, 1476-4687. DOI: 10.1038/d41586-019-03595-0. URL: http://www.nature.com/articles/d41586-019-03595-0 (visited on 05/19/2021).

[5] Royal Society. *Geoengineering the climate : science, governance and uncertainty*. Tech. rep. Royal Society, 2009.

[6] James T. Early. "Space-based solar shield to offset greenhouse effect". In: *Journal of the British Interplanetary Society* 42 (1989), pp. 567–569.

[7] Michael Noah Mautner. "Deep-space solar screens against climatic warming: technical and research requirements". In: *Proceedings of the Third Pacific Basin International Symposium on Advances in Space Sciences Technology and its Applications (PISSTA)*. 1989. URL: https://www.researchgate.net/publication/321712294.

[8] HS Hudson. "A space parasol as a countermeasure against the greenhouse effect". In: *Journal of the British Interplanetary Society* 44 (1991), p. 139.

[9] Kenneth I. Roy. "Solar sails: An answer to Global Warming?" en. In: *AIP Conference Proceedings*. Vol. 552. ISSN: 0094243X. Albuquerque, New Mexico: AIP, 2001, pp. 413–418. DOI: 10.1063/1.1357956. URL: http://aip.scitation.org/doi/abs/10.1063/1.1357956 (visited on 03/23/2021).

[10] C. R. McInnes. "Minimum mass solar shield for terrestrial climate control". In: *JBIS - Journal of the British Interplanetary Society* 55.9-10 (2002). ISSN: 0007084X.

[11] Roger Angel. "Feasibility of cooling the Earth with a cloud of small spacecraft near the inner Langrange point (L1)". In: *Proceedings of the National Academy of Sciences of the United States of America* 103.46 (2006). ISSN: 00278424. DOI: 10.1073/pnas.0608163103.

[12] Takanobu Kosugi. "Role of sunshades in space as a climate control option". In: *Acta Astronautica* 67.1-2 (2010), pp. 241–253. ISSN: 00945765. DOI: 10.1016/j.actaastro.2010.02.009.

[13] Viorel Badescu, ed. *Macro-engineering: a challenge for the future*. eng. Water science and technology library 54. OCLC: 255031769. Dordrecht: Springer, 2006. ISBN: 978-1-4020-4604-9 978-1-4020-3739-9.

[14] James D. Biggs, Colin R. McInnes, and Thomas Waters. "Control of Solar Sail Periodic Orbits in the Elliptic Three-Body Problem". en. In: *Journal of Guidance, Control, and Dynamics* 32.1 (Jan. 2009), pp. 318–320. ISSN: 0731-5090, 1533-3884. DOI: 10.2514/1.38362. URL: https://arc.aiaa.org/doi/10.2514/1.38362 (visited on 05/18/2021).

[15] Jie He and Fei Zheng. "Structural feasibility and orbital stability of a proposed huge space shield for mitigating global warming". en. In: *Advances in Mechanical Engineering* 9.10 (Oct. 2017), p. 168781401771922. ISSN: 1687-8140, 1687-8140. DOI: 10.1177/1687814017719227. URL: http://journals.sagepub.com/doi/10.1177/1687814017719227 (visited on 04/01/2021).

[16] R. Bewick, J. P. Sanchez, and C. R. McInnes. "The feasibility of using an L 1 positioned dust cloud as a method of space-based geoengineering". In: *Advances in Space Research* 49.7 (2012). Publisher: Elsevier Ltd, pp. 1212–1228. ISSN: 18791948. DOI: `10.1016/j.asr.2012.01.010`.

[17] R. Bewick, J.P. Sanchez, and C.R. McInnes. "Gravitationally bound geoengineering dust shade at the inner Lagrange point". en. In: *Advances in Space Research* 50.10 (Nov. 2012), pp. 1405–1410. ISSN: 02731177. DOI: `10.1016/j.asr.2012.07.008`. URL: `https://linkinghub.elsevier.com/retrieve/pii/S0273117712004504` (visited on 04/01/2021).

[18] Joan-Pau Sánchez and Colin R. McInnes. "Optimal Sunshade Configurations for Space-Based Geoengineering near the Sun-Earth L1 Point". en. In: *PLOS ONE* 10.8 (Aug. 2015). Ed. by Franck Marchis, e0136648. ISSN: 1932-6203. DOI: `10.1371/journal.pone.0136648`. URL: `https://dx.plos.org/10.1371/journal.pone.0136648` (visited on 03/30/2021).

[19] Juan B. Moreno-Cruz, Katharine L. Ricke, and David W. Keith. "A simple model to account for regional inequalities in the effectiveness of solar radiation management". In: *Climatic Change* 110.3-4 (2012), pp. 649–668. ISSN: 01650009. DOI: `10.1007/s10584-011-0103-z`.

[20] Dietmar Dommenget and Janine Flöter. "Conceptual understanding of climate change with a globally resolved energy balance model". en. In: *Climate Dynamics* 37.11-12 (Dec. 2011), pp. 2143–2165. ISSN: 0930-7575, 1432-0894. DOI: `10.1007/s00382-011-1026-0`. URL: `http://link.springer.com/10.1007/s00382-011-1026-0` (visited on 03/28/2021).

[21] Zebedee R. J. Nicholls et al. "Reduced Complexity Model Intercomparison Project Phase 1: introduction and evaluation of global-mean temperature response". en. In: *Geoscientific Model Development* 13.11 (Oct. 2020), pp. 5175–5190. ISSN: 1991-9603. DOI: `10.5194/gmd-13-5175-2020`. URL: `https://gmd.copernicus.org/articles/13/5175/2020/` (visited on 06/07/2022).

[22] William H. Press, ed. *Numerical recipes in C++: the art of scientific computing*. 2nd ed. Cambridge, UK ; New York: Cambridge University Press, 2002. ISBN: 978-0-521-75033-2.

[23] Karel Wakker. *Fundamental of Astrodynamics (AE4874 Lecture Notes)*. Delft University of Technology, Jan. 2015. ISBN: 978-94-6186-419-2.

[24] Victor G. Szebehely. *Theory of orbits: the restricted problem of three bodies*. Academic Press, 1967.

[25] Colin Robert McInnes. *Solar sailing: technology, dynamics and mission applications*. eng. Springer-Praxis series in space science and technology. OCLC: 246336919. London: Springer [u.a.], 1999. ISBN: 978-1-85233-102-3.

[26] Colin R. McInnes et al. "Solar sail parking in restricted three-body systems". en. In: *Journal of Guidance, Control, and Dynamics* 17.2 (Mar. 1994), pp. 399–406. ISSN: 0731-5090, 1533-3884. DOI: `10.2514/3.21211`. URL: `https://arc.aiaa.org/doi/10.2514/3.21211` (visited on 04/06/2021).

[27] J. B. Tatum. *Physics topics*. University Course Lecture Notes. Aug. 2022. URL: `http://astrowww.phys.uvic.ca/~tatum/stellatm.html`.

[28] Dennis L. Hartmann. *Global physical climatology*. International geophysics v. 56. San Diego: Academic Press, 1994. ISBN: 978-0-12-328530-0.

[29] J. Hansen et al. "GLOBAL SURFACE TEMPERATURE CHANGE". en. In: *Reviews of Geophysics* 48.4 (Dec. 2010), RG4004. ISSN: 8755-1209. DOI: `10.1029/2010RG000345`. URL: `http://doi.wiley.com/10.1029/2010RG000345` (visited on 08/20/2022).

A
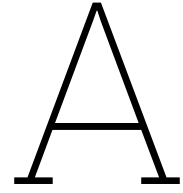
Verification & Validation

In this appendix, the simulation models set up for and used in this work are verified and validated. In particular, the following models were adopted:

- dynamical model;
- solar radiation model;
- shade model;
- solar limb darkening model;
- insolation model;
- climate model (GREB);

Furthermore, the following methods and tools should also be verified:

- reference frame transformations;
- optimal control problem.

The verification and validation (V&V) techniques for each building block listed above are explained in more detail in the following sections.

A.1. Dynamical model

In this section, the dynamical model is verified. The section is divided into the verification of the Circular Restricted Three-Body Problem (Sec. A.1.1) and the verification of the solar radiation pressure acceleration model (Sec. A.1.2).

A.1.1. Circular Restricted Three-Body Problem

The implementation of the Circular Restricted Three-Body Problem (CR3BP) was verified in two ways. Firstly, the locations of the collinear equilibrium points (L_1, L_2, and L_3) were compared to values reported in literature and the magnitude of the acceleration at the equilibrium points was evaluated. Secondly, the Zero-Velocity Curves of the CR3BP were plotted and compared against their equivalent published in literature. The two methods are described in more detail separately.

For both verification methods, it is necessary to introduce the synodic (or corotating) reference frame (SRF), S($\hat{\mathbf{x}}$, $\hat{\mathbf{y}}$, $\hat{\mathbf{z}}$). The SRF is centered at the barycenter of the Sun-Earth system,. One axis of the SRF, $\hat{\mathbf{x}}$, coincides with the vector connecting the primaries and is always oriented towards the smaller primary, m_2, while the $\hat{\mathbf{z}}$-axis coincides with the constant angular velocity vector, ω, describing the circular motion of m_1 and m_2 around the barycenter. The $\hat{\mathbf{y}}$-axis completes the right-handed reference frame.

Collinear Equilibrium Points

The collinear equilibrium points were found by means of a custom root-finding algorithm implemented in the code. Since for collinear Lagrange points there is only one non-zero coordinate, only the value

Type	$\mu\,[10^{-6}]$	L_1	L_2	L_3
Initial guess	–	0.95	1.01	−1.00
Code	3.040439	0.98998596496	1.01007521761	−1.00000126685
Wakker [23]	3.040000	0.98999	1.01008	−1.00000
Szebehely [24]	3.035900	0.9899909310	1.0100701938	1.0000012650
Δ Wakker	3.040000	$3.5 \cdot 10^{-6}$	$5.6 \cdot 10^{-6}$	$1.3 \cdot 10^{-6}$
Δ Szebehely	3.035900	$6.2 \cdot 10^{-6}$	$6.3 \cdot 10^{-6}$	$4.1 \cdot 10^{-6}$

Table A.1 — Non-dimensional x-coordinate of the collinear equilibrium points in the CR3BP found with a custom Newton-Raphson method. The initial guess, together with the characteristic mass parameter of the CR3BP, are reported. The results are compared with the values reported in literature by [23] and [24]. The last horizontal section of the table represents the difference between the values reported in literature and the ones found with the numerical implementation using the characteristic mass parameter of the CR3BP reported in literature.

Source	$\mu\,[10^{-6}]$	L_1	L_2	L_3
Code	3.040439	$-2.0 \cdot 10^{-16}$	$+1.0 \cdot 10^{-16}$	$< 1.0 \cdot 10^{-16}$
Wakker [23]	3.040000	$+2.0 \cdot 10^{-16}$	$-6.0 \cdot 10^{-16}$	$-2.0 \cdot 10^{-16}$
Szebehely [24]	3.035900	$-2.0 \cdot 10^{-16}$	$+5.0 \cdot 10^{-16}$	$+2.0 \cdot 10^{-16}$

Table A.2 — Non-dimensional acceleration computed at the collinear Lagrange points of the CR3BP for different values of the characteristic mass parameter μ.

of the x-coordinate is searched. This way, both the locations of the point and the correctness of the root-finding method can be verified simultaneously. The root-finding algorithm is a one-dimensional Newton-Raphson method, described for instance in Reference [22]. The settings of the Newton method included a maximum number of iterations equal to 50 and a tolerance equal to the reciprocal of the characteristic length of the CR3BP ($(1AU)^{-1} \approx 10^{-12}$). The Newton method is an iterative root-finding method, therefore it needs an initial guess. The initial guesses used for each collinear point are reported in Table A.1. It can be noticed that the difference between the values computed and the ones reported in literature is very close to the precision level of published values.

As a further verification method, the acceleration at the Lagrange points was computed with different values of the characteristic mass parameters μ. Obviously, such values should be very close zero, except for numerical errors. From Table A.2, it can be seen that this is indeed the case.

Zero-Velocity Curves

The Zero-Velocity Curves for the implementation of the CR3BP were reproduced and compared to the ones reported in Reference [23] and [24]. The Zero-Velocity Curves, also called *Hill's surfaces*, are directly related to the Jacobi's constant of the CR3BP. The Jacobi's constant C is an invariant quantity in the CR3BP and is defined as follows [24]:

$$C = -2U + V^2 \tag{A.1}$$

where U is the potential of the CR3BP at the position of a given body and V is its velocity. If the body's velocity is zero, this reduces to:

$$C = -2U \tag{A.2}$$

The Zero-Velocity Curves represent the regions of space that a body with a given value of the Jacobi's constant C is constrained to. In other words, a body with a given initial state (i.e., a fixed value of the Jacobi's constant) will be confined to a given Zero-Velocity Surface. To verify the implementation of the CR3BP, the Zero-Velocity Curves published in Reference [23] for a mass parameter equal to $\mu = 0.27$ and reported in Fig. A.2 were reproduced; the results are plotted in Fig. A.1. As it can be noticed, the two figures show the same topology. It is noted that the contour lines reported in Fig. A.2 differ from the ones shown in Fig. A.1. The same procedure was repeated with another source [24]; the results are reported in Fig. A.4 (original plots) and Fig. A.3 (reproduction) for a mass parameter equal to $\mu = 0.3$.
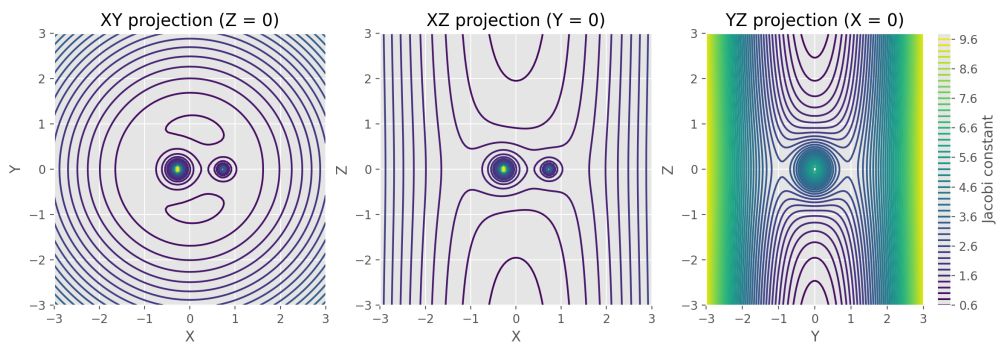
Figure A.1 — Zero-Velocity Curves computed with a characteristic mass parameter $\mu = 0.27$. This figure should be compared to Fig. A.2.
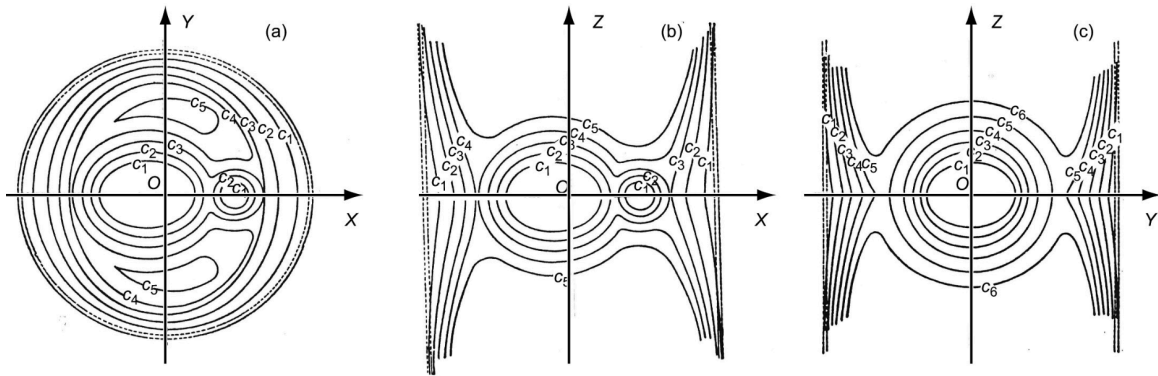
Figure A.2 — Zero-Velocity Curves published in [23], corresponding to a characteristic mass parameter $\mu = 0.27$. This figure should be compared to Fig. A.1.
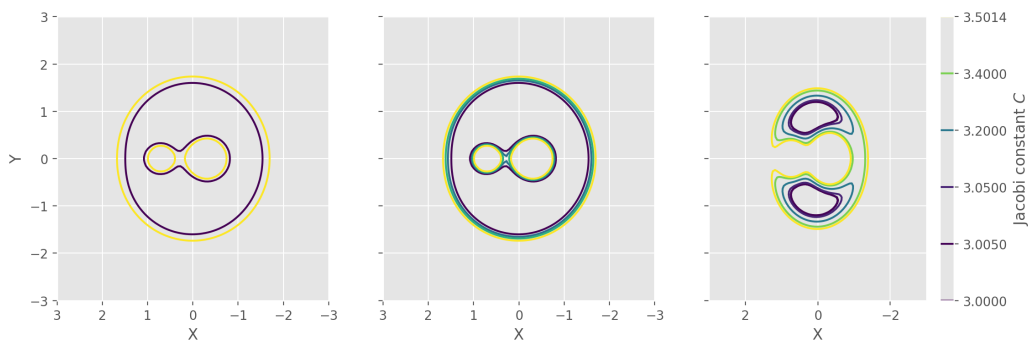
Figure A.3 — Zero-Velocity Curves computed with a characteristic mass parameter $\mu = 0.3$ for selected values of the Jacobi's constant C. This figure should be compared to Fig. A.4. It is noted that the orientation of the x-axis is flipped with respect to the conventional views.
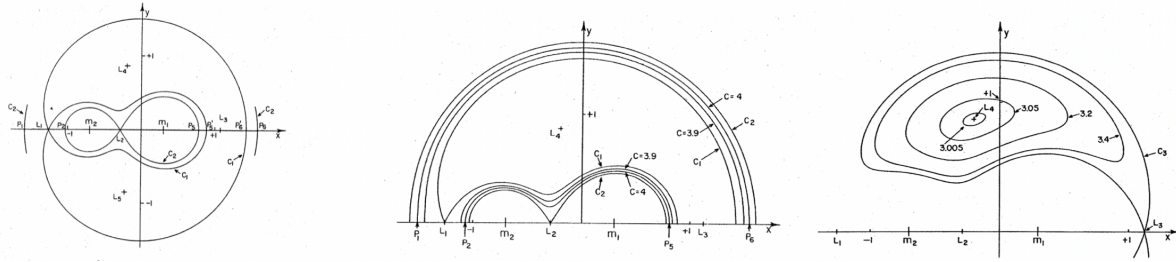
Figure A.4 — Zero-Velocity Curves published in [24], corresponding to a characteristic mass parameter $\mu = 0.3$ for selected values of the Jacobi's constant C. This figure should be compared to Fig. A.3. It is noted that the orientation of the x-axis is flipped with respect to the conventional views.
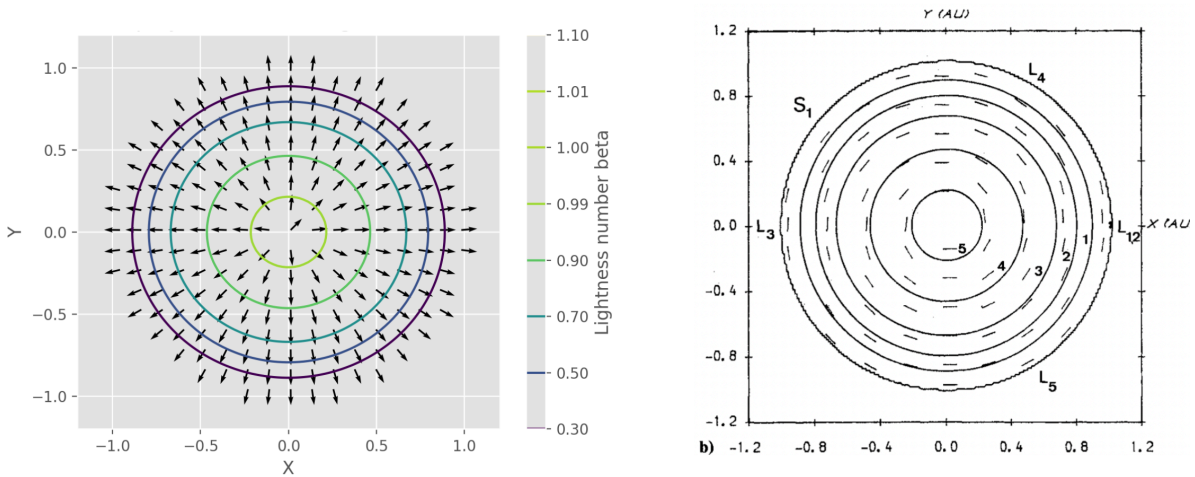
Figure A.5 — Surfaces in the xy-plane representing the lightness number β (contour lines) and sunshade orientation required to achieve equilibrium for a sunshade in the Sun-Earth CR3BP . The sunshade orientation is represented by plotting the vector normal to the sunshade **n** for the left panel (custom implementation) and the profile of the sunshade for the right panel (figure taken from Reference [26]).

A.1.2. Solar radiation pressure model

The solar radiation pressure model, together with the associated equations of motion, was implemented, following the model described in Reference [25]. The correctness of the numerical code reproducing the solar radiation pressure (SRP) acceleration for an ideal sail model was verified by reproducing the distribution of Artificial Equilibrium Points published in Reference [26].

The required lightness number and sunshade orientation to achieve equilibrium are shown for the xy-plane in Fig. A.5 (regular view) and in Fig. A.6 (vicinity of the L_1 point). It can be seen from Fig. A.5 that the lightness number required to achieve equilibrium increases with decreasing distance from the barycenter of the system. In addition, the SRP acceleration is always directed radially with respect to the barycenter, pointing away from the Sun. In Fig. A.6, it is possible to notice that no equilibrium solutions are found in certain areas of the xy-plane, specifically between the L_1 point and the Earth along the Sun-Earth line. This is due to the fact that the solar radiation pressure acceleration cannot point towards the Sun. Very similar features can be observed for the xz-plane in Fig. A.7 (regular view) and in Fig. A.8.

It can be seen how the plots taken from literature (right panels) and the figures reproduced with the custom implementation of the dynamical model (left panels) compare closely, which verifies the SRP computer model implemented for this work.

A.2. Radiation and shade model

The radiation model adopted for the Sun, together with the shade model, was preliminary verified by reproducing the results published in Reference [10]. These models will be verified further in Sec. A.5
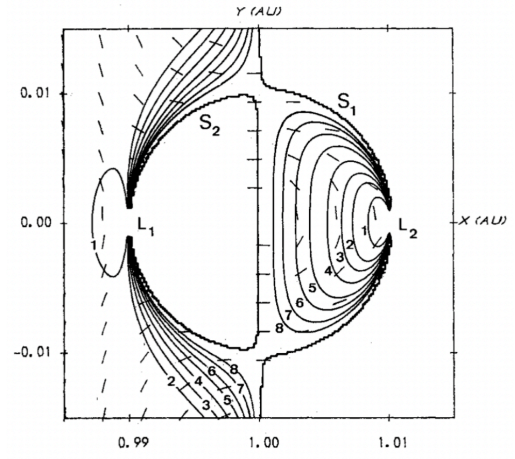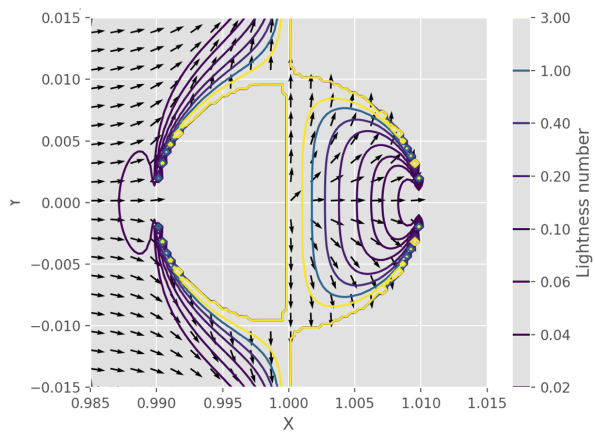
Figure A.6 — As in Fig. A.5, but in the vicinity of the secondary body.
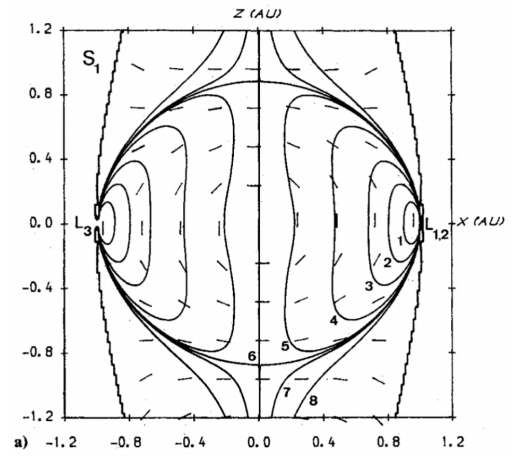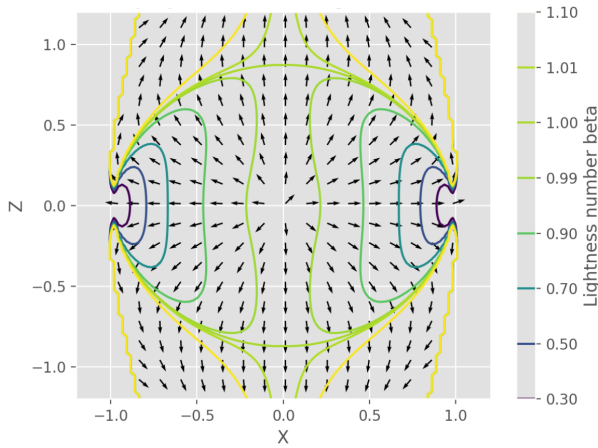
Figure A.7 — As in Fig. A.5, but for the xz-plane.
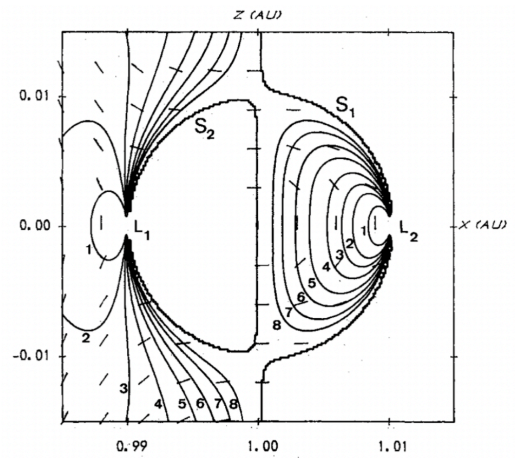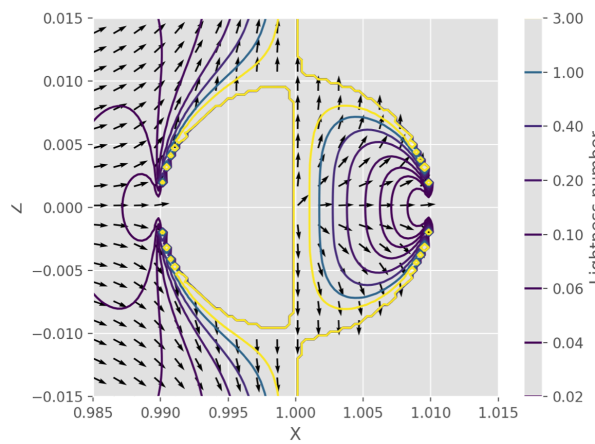
Figure A.8 — As in Fig. A.5, but for the xz-plane and in the vicinity of the secondary body.
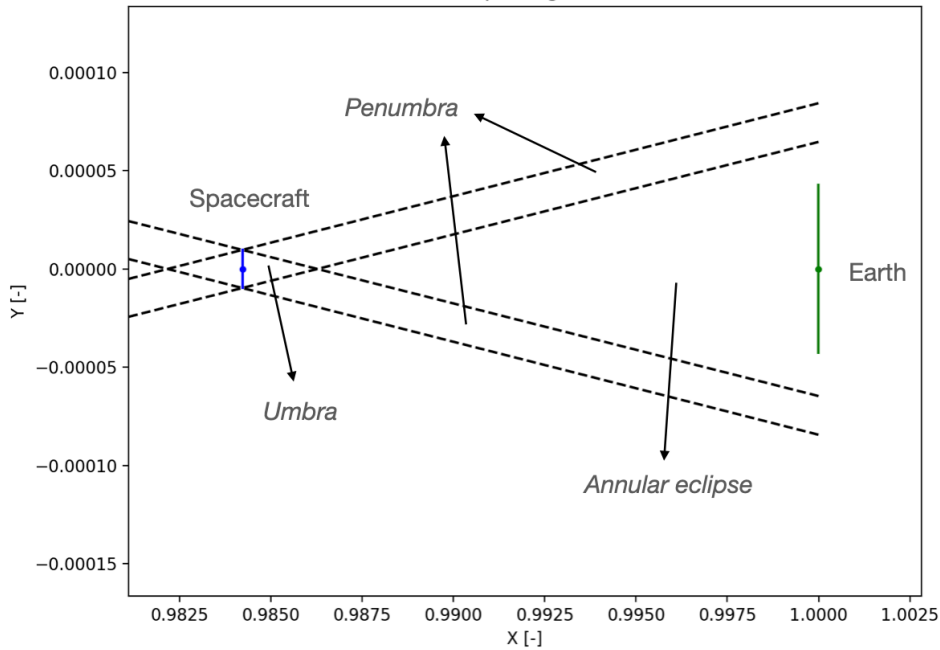
Figure A.9 — Main shade regions cast by a sunshade with the same size and location as in [10]. The figure shows the xy-plane of the Sun-Earth CR3BP in the vicinity of the Earth. The blue and green segments represent the extension of the sunshade's and the Earth's disk respectively.

and Sec. A.6. However, for this preliminary verification, no reference frame transformation is needed, as the radiation and shade models rely solely on the implementation of the CR3BP, verified in Sec. A.1.1.

In Reference [10], the optimal location and size of the sunshade to minimize its mass were found. The main constraint of the optimization concerned the reduction in solar radiation that the sunshade should achieve, fixed at -1.7%. To verify the radiation and shade models, the opposite approach was used: the location and size of the sunshade reported in Reference [10] were assumed. From those settings, the reduction in solar radiation was computed using the radiation and shade models, resulting in a decrease of 1.744%. This is deemed sufficiently close to the reduction assumed in Reference [10].

A further, qualitative verification method consisted of visualizing the main shading regions cast by the sunshade. These are reported in Fig. A.9. For a static sunshade, the Earth should be in the annular eclipse region, as it is the case in Fig. A.9.

A.3. Reference frame transformations

In this section, the transformations between reference frames (RFs) are verified. Two main reference frames were used in this work:

- the synodic (or *corotating*) reference frame of the CR3BP, based on cartesian coordinates;
- the Earth-centered, Earth-fixed spherical reference frame, based on spherical coordinates (latitude and longitude).

In addition, a change of coordinates (but not of reference frame) was also needed to transform cartesian coordinates into spherical coordinates. All these models were verified by visualizing the shade cast on the Earth's surface by the sunshade at different times during the year. In particular, a static sunshade with the same size and location as in Reference [10] was used for these tests. The point with the maximum solar radiation reduction on the Earth's surface was checked visually for three different times of the year: the spring equinox, the summer solstice, and the fall equinox. At these times, the point with the maximum solar radiation reduction should be located respectively on the Tropic of Cancer, on the equator, and on the Tropic of Capricorn. This is also what can be seen in Fig. A.10. Since no Earth's rotation was used in this work, the longitude of the point with the maximum solar radiation reduction is not relevant.
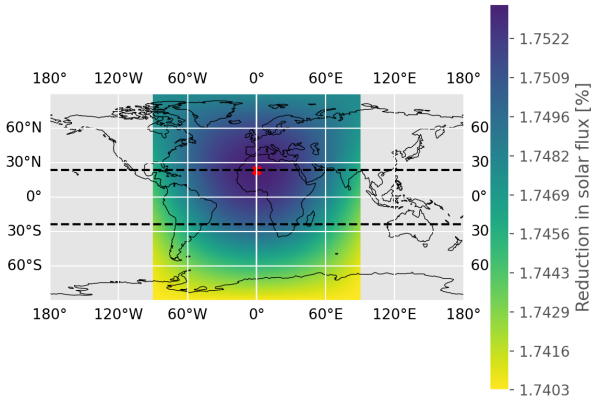
(a) At the Summer solstice.
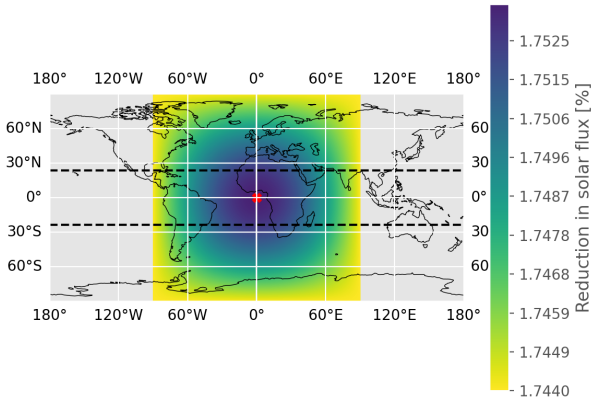
(b) At the fall/spring equinox.
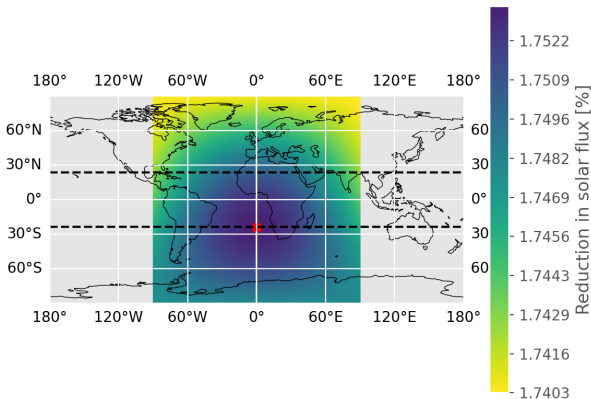
(c) At the winter solstice.

Figure A.10 — Solar radiation reduction cast at different times of the year by a sunshade located and sized as in [10]. The red cross denotes the point of maximum shade, while the dashed lines indicate the Tropics.
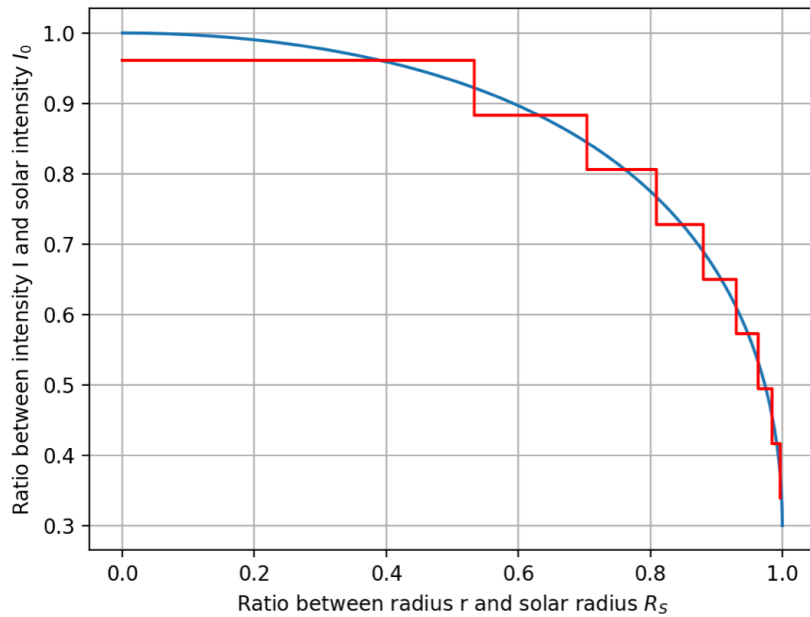
Figure A.11 — Continuous (blue) and discrete (red) solar limb darkening models.
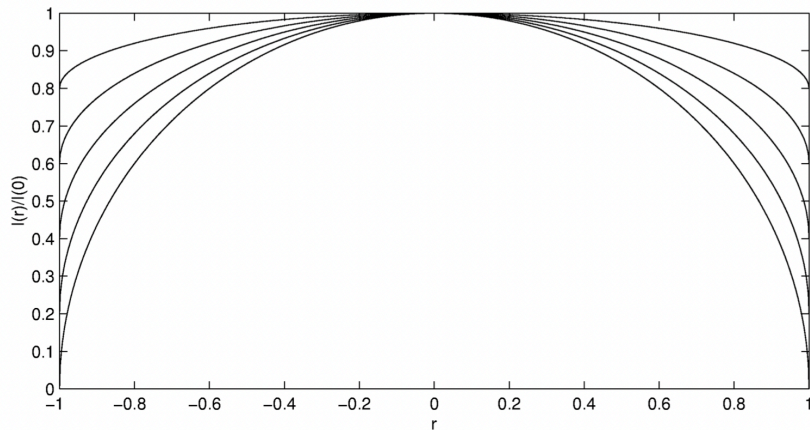
Figure A.12 — Continuous solar limb darkening model for various stellar types, taken from [27].

A.4. Solar Limb Darkening

The solar limb darkening model was verified in two ways. Firstly, the discretized model of limb darkening used in this work was compared to the continuous model and verified against results published in literature. Secondly, the irradiance resulting from the solar limb darkening model was computed to be checked against the value of the solar constant.

A.4.1. Continuous vs. discrete solar limb darkening model

In Fig. A.11, a comparison between the continuous and the discrete solar limb darkening models is reported. As it can be seen, the continuous case resembles the results published in literature (see Fig. A.12). In addition, it can be noticed that the discrete model approximates the behavior of the continuous one, so that the integrated intensity over the ten discrete solar disks of the discrete model is equal to the integrated intensity over the actual solar disk.

A.4.2. Computation of total irradiance

The total irradiance was computed from the limb darkening model. The same process was repeated for a solar model without limb darkening. If the solar intensity is integrated over the full radius of the
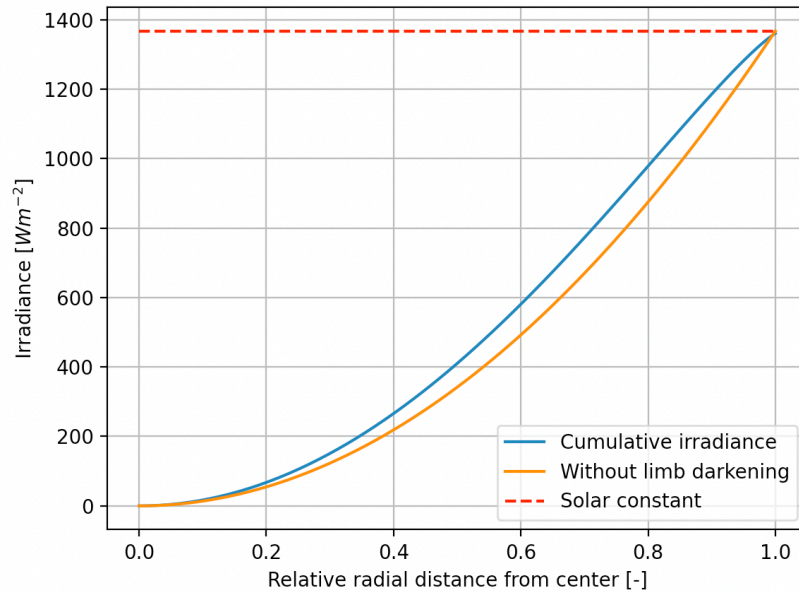
Figure A.13 — Integration of the intensity to compute the total irradiance for a solar model with limb darkening (blue) and without limb darkening (orange). The dashed red line shows the value of the solar constant.

Sun, the value of the Solar constant should be obtained. This is indeed shown in Fig. A.13.

A qualitative verification of the implementation of the solar limb darkening model is also visible in Fig. A.14. This figure should be compared to Fig. A.10a, where the same shading conditions were reproduced without the effect of solar limb darkening. By comparing the two figures, two expected features can be detected. Firstly, the average reduction in solar radiation is larger when including limb darkening. This is because the sunshade is statically placed on the ecliptic plane, therefore it shades the region of the Sun closer to its center. This region is indeed the brightest, therefore a greater level of solar radiation is blocked from reaching the Earth. Secondly, the spatial gradient visible in the plotted shade is not constant, as it was in Fig. A.10a. This is again due to the solar limb darkening model implemented.

A.5. Insolation model

The verification of the insolation model was carried out in two ways. Firstly, the natural insolation distribution (over latitude and over time) was compared to published results. In addition, the same results were reproduced with and without limb darkening to provide a further proof of the correctness of the limb darkening model. Furthermore, the distribution in insolation difference due to a static shade was reproduced and compared to results published in literature. The two methods are described in two separate subsections below.

A.5.1. Natural insolation distribution

The insolation model implemented for this work is used to compute the latitudinal and temporal distribution of the natural insolation received by the Earth. The results are compared to published results in Fig. A.15 (comparison with [28] with a solar constant of $S_0 = 1360 \, W \, m^{-2}$) and Fig. A.16 (comparison with [18] with a solar constant of $S_0 = 1367 \, W \, m^{-2}$). As it can be seen, the plots show no difference with respect to published results. Furthermore, it is possible to notice that even a difference in the solar constant smaller than 1% can produce non-negligible changes in the resulting insolation distribution.

In addition, in Fig. A.17 the natural insolation distribution was computed with the addition of solar limb darkening. Limb darkening is only relevant when a shading body is present. Without a sunshade, the resulting insolation distribution should not show any difference. This is proven by the comparison shown in Fig. A.17. This method also verifies the solar limb darkening model.
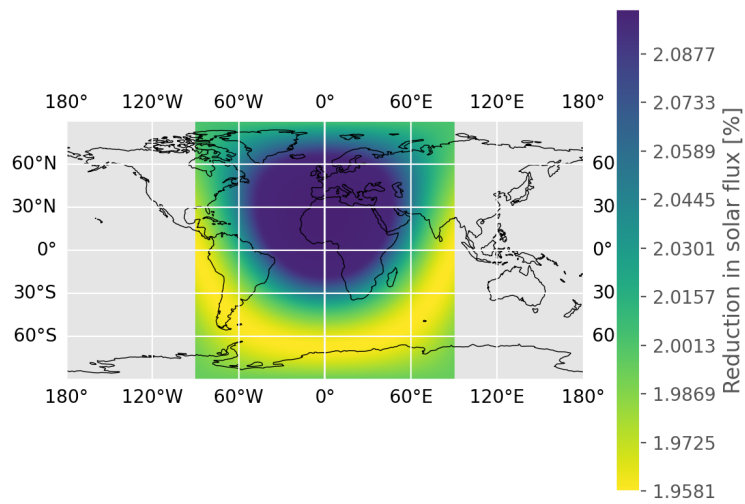
Figure A.14 — As in Fig. A.10a, but with a discrete solar limb darkening model implemented.
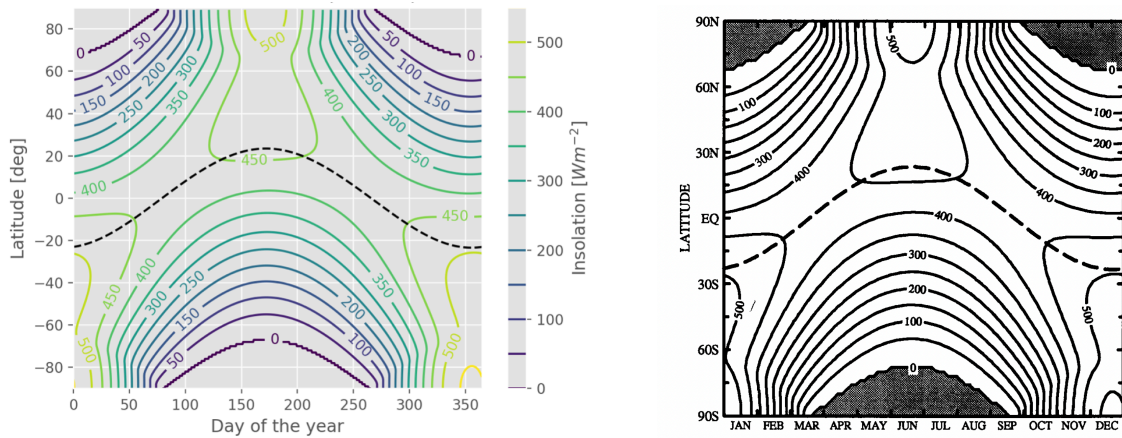
Figure A.15 — Temporal and latitudinal distribution of the natural insolation computed with a solar constant $S_0 = 1360\,W\,m^{-2}$. Right plot: custom model; left plot: figure taken from [28]. The dashed line indicates the latitude of the subsolar point at noon.
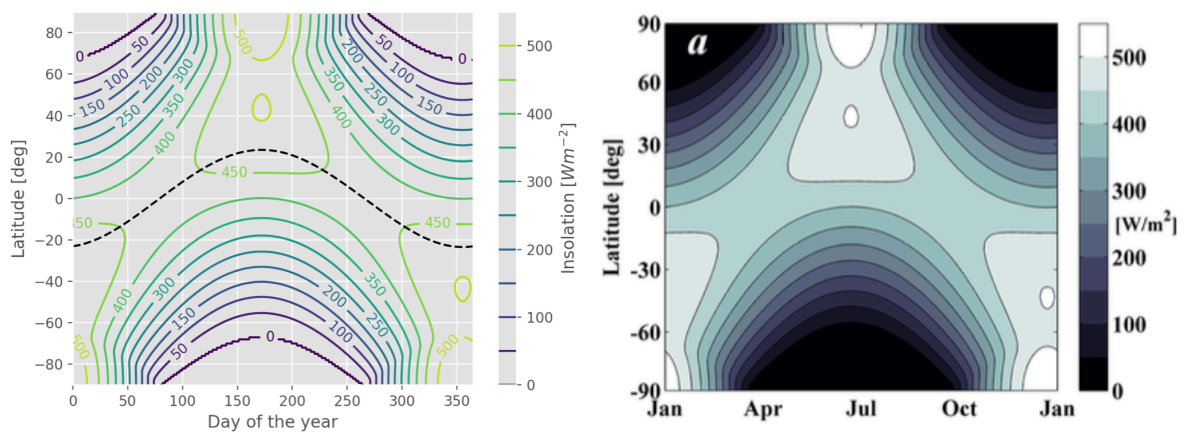
Figure A.16 — Temporal and latitudinal distribution of the natural insolation computed with a solar constant $S_0 = 1367\,W\,m^{-2}$. Right plot: custom model; left plot: figure taken from [18]. The dashed line indicates the latitude of the subsolar point at noon.
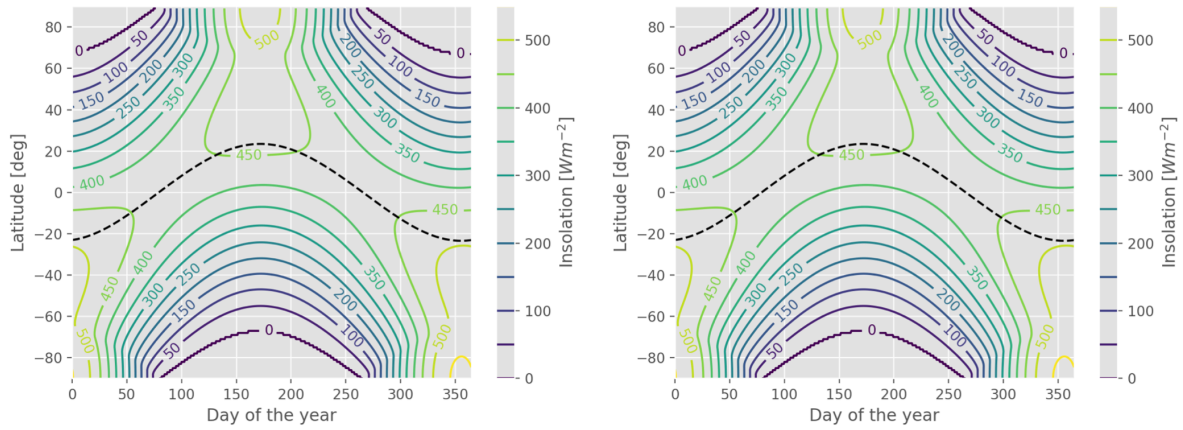
Figure A.17 — As in Fig. A.15, but without (left plot) and with (right plot) a limb darkening for the solar model.
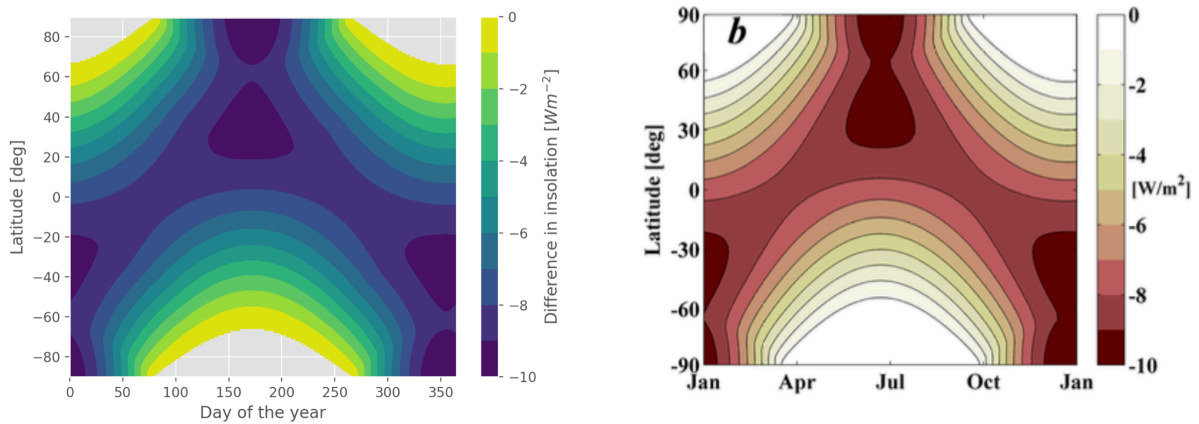
Figure A.18 — Temporal and latitudinal distribution of the difference in natural insolation caused by a static sunshade. The settings for the sunshade and solar insolation model are the same as in [18] Right plot: custom model; left plot: figure taken from [18].

A.5.2. Distribution of insolation difference

The insolation model was further verified by comparing the distribution of insolation difference caused by a static sunshade. The sunshade's size and location are as in Reference [18]. The comparison, where a similar limb darkening model and the same value of the solar constant are used, is shown in Fig. A.18. It can be seen that the two plots reproduce the same behavior, with slight differences in the areas of the plot where the maximum insolation difference occurs. It should be reminded that the scale of this plot is two orders of magnitude smaller than in Fig. A.16. In addition, the discrete contour lines do not reproduce any feature within a specific contour interval. Therefore, the maximum differences with respect to the results published in Reference [18] were checked manually and were found to be between $0.22\,W\,m^{-2}$ and $1.21\,W\,m^{-2}$ (the exact number is not known given the nature of the contour plot published in Reference [18]). Given some slight differences in the discretization of the solar limb darkening model, the slight mismatch in the distribution of the insolation difference is considered acceptable in the context of this work. Furthermore, Fig. A.16 verifies further some of the models discussed in the previous sections, including the solar radiation model, the shading model, and the solar limb darkening model. It also verifies the reference frame transformations that will be verified in Sec. A.3.
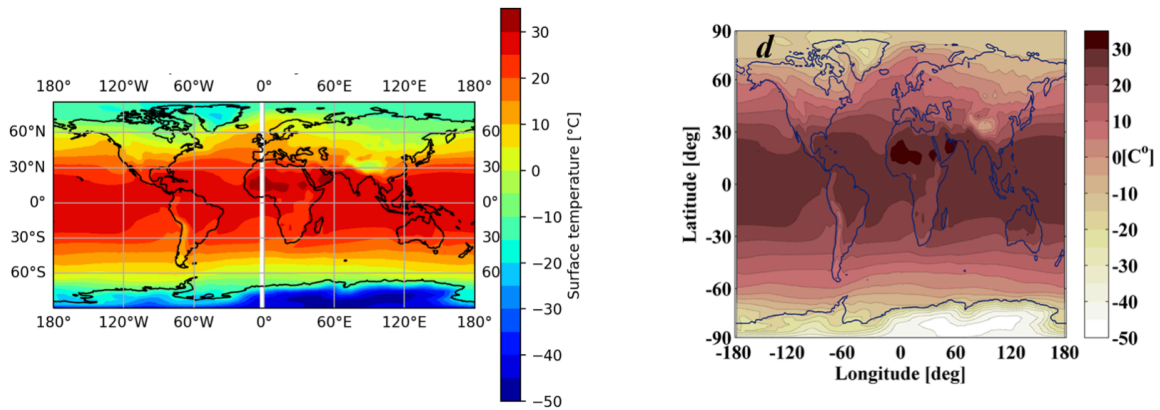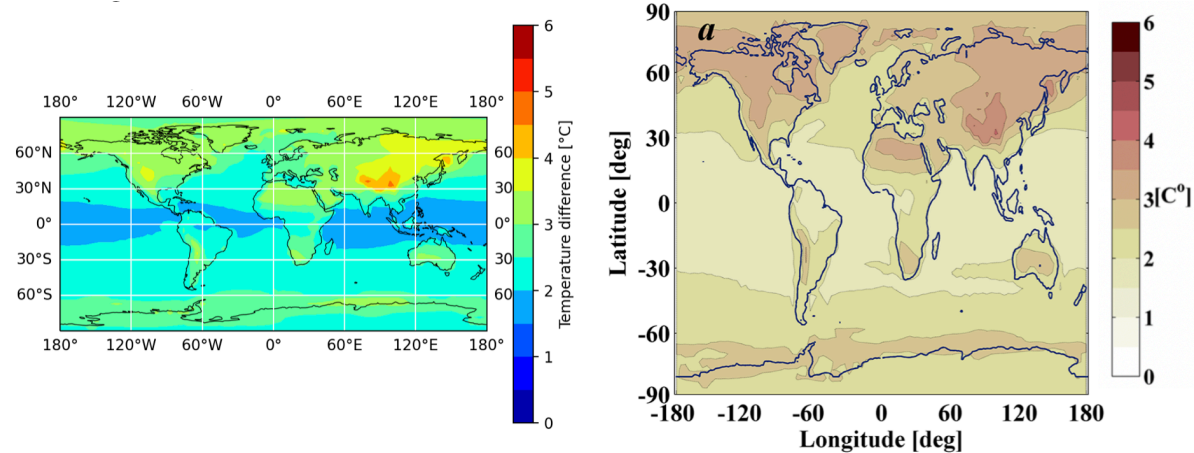
Figure A.19 — Annual mean of the surface temperature for the 50th year of a climate simulation with a CO_2 concentration of 680 ppm, obtained through the GREB model. Left panel: custom implementation of the GREB model; right panel: original implementation of the GREB model in Reference [20] and published in Reference [18].

A.6. Climate model

The Globally Resolved Energy Balance (GREB) climate model was rewritten in Python starting from the Fortran code provided with the original GREB paper[1] [20]. Therefore, the code had to be verified against the results of the original code. This constituted the longest and most important verification effort carried out in this work, given the complexity of GREB's code. All inputs required by the model were provided with GREB's code, therefore they did not have to be verified thoroughly. Nonetheless, the spatiotemporal distribution of the input variables was verified through plots to be compared with the original inputs published in [20].

The first verification (and validation) method entailed the computation of the Global Mean Surface Temperature (GMST) after a simulation of 50 years with a pre-industrial concentration of CO_2 equal to 340 ppm. This means that the model parameters should stay close to their initial values, including the GMST, as no change in climate forcing is introduced. The simulation yielded a GMST of $T_{1xCO2}^{global} = 13.92\,°C$, which is within the range of observed GMST for the 1951-1980 period [29].

Furthermore, another simulation with twice the amount of atmospheric CO_2 (680 ppm) was run. The spatiotemporal distribution of the annual mean of the surface temperature was reproduced and compared to the same result published in Reference [18]. The visual comparison, shown in Fig. A.19, confirms that the model works correctly.

The difference between the surface temperature shown in Fig. A.19 and the reference scenario with a CO_2 concentration of 340 ppm is presented in Fig. A.20, compared to the equivalent results published in Reference [18] using the original GREB model. In such figure, the scale of the contour level is reduced by an order of magnitude and some minor differences with respect to published results can be noticed. In particular, although the general pattern of the spatiotemporal distribution is very similar, the custom implementation of the GREB model shows a smaller temperature difference over North America and in other areas. Nevertheless, the differences are relatively small in magnitude ($< 0.5\,°C$), but especially they are confined to small areas of the planet. Therefore, such differences can be neglected for the purpose of this work, as they are likely caused by either the grid used by the model or the features of the contour plots.

Another similar comparison is shown in Fig. A.21. This figure compares the latitudinal and seasonal distribution of the temperature difference obtained by comparing the two CO_2 scenarios presented above. Fig. A.21 confirms the conclusions drawn above.

A.7. Optimal control problem

The feasibility of the trajectory obtained from the optimal control problem was verified by numerically integrating the trajectory using the same initial state adopted in the optimal control problem and the control profiles found by the optimal control solver. A fixed-step Runge-Kutta 4 integrator was used. The fixed integration step was selected to be 10% of the time step between the first and second collo-

---

[1]`https://users.monash.edu.au/~dietmard/content/GREB/code.html`

Figure A.20 — Annual mean of the surface temperature difference for the 50th year of two climate simulation, one with a CO_2 concentration of 680 ppm and one with half the amount (340 ppm, considered as a reference scenario). Left panel: custom implementation of the GREB model; right panel: original implementation of the GREB model in Reference [20] and published in Reference [18].
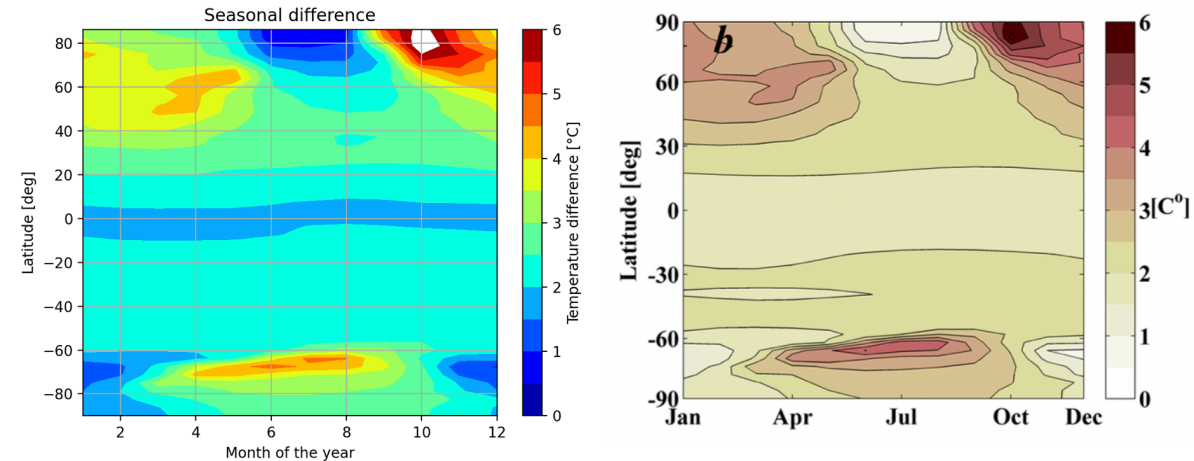
Figure A.21 — As in Fig. A.20, but the latitudinal and seasonal distribution is shown.

cation point of the optimal control problem. The comparison between the optimal and the numerically integrated trajectories are reported in Fig. A.22. As it can be seen, the numerically integrated solution is quite close to the output of the optimal control problem. This is true except for the final value of the x-component of the position vector. This is likely caused by the discontinuity in the first derivative of the cone angle profile, which presents a cusp around the midpoint of the transfer.

Finally, the time-optimality of the solution was checked by integrating the same trajectories with the same initial conditions, yet with a slightly perturbed control profile. Although the final state was not exactly the one prescribed, the transfer trajectory took a longer time than the optimal solution.
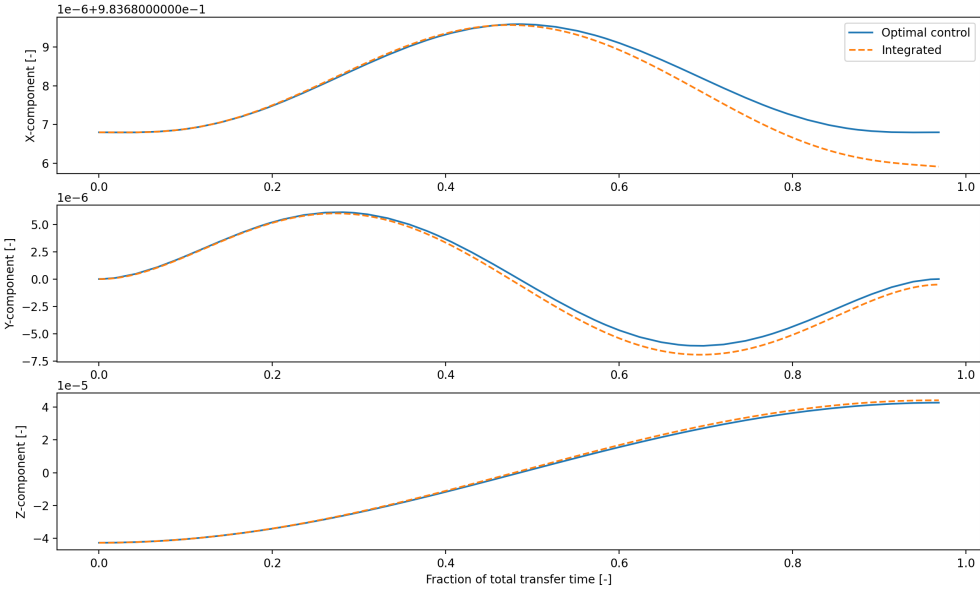
(a) Position components.
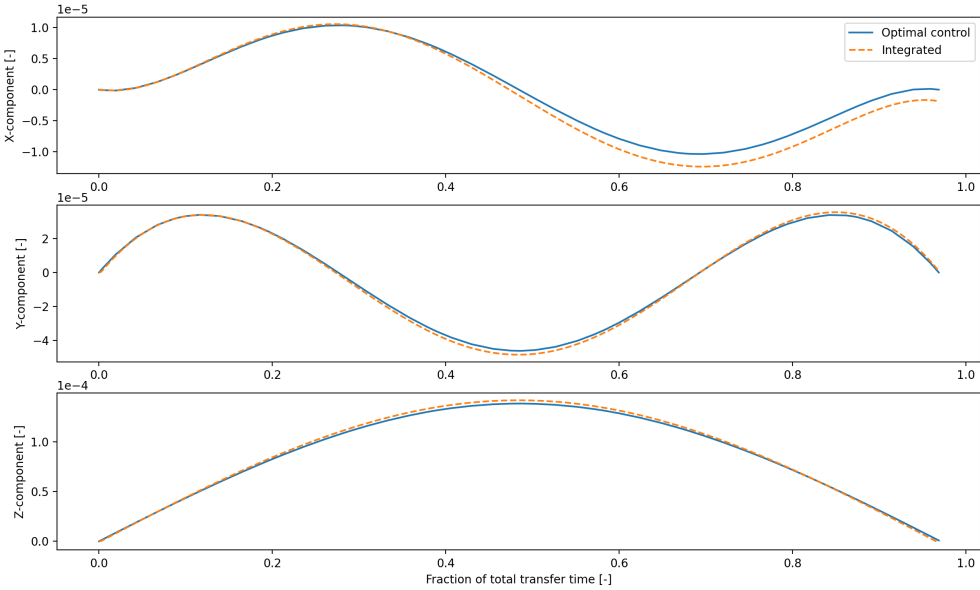
(b) Velocity components.

Figure A.22 — Comparison between the time-optimal trajectory (blue) and the numerically integrated trajectory (dashed orange).

Acknowledgments

Ringraziamenti

Questo lavoro non sarebbe stato possibile senza il sostegno di molte persone.

Innanzitutto, grazie alla mia famiglia. Mamma, sei stata la sostenitrice silenziosa ma costante che mi ha permesso di studiare qui a Delft, accogliendo (quasi) sempre le tante iniziative che ho intrapreso in questi anni. In questo percorso ho potuto godere della libertà e dell'indipendenza, due dei valori a cui tengo di più, senza mai sentirmi solo. Credo che trovare un tale equilibrio non sia facile per un genitore e per questo ti sono profondamente grato. Di mio fratello Luca apprezzo la saggezza spontanea e l'approccio "delicato" alla vita, notevole per la sua giovane età. Da fratello minore sei diventato un mio pari. Se posso dirlo, sono orgoglioso di quello che stai diventando e non vedo l'ora di continuare a crescere insieme nella vita, come abbiamo fatto da bambini. Grazie a mio padre, che mi ha mostrato cosa significa "non mollare mai", e a Gigi, che è sempre stato una presenza stabile a casa e in famiglia. Un riconoscimento va a mio zio Andrea, a mia zia Chiara, a Camilla e Benedetta, che si ricordano sempre di scrivermi delle belle parole a ogni tappa di questo percorso. Grazie ai miei nonni: vi penso spesso con affetto. Devo alla vostra guida e al vostro amore gran parte di ciò che sono oggi. Mi mancate!

Poi, i miei amici. Ho la fortuna di averli sparsi per il mondo, quindi purtroppo non posso condividere questi momenti insieme a tutti loro. Non sono molto bravo a tenere i contatti quando sono lontano, quindi grazie per essere così pazienti con me. Grazie a Carlo, per essere sempre presente, ma anche a Paul, Ale, Cinciu, Luca, Mazzu, Giammo, Filo, Edo, Marche, Tita, Giuli, Fra, Place, Fede e così via. Tornare a casa non sarebbe lo stesso senza di voi. Grazie a Steve per il tempo passato insieme a Parigi.

Sof, anche se non abbiamo condiviso molto di questo percorso, è come se fossi sempre stata al mio fianco. Tutto il resto, lo sai.

Un riconoscimento speciale va ai miei colleghi di Revolv: Marco, Olek, Michal e tutti gli altri. Ci vuole coraggio per fondare una società a 25 anni, ma non vorrei farlo con nessun altro. Finora è stato memorabile, comprese le telefonate di quattro ore, le giornate interminabili piene di riunioni e le "emotional rollercoaster" quotidiane. Mi piace come non perdiamo mai la speranza o come troviamo sempre un modo per superare gli ostacoli, anche se non è tutto nuovo e non l'abbiamo mai fatto prima. Sono curioso di vedere dove ci porterà tutto questo.

Grazie a Jeannette, la mia relatrice, per essere stata sempre paziente e corretta: la qualità del tuo lavoro, insieme ai tuoi consigli, mi ha insegnato molto più di quanto mi sarei mai aspettato. Grazie a Pau per aver trovato sempre il tempo di dare il suo feedback e per essere sempre stato molto concreto. Grazie a Dominic, per avermi accolto nel team di TUDAT, e a Florent, per avermi insegnato un po' di meccanica orbitale e un po' di francese, a volte contemporaneamente. Grazie a Tim, il mio primo mentore, per aver reso proficuo un tirocinio a distanza. Grazie anche a Metzger, per tutte le sessioni di "brainstorming".

Infine, ma non per questo meno importante, grazie a questo bellissimo posto chiamato Delft, in cui sono racchiuse così tante esperienze di vita. Sono felice di poter dire che il Covid non è riuscito a rovinare i miei anni da studente a Delft. Grazie a tutte le persone incontrate tramite l'università: Askar, Irina, Joe, Benni, Gaia, Frank, Willem, Salvo, Tadek, Pietro, Dominik, Berend, Jonas e Jaime, solo per citarne alcuni. Grazie a Olek per essere sempre onesto, disponibile, solidale, laborioso ed energico: sei una delle persone della nostra generazione che ammiro di più. Daniele, la tua conoscenza enciclopedica è superata solo dalla tua modestia e dal tuo senso dell'umorismo: in qualche modo, mi lasci sempre senza parole, quindi grazie per questo. A Mathieu, Emily, Thomas e Florian, grazie per essere stati dei coinquilini fantastici. Grazie a Nerea per avermi mostrato perché i modelli di dischi circumplanetari sono importanti (e per molte altre cose). Grazie anche alle persone di Punch e Shot: mi sono sentito il benvenuto in tutti questi ambienti. Imparare il modo olandese di vivere e di vedere le cose è stato per me una fonte insostituibile di crescita personale e intellettuale.